


University of Alberta

**Total Ionizing Dose Effects on Xilinx
Field-Programmable Gate Arrays**

by

Daniel Montgomery MacQueen 

A thesis

submitted to the Faculty of Graduate Studies and Research

in partial fulfillment of the requirements for the degree

of

Master of Science

Department of Physics

Edmonton, Alberta

Fall 2000



National Library
of Canada

Acquisitions and
Bibliographic Services

395 Wellington Street
Ottawa ON K1A 0N4
Canada

Bibliothèque nationale
du Canada

Acquisitions et
services bibliographiques

395, rue Wellington
Ottawa ON K1A 0N4
Canada

Your file Votre référence

Our file Notre référence

The author has granted a non-exclusive licence allowing the National Library of Canada to reproduce, loan, distribute or sell copies of this thesis in microform, paper or electronic formats.

The author retains ownership of the copyright in this thesis. Neither the thesis nor substantial extracts from it may be printed or otherwise reproduced without the author's permission.

L'auteur a accordé une licence non exclusive permettant à la Bibliothèque nationale du Canada de reproduire, prêter, distribuer ou vendre des copies de cette thèse sous la forme de microfiche/film, de reproduction sur papier ou sur format électronique.

L'auteur conserve la propriété du droit d'auteur qui protège cette thèse. Ni la thèse ni des extraits substantiels de celle-ci ne doivent être imprimés ou autrement reproduits sans son autorisation.

0-612-59840-3

Canada

Abstract

This thesis presents the results of radiation tests of Xilinx XC4036X series Field Programmable Gate Arrays (FPGAs). These radiation tests investigated the suitability of the XC4036X FPGAs as controllers for the ATLAS liquid argon calorimeter front-end boards. The FPGAs were irradiated with gamma rays from a cobalt-60 source at a average dose rate of 0.13 rad(Si)/s. An average total dose of 39 krad(Si) was absorbed by the XC4036XL FPGAs before the power supply current increased. The XC4036XLA FPGAs absorbed an average of 16 krad(Si) before the power supply current increased. Neither type of FPGA is expected to meet the ATLAS requirement of surviving at least 80 krad(Si) over 10 years without failure.

Acknowledgements

I would like to thank Dr. Douglas M. Gingrich of the University of Alberta for his support as a supervisor, his demonstration of Fricke dosimetry, and his work on prior publications of the results presented in this thesis. The other members of the examining committee have my gratitude for their many useful comments.

I would also like to thank Dr. Peter Green for writing the program used in monitoring the FPGAs, Norm Buchanan for advice and assistance with several of the tests, Shane Mullin and Lars Holm for invaluable technical support, the University of Alberta Department of Chemistry for the use of their gamma ray source and spectrophotometers, and Vaidy Bala of Saskatchewan Labour for measurements of the thermoluminescent detectors.

Finally, I would like to thank all of my friends, family, and colleagues for their support.

Contents

| | | |
|----------|---|-----------|
| 1 | Introduction | 1 |
| 1.1 | The ATLAS Detector | 2 |
| 1.2 | Programmable Logic and Field-Programmable Gate Arrays | 6 |
| 1.3 | Front End Electronics | 11 |
| 1.3.1 | Analog Memory in Front End Electronics | 11 |
| 1.3.2 | FPGA Implementation of the SCA Controller | 13 |
| 1.4 | Radiation Environment in ATLAS | 18 |
| 2 | Ionizing Radiation | 20 |
| 2.1 | Types of Radiation | 21 |
| 2.2 | Cobalt-60 Sources | 24 |
| 2.3 | Interaction of Gamma Rays With Matter | 27 |
| 2.4 | Dosimetry | 33 |
| 2.4.1 | Fricke Dosimetry | 33 |
| 2.4.2 | Thermoluminescent Detector Dosimetry | 36 |
| 3 | Radiation Effects | 38 |
| 3.1 | Effects of Radiation on Electronics | 39 |
| 3.1.1 | Effects of Ionization | 39 |

| | | |
|----------|---|-----------|
| 3.1.2 | MOS and CMOS Structures | 40 |
| 3.1.3 | Effects of Radiation on MOS and CMOS Structures | 44 |
| 3.2 | Annealing Effects | 48 |
| 3.3 | Recent Radiation Tests of FPGAs | 50 |
| 3.3.1 | Total Ionizing Dose Tests | 50 |
| 3.3.2 | Single Event Tests of SRAM-based Field Programmable Gate Ar- rays | 52 |
| 4 | Radiation Testing | 55 |
| 4.1 | Initial Tests of Dosimetry, Shielding, and Geometry | 56 |
| 4.1.1 | Testing of Fricke Dosimetry | 56 |
| 4.1.2 | Dosimetry Test With Lead Wall | 61 |
| 4.1.3 | Dosimetry Test With Full Enclosure | 70 |
| 4.1.4 | Comparison of Dose Response in Fricke Dosimeters and Thermo- luminescent Detectors | 78 |
| 4.2 | Setup for Radiation Tests of FPGAs | 90 |
| 4.3 | Monitoring Program | 92 |
| 4.4 | Interpolation of Dose Rates to the FPGA Die | 94 |
| 4.5 | Test Procedure | 96 |
| 5 | Results | 98 |

| | | |
|----------|--|------------|
| 5.1 | Test Results for XC4036XL Devices | 99 |
| 5.1.1 | First Irradiation Period | 101 |
| 5.1.2 | Annealing Period | 102 |
| 5.1.3 | Second Irradiation Period | 104 |
| 5.2 | Test Results for XC4036XLA Devices | 107 |
| 5.2.1 | First Irradiation Period | 108 |
| 5.2.2 | Annealing Period | 110 |
| 5.2.3 | Second Irradiation Period | 111 |
| 6 | Conclusions | 115 |
| 6.1 | Further Work | 116 |
| 6.2 | General Conclusions | 118 |

List of Tables

| | | |
|-----|---|-----|
| 1.1 | Approximate radiation levels in the crack region of ATLAS. | 18 |
| 2.1 | Parameters used to calculate dose rate using Fricke dosimetry. | 35 |
| 4.1 | Dose rates measured for each dosimeter in lead wall test. | 68 |
| 4.2 | Attenuation factors for central dosimeters in lead wall test. | 70 |
| 4.3 | Dose rates measured for each dosimeter in full enclosure test. | 77 |
| 4.4 | Attenuation factors for dosimeters inside aluminum box. | 78 |
| 4.5 | Dose measured for each TLD compared to dose estimated using nearest Fricke dosimeter. | 84 |
| 4.6 | Dose rates measured for each Fricke dosimeter irradiated for combined TLD and Fricke test. | 86 |
| 4.7 | Attenuation factors used to find dose rate in FPGA die. | 95 |
| 5.1 | Date codes for XL FPGAs. | 99 |
| 5.2 | Dose rates measured for each XL FPGA tested. | 100 |
| 5.3 | Results from irradiation of XL FPGAs. | 101 |
| 5.4 | Dose rates measured for each XLA FPGA tested. | 107 |
| 5.5 | Results from irradiation of XLA FPGAs. | 108 |

List of Figures

| | | |
|-----|--|----|
| 1.1 | The ATLAS detector. | 4 |
| 1.2 | Liquid Argon Calorimetry in ATLAS. | 5 |
| 1.3 | Conceptual structure of FPGAs, modeled after reference [3]. | 7 |
| 1.4 | Diagram of read-out electronics, from reference [2]. | 12 |
| 1.5 | Communications with the SCA controller. | 13 |
| 1.6 | Block diagram of the SCA controller. | 15 |
| 2.1 | Dominant decay scheme of cobalt-60 | 24 |
| 2.2 | Cave-type cobalt-60 source at the University of Alberta, not to scale. . . | 26 |
| 2.3 | Backscattering of electrons, and use of low-Z shielding | 32 |
| 3.1 | Cross-sectional view of an n-channel MOSFET | 41 |
| 3.2 | Cross-sectional schematic of an n-well CMOS inverter, modeled after reference [20] | 43 |
| 3.3 | Radiation-induced shifts in enhancement MOSFET I_D - V_G curves, mod- eled after reference [19] | 45 |
| 4.1 | Setup of the first Fricke dosimetry test, not to scale. | 57 |
| 4.2 | First Fricke dosimetry test: Reduced dose versus time measured in the left dosimeter. | 58 |

| | | |
|------|---|----|
| 4.3 | First Fricke dosimetry test: Dose versus time measured in the centre dosimeter. | 59 |
| 4.4 | First Fricke dosimetry test: Dose versus time measured in the right dosimeter. | 60 |
| 4.5 | Setup of lead wall test, not to scale. | 62 |
| 4.6 | Lead wall test: Dose versus time measured in the far central dosimeter. . | 63 |
| 4.7 | Lead wall test: Dose versus time measured in the mid-central dosimeter. | 64 |
| 4.8 | Lead wall test: Dose versus time measured in the near central dosimeter. | 64 |
| 4.9 | Lead wall test: Dose versus time measured in the left backscatter dosimeter. | 65 |
| 4.10 | Lead wall test: Dose versus time measured in the right backscatter dosimeter. | 65 |
| 4.11 | Lead wall test: Dose versus time measured in the background dosimeter in the line of radiation. | 66 |
| 4.12 | Lead wall test: Dose versus time measured in the background dosimeter out of the line of radiation. | 66 |
| 4.13 | Lead wall test: Dose versus time measured in the background dosimeter outside the cave. | 67 |
| 4.14 | Setup of full enclosure test, not to scale. | 72 |
| 4.15 | Full enclosure test: Dose versus time measured in the front central dosimeter. | 73 |
| 4.16 | Full enclosure test: Dose versus time measured in the rear central dosimeter. | 74 |

| | |
|---|----|
| 4.17 Full enclosure test: Dose versus time measured in the left backscatter dosimeter. | 74 |
| 4.18 Full enclosure test: Dose versus time measured in the right backscatter dosimeter. | 75 |
| 4.19 Full enclosure test: Dose versus time measured in the background dosimeter in line of radiation. | 75 |
| 4.20 Full enclosure test: Dose versus time measured in the background dosimeter out of line of radiation. | 76 |
| 4.21 Full enclosure test: Dose versus time measured in the background dosimeter outside the cave. | 76 |
| 4.22 Setup for combined TLD and Fricke dosimetry test, not to scale. | 80 |
| 4.23 Combined TLD and Fricke test: Dose versus time measured in the far left dosimeter. | 81 |
| 4.24 Combined TLD and Fricke test: Dose versus time measured in the near left dosimeter. | 81 |
| 4.25 Combined TLD and Fricke test: Dose versus time measured in the central dosimeter. | 82 |
| 4.26 Combined TLD and Fricke test: Dose versus time measured in the near right dosimeter. | 82 |
| 4.27 Combined TLD and Fricke test: Dose versus time measured in the far right dosimeter. | 83 |

| | |
|---|-----|
| 4.28 Combined TLD and Fricke test: Dose versus time measured in all irradiated Fricke dosimeters. | 83 |
| 4.29 Combined TLD and Fricke test: Comparison of TLD results to time spent under irradiation. | 85 |
| 4.30 Combined TLD and Fricke test: Plot of residuals between TLD and Fricke results. | 87 |
| 4.31 Combined TLD and Fricke test: Distribution of residuals, compared to a Gaussian fit. | 88 |
| 4.32 Combined TLD and Fricke test: Distribution of individual contributions to chi-squared. | 89 |
| 4.33 Setup for radiation tests of FPGAs, not to scale. | 91 |
| 5.1 Current versus dose for XL FPGAs, first irradiation period. | 102 |
| 5.2 Errors versus time since first error for XL FPGAs, first irradiation period. | 103 |
| 5.3 Current versus time for XL FPGAs during annealing. | 104 |
| 5.4 Current versus dose for XL FPGAs, second irradiation period. | 105 |
| 5.5 Errors versus time since first error for XL FPGAs, second irradiation period. | 106 |
| 5.6 Current versus time for XL FPGAs, entire test. | 106 |
| 5.7 Current versus dose for XLA FPGAs, first irradiation period. | 108 |
| 5.8 Errors versus time since first error for XLA FPGAs, first irradiation period. | 110 |
| 5.9 Current versus time for XLA FPGAs during annealing. | 111 |

5.10 Current versus dose for XLA FPGAs, second irradiation period. 112

5.11 Errors versus time since first error for XLA FPGAs, second irradiation
period. 113

5.12 Current versus time for XLA FPGAs, entire test. 114

CHAPTER 1

Introduction

This thesis describes total ionizing dose testing of Xilinx field-programmable gate arrays (FPGAs) for use in the ATLAS experiment. These FPGAs were considered for use in the front end electronics of the ATLAS experiment's liquid argon calorimetry. In chapter 1, a brief overview of the ATLAS experiment, FPGAs, and the requirements which the FPGAs tested would have to satisfy for use at ATLAS are presented. The requirement which is tested in this thesis is tolerance to total ionizing radiation dose. We do not consider the effects of radiation causing single event effects.

In chapter 2, radiation and its interaction with matter are discussed. This chapter concentrates on gamma rays, the type of radiation used in testing the FPGAs. The interaction of radiation with electronics is discussed in chapter 3, along with a discussion of the effects of annealing electronics at elevated temperatures and an overview of previous work in the radiation testing of FPGAs.

Chapters 4 and 5 present the results of radiation testing. Chapter 4 begins with a discussion of pretests which characterized the cobalt-60 source and the use of Fricke dosimetry. The setup and procedure for the radiation tests of the FPGAs are also discussed. Chapter 5 presents the results of the total ionizing dose tests of XC4036XL and XC4036XLA FPGAs. Finally, chapter 6 contains suggestions for further work and other general conclusions.

1.1 The ATLAS Detector

The ATLAS (A Toroidal LHC ApparatuS) detector, shown in figure 1.1, is a general-purpose detector being designed for CERN's Large Hadron Collider (LHC). The LHC will collide proton beams with a centre-of-mass energy of 14 TeV [1]. One of the most important motivations for the ATLAS experiment at the LHC is the search for the Standard Model Higgs boson or Minimal Supersymmetry Higgs bosons. ATLAS must be sensitive to a wide range of processes which would lead to the discovery of the Higgs bosons in the mass ranging from about 80 GeV to 1 TeV. However, most of these processes have very small cross-sections, and it is thus necessary to operate the LHC (and thus ATLAS) at high luminosities (10^{33} - 10^{34} $\text{cm}^{-2} \text{s}^{-1}$, or more) [1].

Figure 1.1, taken from reference [1], shows the subsystems of the ATLAS detector. The magnet systems consist of a superconducting solenoid in the central part of the detector, and three superconducting air-core toroid magnet systems on the outside and on both end-caps. The muon spectrometer subsystem is integrated with the air-core toroid magnets. As the name implies, this subsystem will measure the trajectories and momentum of outgoing muons. The inner detector, enclosed by the solenoid and the electromagnetic calorimeter, uses several types of detectors, including semiconductor detectors and straw tube trackers (cylindrical drift tubes filled with gas). Its purpose is to provide high-precision identification measurements of leptons, photons, and b-jets.

Between the muon spectrometer and the inner detector is the calorimetry for the ATLAS detector, pictured in figure 1.2. Both electromagnetic calorimetry (which allows the identification and reconstruction of electrons and photons) and hadronic calorimetry (which does the same for jets) are used. The ATLAS calorimetry subsystem is divided into four parts. On the outer barrel, hadronic tile

calorimeters consisting of scintillating tiles and iron absorber plates are used. The rest of the calorimeters use liquid argon. The absorber plates in the electromagnetic calorimeters are lead, while copper is used in the hadronic end-cap. The forward calorimeter, which provides both hadronic and electromagnetic calorimetry, uses copper rods in the electromagnetic part and tungsten rods in the hadronic part. Detailed information about the LAr calorimetry is found in reference [2]. The front end electronics (discussed in section 1.3) are located in the crack region between the central hadronic tile calorimeter (the barrel) and the hadronic tile calorimeter close to the end-caps (the extended barrel.)

ATLAS

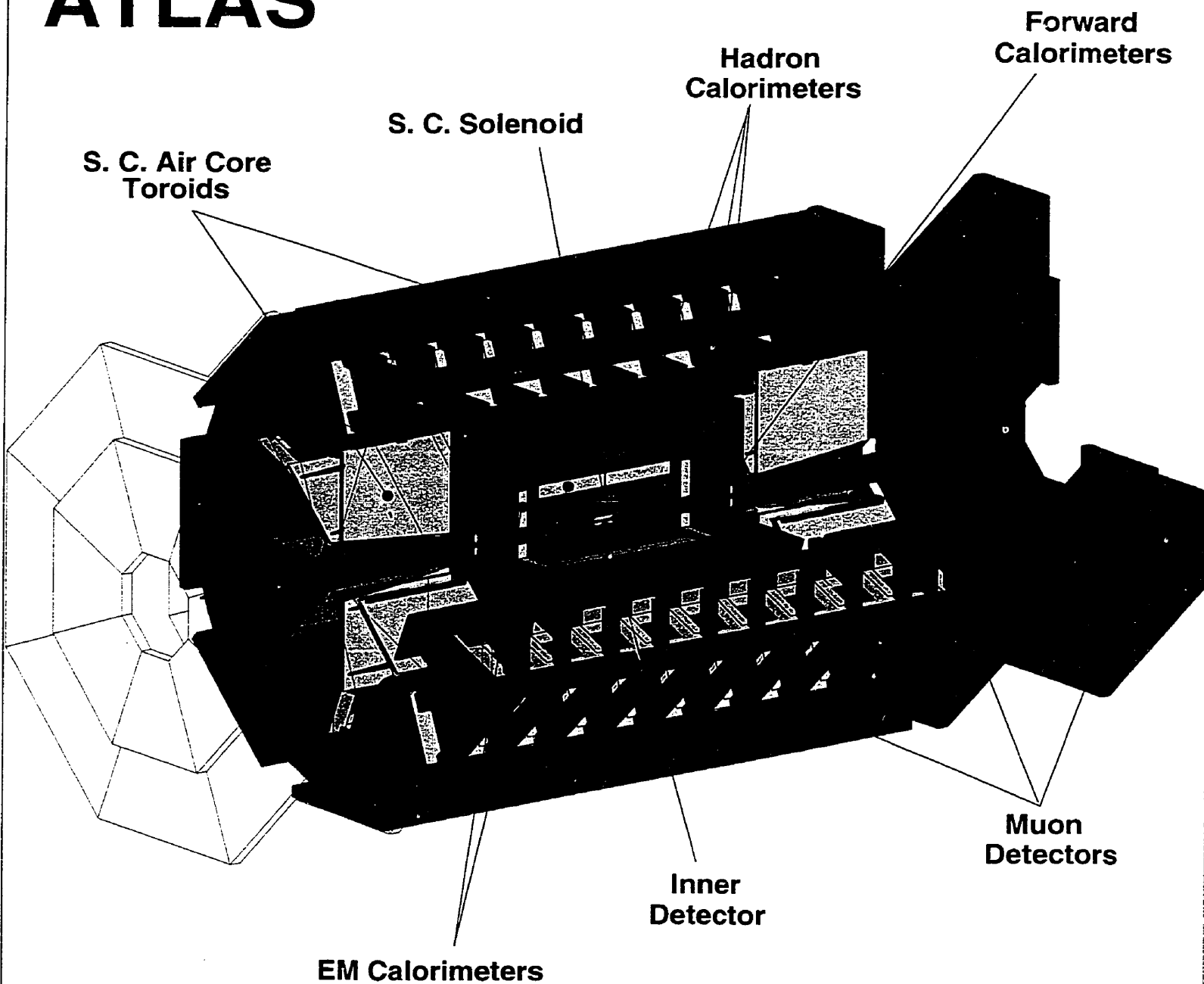


Figure 1.1: The ATLAS detector.

ATLAS Calorimetry (Geant)

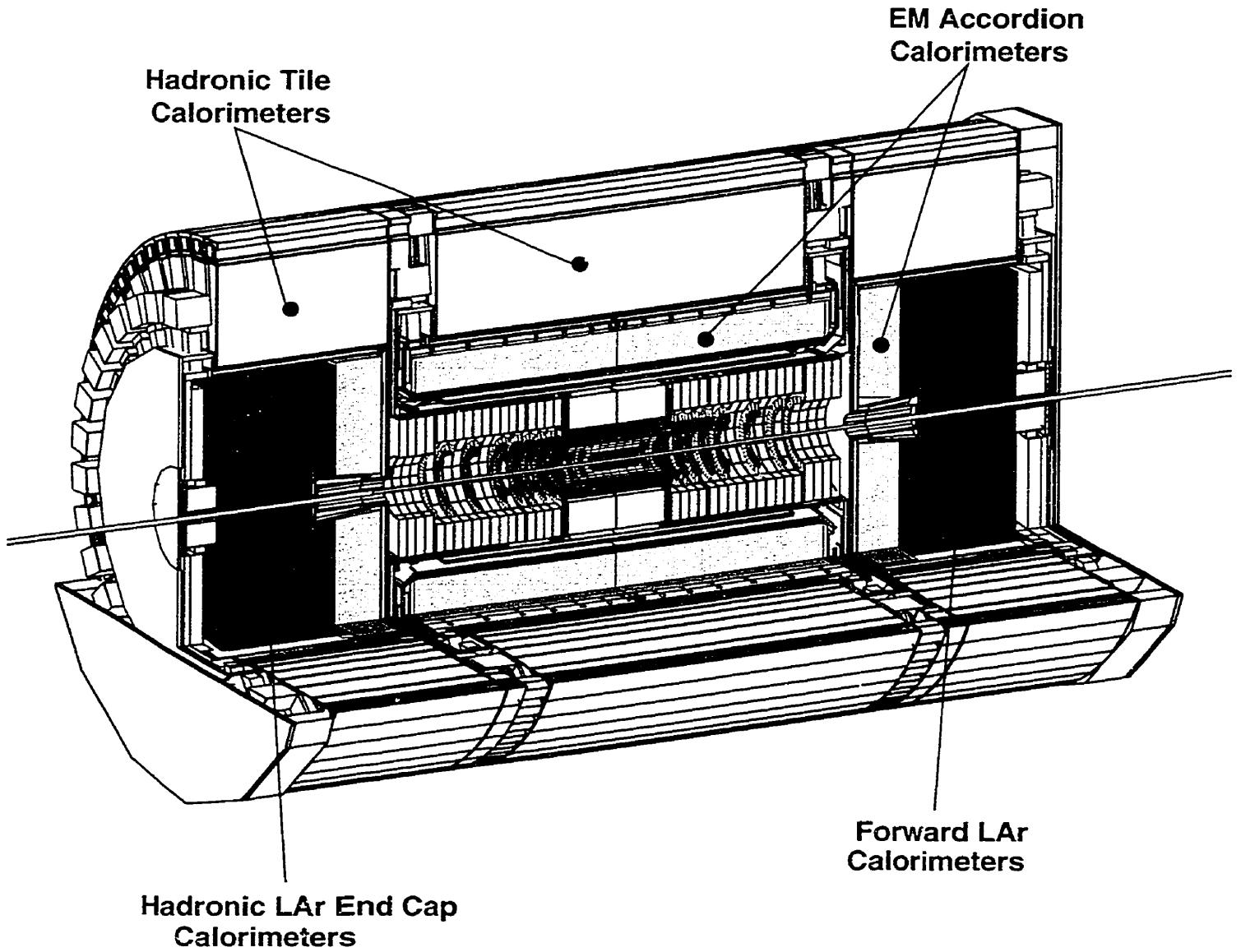


Figure 1.2: Liquid Argon Calorimetry in ATLAS.

1.2 Programmable Logic and Field-Programmable Gate Arrays

Field-Programmable Gate Arrays (FPGAs) are the latest step in the continuing evolution of logic circuits. In the 1960s, small-scale integration (SSI) and medium-scale integration (MSI) technologies provided logic gates, flip-flops, and other basic components at the chip level. The number of gates per component was on the order of 10^2 [3]. As large-scale and very large-scale integration technologies (LSI and VLSI) were developed, gate arrays with 10^4 to 10^5 gates became possible [3]. The Xilinx XC4000 series FPGAs used in these tests have a maximum of 36000 gates, with other members of the family having up to 250000 gates [4].

A field-programmable gate array is simply an array of electronic logic blocks which can have their configurations and connections altered in the field for use in a specific application [3]. SRAM-based FPGAs, such as the Xilinx 4000 series, consist of a static random-access memory (SRAM) control store which connects to an array of functional blocks and their connection network. The FPGA is programmed by an array of transistor switches according to the contents of the SRAM data store.

Figure 1.3 shows a conceptual diagram of the SRAM-based FPGA. An array of configurable logic blocks (CLBs) with an array of configurable interconnections are connected to a SRAM control store on the perimeter of the device. The CLBs are represented in the figure by the rectangular blocks, and the interconnections are represented as a matrix of intersecting lines. Once the configuration, represented on the right as a series of binary digits, is loaded into the control store, the signals from the control store reconfigure the CLBs and the interconnections into the final logic circuit. The CLBs are configured into various logic devices, and interconnections

between them have been made.

The fact that the actual circuits in the FPGA are defined by information in a volatile control store gives SRAM-based FPGAs several advantages. The circuit in the FPGA can be reconfigured and upgraded in the field by changing the contents of the SRAM store. As well, the time between design and implementation is almost instantaneous, especially compared to the weeks between design and manufacture for a conventional integrated circuit. SRAM-based FPGAs, since they are reconfigurable hardware, can combine the versatility of a software-based design with the speed of an application-specific integrated circuit (ASIC). However, any upset to the SRAM (for example, loss of power to the FPGA or damage due to radiation effects) will result in the loss of the device's configuration.

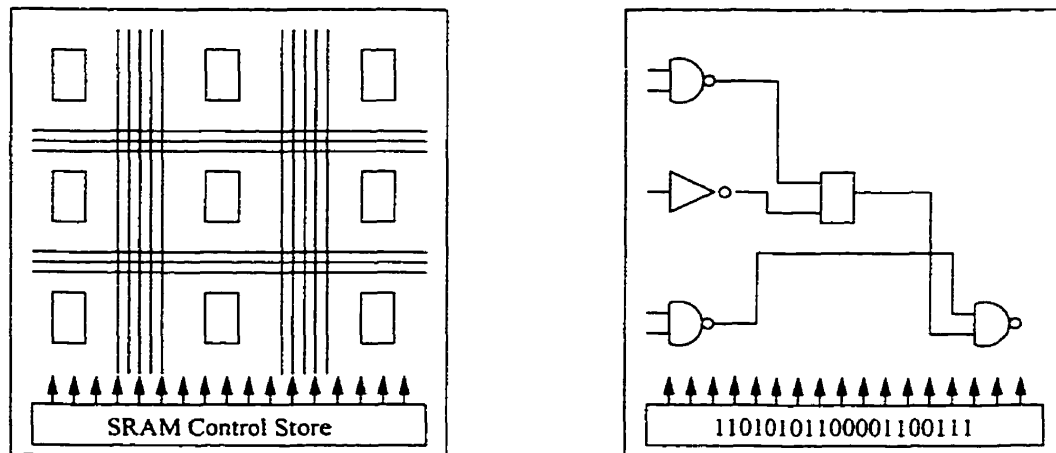


Figure 1.3: Conceptual structure of FPGAs, modeled after reference [3].

FPGAs can also be built which use antifuses for programming. In antifuse-based FPGAs, the configuration of the FPGA is set by applying high programming voltages across antifuses, causing permanent interconnections between logic modules. This contrasts with SRAM-based devices, which are connected via reconfigurable switches. The main disadvantage of antifuse-based FPGAs, such as

those produced by Actel, is that the device can only be programmed once. The antifuse-based FPGAs available also have less RAM than SRAM-based FPGAs do. This smaller amount of RAM is why antifuse-based FPGAs were not considered for ATLAS. However, antifuse-based FPGAs are otherwise capable of higher performance [3]. They are also generally more resistant to radiation effects (see section 3.2).

Other programming technologies are being investigated for use in radiation-resistant FPGAs. Some, like electronically erasable programmable read-only memory (EEPROM) [5] or FLASH-memory [6], will produce FPGAs which can be reprogrammed much like SRAM-based FPGAs. However, after a finite (though large) number of times, these devices cannot be reprogrammed. Special hardware is also needed to program them.

The Xilinx XC4000 series FPGAs, like almost all other FPGAs, are integrated circuits built with CMOS technology. CMOS (for complementary metal-oxide-semiconductor) devices are built using pairs of p-channel and n-channel metal-oxide-semiconductor field-effect transistors. (See section 3.1.)

Xilinx FPGAs have programmable input-output blocks (IOBs) at the perimeter which connect the chip to the outside electronics, a RAM store which stores the device configuration, and an array of CLBs. The XC4036XL and XC4036XLA FPGAs we tested had a maximum of 36,000 logic gates available. Thus, they were denoted as XC4036 devices. Each FPGA had 1296 CLBs in a 36 x 36 matrix.

Two different models of FPGAs were tested. Both types were from the Xilinx XC4000 series of devices. The first four FPGAs were XC4036XL devices, while the remaining three were XC4036XLA FPGAs. The XLA family of FPGAs is an

improved version of the XL devices, with approximately 40% lower power consumption, a smaller die allowing reduced clock delays, lower cost, and overall improved performance [4]. Both types of FPGA were packaged in a 240-pin High Heat Dissipation Quad Flat Pack (HQ240C) package which could tolerate temperatures from -40°C to 100°C [4].

The XLA device is also intrinsically faster than the XL device, as denoted by the different range of speed codes the XLA and XL FPGAs are available in. Xilinx uses two sets of speed codes to show what speed their XC4000 series FPGAs can operate at. The first goes from -4 to -1, with -4 being the slowest. The second ranges from -09 to -07, with -09 being one step faster than -1. XC4036XL FPGAs are available in speed codes ranging from -3 to -08, while the XC4036XLA FPGAs were available in speed codes ranging from -09 to -07 [4]. The XL FPGAs we tested had a speed code of -1, while the XLA FPGAs had a speed code of -09.

The XC4036XL was chosen because it was just large enough (i.e., had enough logic gates) for use as an SCA controller. At the time testing began, it was the state of the art, being the only FPGA available with dual-ported RAM. Xilinx FPGAs were also chosen because their RAM can be configured to almost arbitrary size. Since this project began, Xilinx continued to develop more sophisticated FPGAs, such as the XC4036XLA devices tested in the later part of this project, and the newer Virtex series FPGAs. Altera also offers an FPGA with dual-ported RAM, although its RAM sizes are fixed. Its radiation resistance would probably be similar to the Xilinx FPGAs tested, as it is also produced in a commercial sub-micron CMOS process.

Radiation hardened Xilinx FPGAs have also been produced, such as the XQR4036XL. This device is based on the XC4036XL, but was specifically modified

to resist radiation. The XQR4036XL is only available in the -3 speed code [4]. Hence, it is too slow for use by ATLAS. A radiation hardened version of the Virtex FPGAs, the XQVR300, has recently been developed. This device is not yet on the market.

1.3 Front End Electronics

1.3.1 Analog Memory in Front End Electronics

One of the University of Alberta's main contributions to the ATLAS project is design and testing of the front end electronics for the Liquid Argon (LAr, or LARG) calorimeters. These electronics must be installed in the vicinity of the detector, despite the limited space, limited accessibility, and significant radiation field. This is because the necessary low level of coherent noise and ability to handle large dynamic range in the signals would not be possible if the preamplifiers were not very close to the detector [2]. Thus, while much of the digital electronics will be in a control room hundreds of metres from the detector, preamplifiers, shapers, analog-digital converters (ADC), switched capacitor arrays (SCAs), and the digital control logic will be on the detector.

A schematic of the front end electronics is shown in figure 1.4. Signals from the calorimeter cells are amplified by the preamplifiers and the shapers, and are sampled at 40 MHz. These samples are stored in an SCA analog memory chip. Each SCA stores the signals from four calorimeter channels at three different amplifier gain levels, as well as a reference channel. The gain selector chip is responsible for determining which gain scale needs to be applied to the signal. Each channel contains 144 analog storage cells. The design allows for random access to each cell, with the SCA controller chip controlling which cells are available to be written to and which can be digitized by the ADCs [2].

When a level-1 trigger accept signal is received, the samples are read from the SCA and digitized by a 12-bit analog-digital converter. The digitized signals are sent directly over optical links to the read-out driver (ROD), a large digital memory

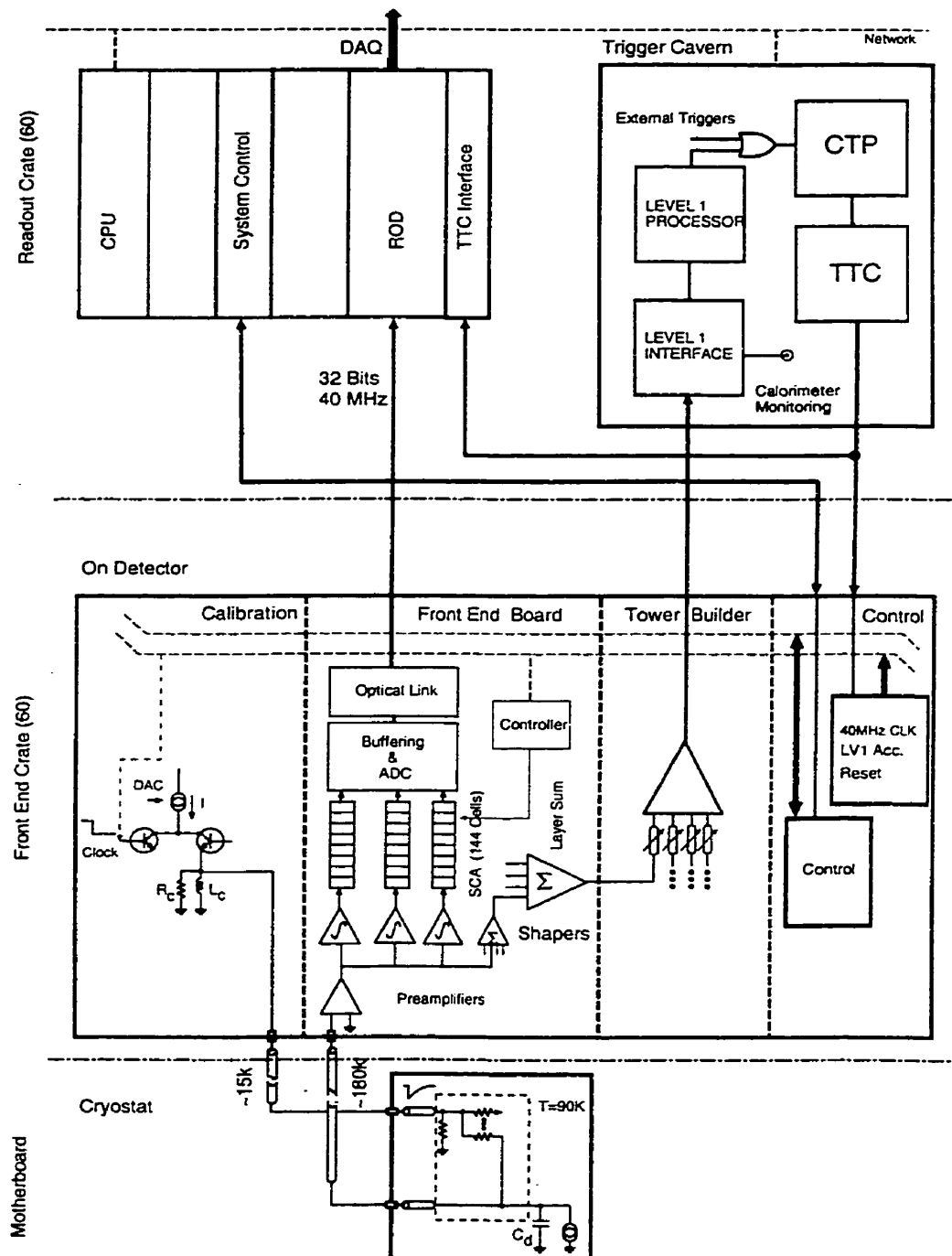


Figure 1.4: Diagram of read-out electronics, from reference [2].

buffer. Tests of the effects of radiation and temperature on SCAs have previously been carried out by our group [7].

1.3.2 FPGA Implementation of the SCA Controller

The design of the SCA controller for the front end board is described in detail in reference [8]. The controller on the front-end board is responsible for addressing the SCAs and sending information to the gain selector logic. The components the controller must communicate with are shown in figure 1.5. The SPAC (Serial Protocol for the ATLAS Calorimeter [9]) is responsible for handling communications between the front end electronics and the run control systems. The TTC (Trigger Clock and Control) system is responsible for delivering the triggering and timing information to the front end electronics. The gain selector reads out the SCA, controls their digitization by the ADCs, and selects the gain scale applied to the signals.

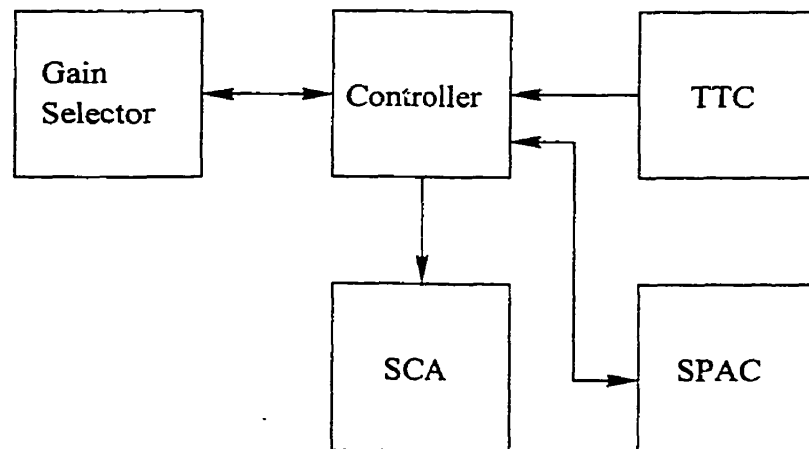


Figure 1.5: Communications with the SCA controller.

The controller should, as far as is possible, be fast enough that the front-end boards can be operated without significant dead-time. To operate the SCAs, the

controller must provide the SCA an 8-bit parallel write address every 25 ns (keeping them in sequential order if possible) and five 8-bit serial read addresses at a rate of 75 kHz [8]. The current design of the system must be upgradable to a trigger rate of 100 kHz [8]. For each trigger, the controller has to send the SCA addresses for each time sample, as well as the bunch-crossing number for the first sample, to the gain selector which then injects them into the data stream [8]. The controller must also provide a register of errors when problems arise, such as when no storage locations are available in the SCA. It must also be able to make SCA addresses unavailable for writing. Finally, it must deal with overlapping events (where another trigger occurs before the first event has been processed) by signalling the gain selector to keep the gain fixed for the next event.

A block diagram of the circuit for the SCA controller is given in figure 1.6. The read and write addresses for the SCAs are managed using a series of four FIFO (First In, First Out) memories, synchronized with the 40 MHz clock. The first lists available SCA addresses, the second lists the addresses of SCA cells which have been written to and await the level-1 trigger, the third lists the addresses selected by the trigger and waiting to be read and digitized, and the last lists the addresses which have been digitized and can be added to the list of available addresses. Since the read and write switches of the SCA are controlled independently, the system can deal with 75 kHz Level-1 trigger rates and still have less than 0.5% dead time [2].

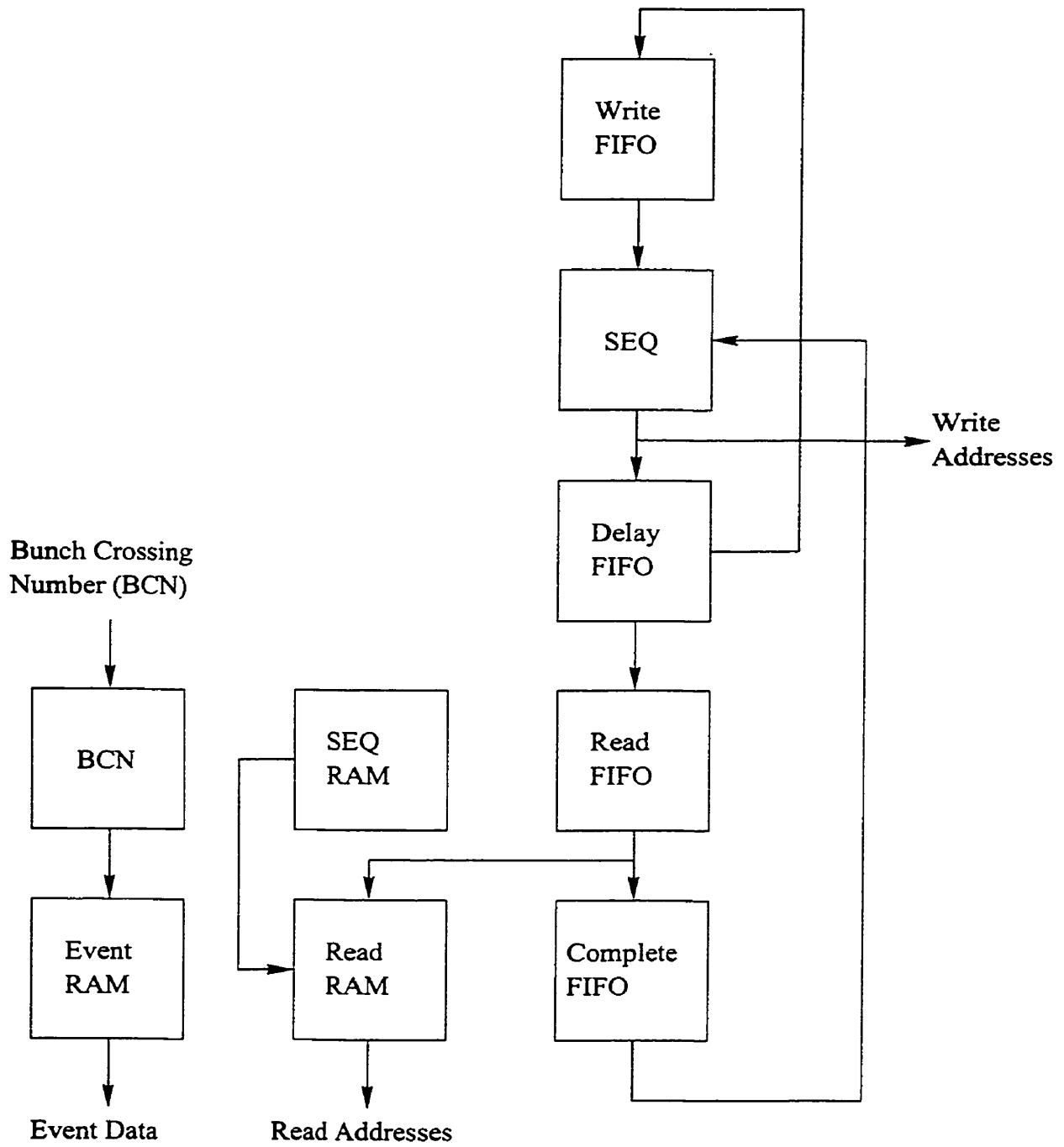


Figure 1.6: Block diagram of the SCA controller.

The controller also Grey encodes the addresses before reading and writing. This is done to reduce the digital noise. Since Grey encoding is only useful if the addresses are generated in order before encoding, the controller must put the addresses in sequence as well. Hence, a sequencing step is put between the write and delay FIFOs. After sequencing, the controller sends the SCA a sequenced and encoded list of available write addresses.

When a trigger signal is received, the SCA addresses from the read FIFO are arranged in sequence by the SEQ RAM, and sent to to the read RAM. The readout order is sequenced so that the sample at the pulse's peak is read by the gain selector first. This maximum sample allows the gains to be compared and the correct gain to be chosen. Likewise, the bunch-crossing number is sent to the event RAM. The contents of the event and read RAM stores are sent to the gain selector logic. Finally, the controller also sends status bits to the gain selector logic if the addresses are out of sequence, triggers are being ignored, or the current trigger occurred within a set number of nanoseconds of the last trigger.

At the beginning of the run, trigger delay time, number of time samples, and available SCA addresses are downloaded to the controller. The controller will receive these parameters from the SPAC. If an FPGA is used as the controller, the circuit configuration and the control parameters will be downloaded separately [8]. Bits in the control parameters are also used to put the controller in particular diagnostic modes – for example, Grey encoding of the SCA addresses can be bypassed, or a single SCA address can be read to the exclusion of all others.

The controller will consume about 1.2 W of power [8], a small fraction of the total power consumption of the front end board, so cooling should not be a major concern even if commercial packaging is used.

The controller design has been prototyped using XC4036X-series FPGAs. The design of the circuit used in testing was done using schematic diagrams, while Xilinx tools were used to translate the schematics into the connections and configurations of the logic blocks in the FPGA.

The University of Alberta has built a series of controller prototypes since 1993, with the first version implemented with an FPGA made in 1997. The XC4025E and XC4028E FPGAs were too slow to operate at the full 40 MHz clock speed, so dual FIFOs operating at different phases of a 20 MHz clock were used to get the circuit operating at effectively 40 MHz. The XC4036XL and XC4036XLA FPGAs are fast enough to run at nearly 60 MHz without using dual FIFOs [8]. 100 controllers have been used at ATLAS testbeams to date.

1.4 Radiation Environment in ATLAS

Due to the high luminosity of the LHC, all components of the ATLAS detector must be able to resist significant levels of radiation without being damaged or polluting the surroundings. The radiation fluxes throughout the ATLAS detector have been estimated using simulations. Numerous tests have been done, and continue to be done, by members of the ATLAS collaboration on prototypes of electronics and other hardware to ensure that all parts of ATLAS will survive 10 years of operation without failure due to irradiation.

Table 1.1 summarizes the fluxes of various types of radiation in the crack region, according to reference [10]. These fluxes have been determined through simulations. Within the crack region, where the front-end electronics are located, the radiation flux of any given particle type can vary by up to a factor of ten. These results do not include the safety factors necessary for determining the level of radiation tolerance of electronics and other components in ATLAS.

| Type of Radiation | Flux (kHz/cm ²) |
|-------------------------|-----------------------------|
| Neutrons above 100 keV | 10 ¹ |
| Total Neutrons | 10 ² |
| Photons above 300 keV | 10 ¹ |
| Photons above 30 keV | 10 ² |
| Electrons | 10 ⁰ |
| Muons | 10 ⁻¹ |
| Total Charged Particles | 10 ⁰ |

Table 1.1: Approximate radiation levels in the crack region of ATLAS.

The results for the flux of photons and charged particles can be used to find the total ionizing dose rate in ATLAS. In the part of the crack region with the

highest radiation levels, the dose rate for electronic devices has been simulated to be 2.0 krad/yr [11], with a 5% statistical error. (See section 2.3 for the definitions of the units of dose.) An additional systematic safety factor of 4 is also taken into consideration in computing the required level of radiation tolerance required by ATLAS electronics [11]. This safety factor is required to take into account both inaccuracy in the simulations and possible variations from lot to lot of the electronics used. This results in a total dose requirement over ten years of operation in ATLAS of 80 krad.

While several technologies exist which are guaranteed to be radiation resistant, or “radiation hard”, commercial devices which are not designed for radiation environments are generally cheaper and faster. Therefore, standard commercial devices are preferred over devices custom-built to be radiation hard, if they can also withstand the radiation in ATLAS.

CHAPTER 2

Ionizing Radiation

Gamma rays from a cobalt-60 source were used to irradiate the FPGAs. This chapter discusses types of radiation, cobalt-60 sources, the interaction of gamma rays with matter, and the use of Fricke dosimetry to measure the absorbed dose from gamma rays.

2.1 Types of Radiation

All radiation can be divided into two main categories – non-ionizing radiation and ionizing radiation. Charged hadrons and leptons, heavy ions, and photons are considered ionizing radiation, as they can ionize an atom through electromagnetic interactions. Neutrons and other neutral hadrons do not ionize atoms, and are therefore non-ionizing radiation. This thesis deals with the effects of ionizing radiation, specifically gamma rays, on electronics.

Neutral particles, such as neutrons, interact with matter through non-ionizing energy loss mechanisms. In the case of neutrons with energy in the MeV range, the primary mechanism for energy loss is elastic scattering from atomic nuclei [12]. This results in displacement of the atom in the lattice of the material.

For neutrons with sufficient energy to excite the nucleus, inelastic scattering may also occur. This leaves the nucleus in an excited state which may later decay by emitting gamma rays or other radiation. Low energy neutrons with energy in the eV to keV range may undergo nuclear reactions such as radiative neutron capture [12]. This may also result in an unstable nucleus, which will alpha or beta decay. Although the neutrons themselves do not ionize atoms, they may produce unstable nuclei which will produce ionizing radiation.

Gamma rays and other high-energy photons interact with matter in three ways: the photo-electric effect, the Compton effect, and pair production [13, 12]. The interaction of gamma rays with matter is more fully described in section 2.3. The photo-electric and Compton effects result in the ejection of energetic electrons and the ionization of atoms. Pair production produces electron-positron pairs. The energetic electrons and positrons from these three processes are responsible for most

of the ionization of the material.

Charged particles can also ionize atoms. For the purposes of radiation effects, charged particles can be divided into light particles (electrons and positrons) and heavy particles (muons, hadrons, and nuclei) [12]. These charged particles will lose their energy through inelastic collisions with atomic electrons and elastic scattering from nuclei. Heavy charged particles lose most of their energy through inelastic collisions with electrons [12]. These collisions will excite the atomic electrons. If enough energy is transferred from the heavy particle to the electrons in the collisions, ionization results. The recoil electrons may also have enough energy to cause secondary ionization. The effects of elastic scattering of heavy charged particles from nuclei is similar to the effects of neutrons colliding with nuclei, resulting in atomic displacements.

Electrons and positrons also lose energy from collisions with atomic electrons in much the same way as heavier particles. Since they have a much smaller mass, however, they are also subject to energy losses from bremsstrahlung (electromagnetic radiation emitted by the electron as it loses energy through interaction with the electric field of an atomic nucleus). Bremsstrahlung is a minor factor for electrons with energies below a few MeV, but dominates energy loss from collisions for electrons with energies of a few tens of MeV [12]. Through colliding with atomic electrons, free electrons will ionize more atoms until they lose enough energy from collisions that they fall below the ionization threshold energy. In the meantime, secondary electrons from previous collisions or bremsstrahlung photons will cause secondary ionization.

In this thesis, ionizing radiation effects using cobalt-60 gamma rays were considered, to the exclusion of other radiation effects on electronics. This is because

all radiation effects can be divided into ionizing and non-ionizing effects. Hence, it is possible to study the effects of total ionizing dose in isolation from non-ionizing effects. A gamma-ray source was used because other sources of radiation, such as proton or heavy ion beams, would cause non-ionizing radiation effects as well as ionizing radiation effects. The cobalt-60 source used was also readily available and inexpensive to operate, since no power needed to be supplied to the source for it to irradiate the devices under test. Its main disadvantage was its low dose rate. Electron or positron beams and X-ray sources would also be good sources of ionizing radiation without non-ionizing radiation effects, but they were not available for these tests. They would also be more expensive to operate than a cobalt-60 source.

2.2 Cobalt-60 Sources

One of the standard gamma-ray sources used in radiation testing of electronic devices is cobalt-60. Cobalt-60 is an unstable isotope with 27 protons and 33 neutrons, which beta-decays into nickel-60. The energy level diagram for this decay is shown in figure 2.1. The beta particle (β) emitted has a maximum energy of 0.314 MeV, and an average energy of 0.093 MeV. The half-life of this decay is 5.27 years [14]. The resulting nickel nucleus is usually in an excited state, which quickly decays into a stable state by emitting a 1.173 MeV photon (γ), followed by a 1.332 MeV photon. For many purposes, a mean gamma energy of 1.25 MeV is used in calculations. Less than one in 10^6 cobalt-60 nuclei beta decay directly into the ground state of nickel-60 [13].

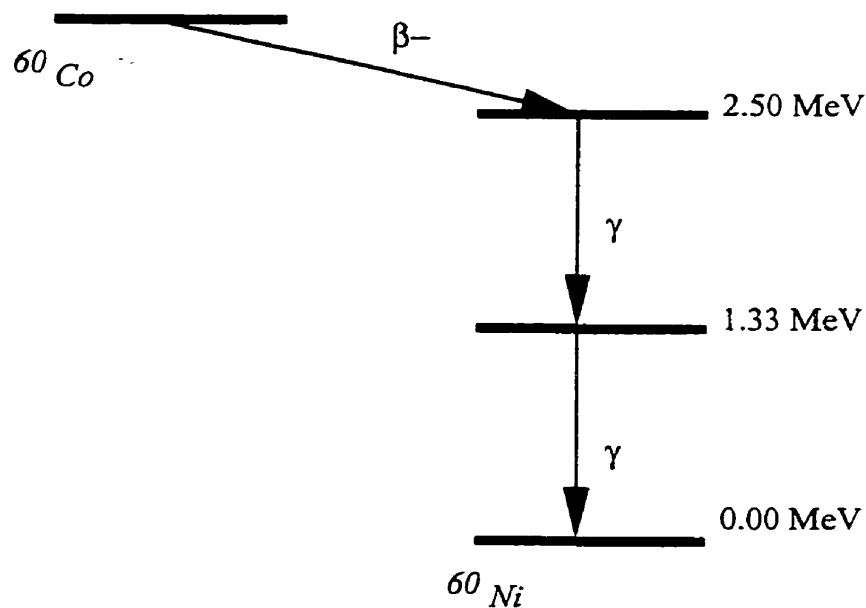


Figure 2.1: Dominant decay scheme of cobalt-60

Nickel-60 is a stable isotope, so a pure cobalt-60 source will not produce any radiation other than those from cobalt-60 beta and gamma decay. However, the

interaction of the beta and gamma particles produced by cobalt-60 with the environment through Compton scattering and pair production will produce a spectrum of particles [15].

There are two main types of cobalt-60 sources: cavity-type sources and cave-type sources. In cavity sources, the cobalt-60 irradiates a cavity surrounded by shielding material (usually lead). Samples to be irradiated are placed inside the cavity. Movable shielding is used so that the sample can be introduced without exposing the cobalt-60.

In a cave source, the shielding is immobile, but the source is movable. In cave sources, the cobalt-60 is kept in a shielded container. The sample to be irradiated is placed in a small room, or cave, and the source is moved out of its container and into the cave. Since the source is exposed unshielded in the cave, the cave must also be shielded from the outside environment, usually with concrete walls. The cave's entrance is also isolated from the radiation area by building the cave in the form of a labyrinth.

The cobalt-60 source used in this research is a cave source, located in the basement of the Chemistry building at the University of Alberta. Figure 2.2 shows the cobalt-60 source used. When not in use, the source is kept in a lead-lined source house, or "hutch." This source is attached to a steel push rod, which is operated from outside the radiation area. The push rod is used to move the source along a track leading out of the hutch, so that the samples in the radiation area can be irradiated. A bench is located in front of the source's extended position, so that an experiment can be set up in front of it.

The radiation area is located at the end of a concrete corridor, which is locked

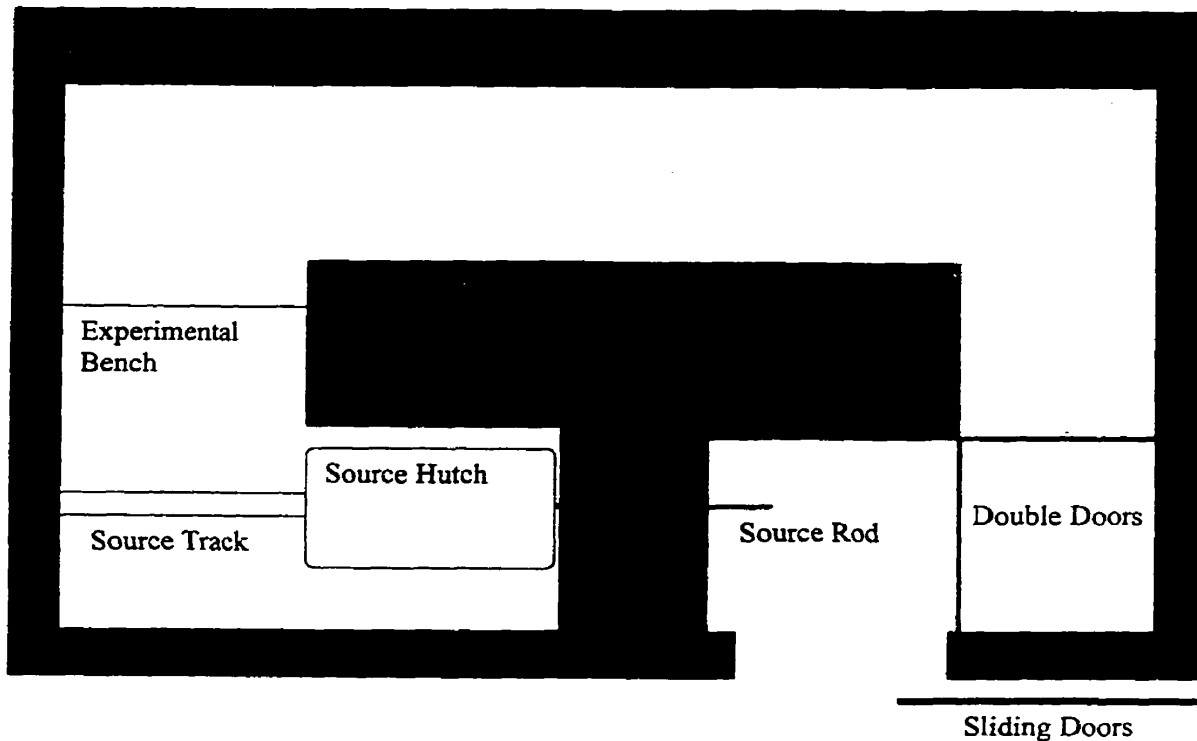


Figure 2.2: Cave-type cobalt-60 source at the University of Alberta, not to scale.

off with two metal doors when the source is out. The corridor also has two right-angle turns, so that the entrance (where the experimental equipment which is not irradiated is kept) is not in the line of radiation. When the sample to be irradiated is ready, the doors are locked, and the source is pushed out of its hutch. In this thesis, the source is referred to as “on” when it is pushed out of its hutch, and “off” when it is retracted.

2.3 Interaction of Gamma Rays With Matter

Photons in the keV to MeV range produced by the de-excitation of nuclei are referred to as gamma rays. Photons produced by atomic deexcitation, with energies in the eV to keV ranges, are referred to as X-rays. These photons interact with matter in three ways: photo-electric effect (the primary means of interaction for low-energy X-rays), the Compton effect (which is more important for high-energy photons), and pair production (which is only possible for photons with energy greater than 1.022 MeV, or twice the mass of the electron [13, 12]).

In the photoelectric effect, a photon is completely absorbed by an atomic electron, which is then ejected from the atom with an energy equal to the photon's energy minus the binding energy of the electron. This must involve an atomic rather than a free electron, as the recoil of the nucleus is needed to take care of conservation of momentum.

In Compton scattering, a photon interacts with a free electron (or a bound electron, if the photon energy is much larger than the binding energy), resulting in an electron and photon of reduced energy scattered off at an angle. The energy of the scattered electron and photon depends on the scattering angle.

Pair production involves the production of an electron-positron pair from a photon. For momentum to be conserved, a third body, such as an atomic nucleus, is required. Cobalt-60 gamma rays of average energy 1.25 MeV are of sufficient energy for pair production to occur.

The total cross section per atom for a photon interacting with matter is thus

$$\sigma = \sigma_{photo} + \sigma_{Comp} + \sigma_{pair}. \quad (2.1)$$

σ_{Comp} can be expressed as the sum of two cross sections [13, 12]:

$$\sigma_{Comp} = \sigma^a + \sigma^s, \quad (2.2)$$

where σ^a is the Compton absorption cross-section, and σ^s is the Compton scattering cross-section. σ^s/σ_{Comp} is the average fraction of the original photon's energy E which is contained in the scattered photon, while σ^a/σ_{Comp} is the average fraction of E which is contained in the recoil electron.

For a photon beam of intensity I (in units of energy per unit time and unit area), where

$$I = \Phi E \quad (2.3)$$

and Φ is the flux of photons per unit time and unit area, the flux of primary photons lost through the three photon interactions through a distance dx is

$$d\Phi = \Phi N(\sigma_{photo} + \sigma_{Comp} + \sigma_{pair})dx \quad (2.4)$$

where N is the density of atoms. This translates to a loss in intensity of

$$dI = \Phi EN(\sigma_{photo} + \sigma_{Comp} + \sigma_{pair})dx = I\mu dx, \quad (2.5)$$

where μ is the total absorption coefficient, defined as

$$\mu = N\sigma = \sigma(N_a\rho/A), \quad (2.6)$$

with ρ the material density, N_a Avogadro's number, and A the atomic mass [12]. μ/ρ is the more commonly tabulated value, as this quantity is independent of the physical state of the substance. For chemical compounds or mixtures of materials, μ/ρ can be calculated using Bragg's rule,

$$\frac{\mu}{\rho} = \sum_{i=1}^n w_i \frac{\mu_i}{\rho_i}, \quad (2.7)$$

with w_i being the weight fraction of element i in the compound or mixture [13, 12]. Reference [16] has μ/ρ values tabulated for most of the chemical elements as well as an extensive selection of chemical compounds and mixtures (such as air and concrete).

The attenuation of a beam of photons after passing through a thickness x of material then becomes [13, 12]

$$I(x) = I_o e^{-\mu x} = I_o e^{(-\mu/\rho)\rho x}. \quad (2.8)$$

where $I(x)$ is the intensity of the beam after a distance x , and I_o is the initial intensity.

In all three energy-loss mechanisms, the primary photons lose energy and produce secondary electrons (and positrons in the case of pair production). These electrons and positrons lose their energy primarily through collisions with atomic electrons [12].

Note that μ is the attenuation coefficient for absorption of primary photons only, and equation 2.8 gives the intensity of the beam of original photons only. It can be used to find the attenuation of the original beam of photons of energy E , neglecting all secondary particles. However, in Compton scattering, only a fraction

of the primary photon's energy is transferred to the electron. As well, photons of lower energy than E can be scattered via multiple collisions back into the direction of the original beam.

When assessing radiation damage on electronic devices, the relevant quantity is the total absorbed dose, D . D is defined as the total energy absorbed by a medium due to irradiation per unit mass. Thus, the relevant constant for the purposes of assessing the attenuation of the ionizing dose rate from a gamma ray source is not μ , but μ_{en} , the energy absorption constant.

To calculate μ_{en} , the relevant quantity is the energy transferred to the secondary electrons produced by the incident photons. In the photoelectric effect, this is simply E minus the binding energy of the electron E_b . For pair production, each electron-positron pair has a total energy of $E - 2m_e$. In the Compton effect, the recoil electron has an average energy of $E(\sigma^a/\sigma_{Comp})$. Thus, equation 2.5 is replaced by [13]

$$dI = \Phi N(\sigma_{photo}(E - E_b) + \sigma_{Comp}(E \frac{\sigma^a}{\sigma_{Comp}}) + \sigma_{pair}(E - 2m_e))dx. \quad (2.9)$$

In the approximation where E_b and m_e are neglected, this is simply [13]

$$dI = \Phi NE(\sigma_{photo} + \sigma^a + \sigma_{pair})dx = I\mu_{en}dx, \quad (2.10)$$

which leads to

$$I(x) = I_0 e^{-\mu_{en}x} = I_0 e^{(-\mu_{en}/\rho)\rho x}. \quad (2.11)$$

For cobalt-60 gamma rays, the Compton effect dominates, and the cross-sections for the photoelectric effect and pair production are comparatively low. In fact, the cross-section for pair production is negligible [13]. Thus, even though $2m_e$ is not really negligible with respect to E , this exponential approximation can be used.

Dose is defined as the energy transferred to a medium due to ionization per unit mass. The usual units for dose are the Gray (Gy), which is defined as 1 J/kg, and the rad, which is equal to 100 erg/g or 0.01 Gy. The dose rate can be calculated from the intensity of the photon beam using the simple relation [13]

$$\frac{dD}{dt} = I \frac{\mu_{en}}{\rho}. \quad (2.12)$$

Note that the dose rate from a gamma source of a given intensity varies according to the atomic composition and the density of the medium.

Since σ_{photo} is proportional to Z^n (where n is approximately 4.5) when E is in the MeV energy range, σ_{Comp} is roughly proportional to Z , and σ_{pair} is proportional to Z^2 [13], the total interaction cross section, and thus the attenuation constant, increases for high Z materials. This is why dense materials with high atomic numbers, such as lead, are extensively used in radiation shielding.

There is one problem with the use of high Z materials as shielding, however: the existence of “backscattered” radiation. The low-energy secondary electrons produced by photon interaction are susceptible to scatter from atomic nuclei and will be deflected at large angles. The possibility of an electron being reflected from the surface of an absorber increases for high Z nuclei [12]. As a result, if primary or secondary photons interact with the air inside an enclosure surrounded by a high Z

material (as was the case in the tests described in subsection 4.1.3 and chapter 5), backscattered electrons may be reflected into the cavity. Thus, the dose received at the centre (where dosimeters or electronics are undergoing tests) will be increased, and will not be purely the result of photons.

In these tests, backscattered radiation was reduced by adding a second layer of shielding around the dosimeters and electronics. This shielding was thick enough to stop the low-energy backscattered electrons. The shielding was also made of aluminum, a low Z material, so it was not a major source of backscattered radiation. Figure 2.3 shows the use of low- Z shielding to stop backscattered radiation.

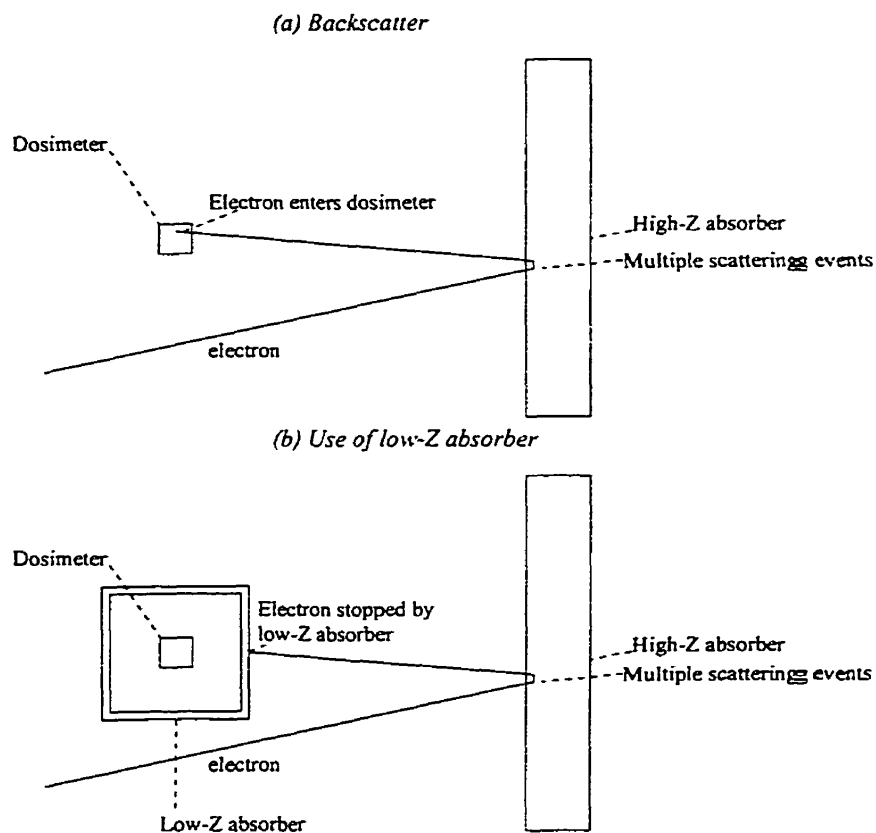


Figure 2.3: Backscattering of electrons, and use of low- Z shielding

2.4 Dosimetry

Dosimetry is simply any method for determining the dose of radiation absorbed by a material. During the course of this work, two dosimetric techniques were used. The first, Fricke dosimetry, measures dose rate by measuring the change in a solution's infrared absorption caused by radiation-induced chemical changes. The second, thermoluminescent dosimetry, measures total absorbed dose by examining the light given off by an irradiated crystal after heating.

2.4.1 Fricke Dosimetry

During the radiation tests of the Xilinx FPGAs, Fricke dosimetry was used in order to determine the dose rate at the position of the FPGA die. Fricke dosimetry is carried out by examining the infrared absorption of a vial of Fricke solution which has been exposed to ionizing radiation, such as cobalt-60 gamma rays. The infrared absorption of the solution depends on both the temperature and the dose absorbed by the solution.

The Fricke solution used in this experiment contained 0.0780 g of ammonium ferrous sulphate ($(\text{NH}_4)_2\text{SO}_4 \cdot \text{FeSO}_4 \cdot 6\text{H}_2\text{O}$) and 4.4 ml of sulphuric acid (H_2SO_4), in 200 ml of solution. Often, chloride ions are added to the solution in order to inhibit the oxidation of ferrous ions by organic impurities [14]. However, as nanopure water was used in this solution, the level of organic impurities was considered to be low enough that this was not required.

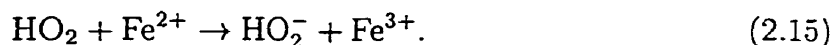
Fricke dosimetry is based on the oxidation of ferrous ions (Fe^{2+}) to ferric ions (Fe^{3+}) in the presence of oxygen, under the influence of ionizing radiation [14, 17]. Fricke first proposed this system in 1929 [14], using 0.4 M sulphuric acid so that the

x-ray response would be the same as that of standard air ionization chambers.

The basic reactions involved are as follows. As ionizing radiation passes through the dosimeter solution, electron-ion pairs are formed. The free electrons can react with the hydrogen ions in the solution as follows [17]:



In an acidic solution – one with a high concentration of hydrogen ions – this reaction occurs very quickly. For a solution with 0.8 mol/l sulphuric acid, it is complete in less than 10^{-9} s [17]. In an aerated solution, this is succeeded by [17]



Once all of the dissolved oxygen is used up, the HO_2 radical can no longer be formed. Thus, conversion of ferrous ions to ferric ions is inhibited. In air-saturated water, a dose of 40 to 50 krad will use up all of the oxygen in standard Fricke solution [17, 14]. As well, a dose of about 4 krad is necessary to produce noticeable changes in absorbtion [14]. The resulting useful range of 4 to 50 krad covers enough of the range in total absorbed dose of interest in these experiments to accurately determine the dose rate from the cobalt-60 source. The non-linearity due to saturation at high dose levels, and the small change in absorbtion at low dose levels, was seen in the Fricke dosimetry done for both the pretests and the FPGA tests (see section 4.2 and chapter 5.)

Absorbed dose in the dosimeter vials is determined by measuring the optical density at 304 nm, the wavelength of maximum absorbtion for ferric ions. This is

done using a spectrophotometer. The optical density is adjusted by subtracting the optical density of a dosimeter vial which is kept out of the radiation area, but at the same temperature. The optical density of the vial is substituted into the equation for dose (in air) per unit time, dD/dt [14]:

$$\frac{dD}{dt} = \frac{9.56 \times 10^8}{\Delta\epsilon d \rho G(\text{Fe}^{3+})} \frac{d(\Delta A)}{dt}, \quad (2.16)$$

where ΔA is the difference between the optical density, A , of an irradiated dosimeter and that of a dosimeter before irradiation, d is the optical path length through the dosimeter, ρ is the density of the dosimeter, $G(\text{Fe}^{3+})$ is the number of ferric ions produced per 100 eV of absorbed energy from ionizing radiation, and $\Delta\epsilon$ is the difference between molar extinction coefficients of ferric and ferrous ions. The following parametrization is used for the change of $\Delta\epsilon$ with temperature:

$$\Delta\epsilon = [\Delta\epsilon_{25^\circ\text{C}}(1 + 0.007 \text{ C}^{-1}(T - 25^\circ\text{C}))]. \quad (2.17)$$

The parameters used during these measurements are shown in table 2.1.

| | |
|---------------------|---------------------------------------|
| $\Delta\epsilon$ | 2201 \pm 9 l/mole·cm at 25°C, |
| d | 1.00 \pm 0.00 cm, |
| ρ | 1.024 \pm 0.001 g/cm ³ , |
| $G(\text{Fe}^{3+})$ | 15.5 \pm 0.2 molecules/100 eV. |

Table 2.1: Parameters used to calculate dose rate using Fricke dosimetry.

This results in the equation for dose rate (using rad as the unit of dose):

$$\frac{dD}{dt} = \left(\frac{6.08 \times 10^7}{(2201 \frac{1}{\text{mol}\cdot\text{cm}})[1 + 0.007(T - 25^\circ\text{C})]} \right) \left(\frac{d(\Delta A)}{dt} \right). \quad (2.18)$$

The optical density of the background dosimeter was subtracted from that of the irradiated dosimeters. The standard deviation of the optical density measurements of all of the dosimeters before irradiation was used as an estimate of the error in the optical density measurements for the irradiated dosimeters. Finally, the equation

$$D = \left(\frac{6.08 \times 10^4}{(2201 \frac{1}{\text{mol-cm}})[1 + 0.007(T - 25^\circ\text{C})]} \right) (A_{\text{irradiated}} - A_{\text{background}}) \quad (2.19)$$

was used to find the absorbed dose (in krad) in the dosimeter, and the best-fit line of a dose versus time plot was used to find the dose rate.

Note that, even at the same distance from the same source of radiation, the absorbed dose is different for different materials. Thus, in our tests, it was necessary to correct the absorbed dose by calculating the ratio of the energy absorption coefficients, μ_{en}/ρ , in the Fricke solution and the FPGA die. These coefficients were found in reference [16]. For cobalt-60 gamma rays with an average energy of 1.25 MeV, the correction factor is

$$\frac{(\mu_{en}/\rho)_{Si}}{(\mu_{en}/\rho)_{Fricke}} = \frac{2.652 \times 10^{-2}}{2.955 \times 10^{-2}} = 0.90, \quad (2.20)$$

where silicon is used as the material of the FPGA die. There is a difference of less than 0.4% between the correction for Si and SiO₂.

2.4.2 Thermoluminescent Detector Dosimetry

The use of thermoluminescent detectors, or TLDs, is another common method of dosimetry. TLDs are inorganic crystals, such as lithium borate manganese, with

a high concentration of trapping centres within the band gap. When exposed to ionizing radiation such as the gamma rays from cobalt-60, electrons are excited from the conduction band to the valence band, and are captured at a trapping centre. If the trap energy level is far enough below the conduction band, the electron is unlikely to return to the conduction band at room temperatures. An analogous process serves to trap holes [18].

The measurement of total absorbed dose in TLDs is done by heating the crystals to 300°C. This provides enough thermal energy for the trapped electron-hole pairs to recombine, radiating a photon in the process. The total number of photons emitted is proportional to the dose absorbed by the TLD [18]. This process also “zeroes” the TLDs, allowing them to be reused for more dose measurements.

In order to translate a photon count from a TLD which has been exposed to an unknown dose to a measurement of absorbed dose, the TLD is usually exposed to a previously calibrated source. Then, the response of the TLD to a known absorbed dose is compared to its response to the unknown dose. This is in contrast to Fricke dosimetry, where an absorption measurement can be directly converted into a dose measurement.

CHAPTER 3

Radiation Effects

This chapter discusses the basic mechanisms of radiation damage on CMOS electronics, concentrating on the effects of total ionizing dose. The alleviation of radiation damage through high-temperature annealing is also discussed. Finally, the results of other radiation tests on FPGAs are presented.

3.1 Effects of Radiation on Electronics

Radiation damage of electronic devices can be divided into two main categories: damage from ionizing radiation and single event effects (SEE) from a single energetic particle (such as a proton, neutron, or heavy ion.) SEE can result in transient upsets in memory elements and logic circuits (referred to as single event upsets, or SEU). SEE can also cause latchup in complementary metal-oxide semiconductor (CMOS) circuits. This single event latchup (SEL) is not a transient effect, and can cause structural damage to the device if allowed to persist.

This thesis concentrates on the damage to a CMOS device due to total ionizing dose (TID). Ionizing radiation will affect CMOS devices by slowly changing the electrical parameters such as current and threshold voltages of the device. This section will discuss TID damage on MOS devices in detail.

3.1.1 Effects of Ionization

Photons, such as gamma rays and X-rays, interact with matter in three different ways – the photoelectric effect, the Compton effect, and pair production. All three of these photon interactions are ionization-causing processes, where free electrons, and thus hole-electron pairs, are produced. These electrons can themselves ionize atoms, making more hole-electron pairs. Ionization causes changes in material in three main ways: increasing conductivity, causing trapped charges in insulators, and breaking chemical bonds. For gamma radiation acting on electronics, chemical effects are not very significant.

Free electrons released from an ionized atom, if they have enough energy,

are released from the valence band, and reach the conduction band, creating hole-electron pairs. The energy difference, over that used to span the band gap, is lost in creating more electron-hole pairs or as thermal energy. For a particular material, the number of hole-electron pairs produced for every rad of ionizing dose absorbed is constant, and temperature independent.

The holes produced by ionization in an insulator are not very mobile. However, the electrons are comparatively mobile, and some electrons from hole-electron pairs will leak from the surface of the material to another material. This gives the material a net positive surface charge. If those electrons are captured by contiguous material, the contiguous material develops a net negative charge on its surface.

The trapped charges resulting from ionization can set up an electric potential, and thus an electric field, with the neutralizing charge counterparts on nearby conductors. As the electric field gets stronger, the conductivity of the insulator increases. However, if it does not increase enough to allow enough counter current to the insulator surface to establish an equilibrium current flow, electrical breakdown occurs, and the charge returns to the surface. In insulators, trapped charge can persist for days. The properties of the material can change from having charges trapped within it, even if the insulator as a whole remains neutral.

3.1.2 MOS and CMOS Structures

Figure 3.1 shows a cross-sectional view of a simplified n-channel Metal Oxide Field-Effect Transistor (MOSFET). The metal terminals of the transistor are at the gate, the source, the drain, and the substrate. A semiconductor material (such as silicon) makes up the bulk of the source, drain, substrate, and channel. The channel is the portion of the semiconductor which carries current between the source and the

drain. The channel and the gate are separated by a layer of oxide (SiO_2). In an n-channel device, the current is conducted from the highly-doped n-type (usually denoted n^+) semiconductor material at the source to the n^+ drain by electrons through the n-type channel, while the substrate is p-type. The opposite holds for p-channel devices, with holes conducting current between the p^+ source and drain.

The current flowing between source and drain depends on the voltage applied at the gate. If no current flows between the source and the drain when V_G , the voltage applied between the gate and the substrate, is 0, the transistor is called an enhancement mode device. N-channel MOSFETS can also be manufactured in depletion mode, where current does flow through the channel with zero gate voltage, and a negative V_G is required to turn it off. This is done by doping the channel region with n-type material beforehand.

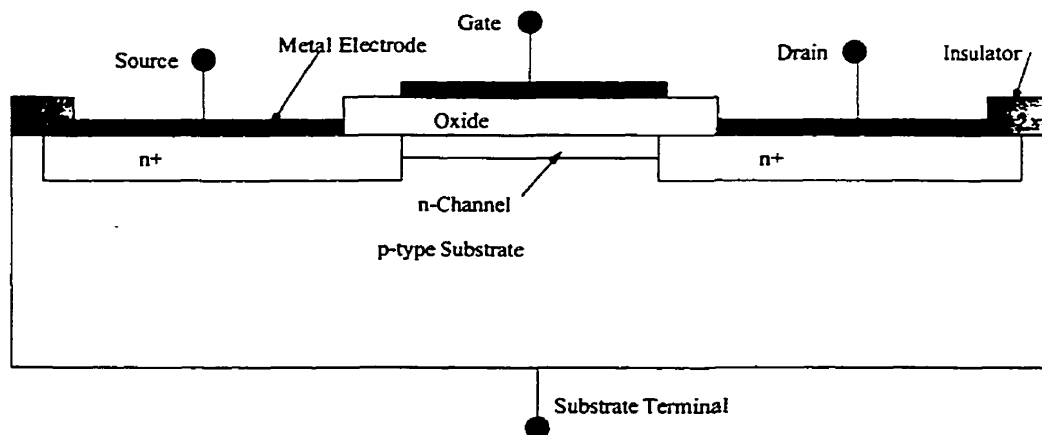


Figure 3.1: Cross-sectional view of an n-channel MOSFET

The key element in the MOSFET is the capacitor formed by the gate terminal, the substrate terminal, the channel, and the oxide layer. The properties of the MOSFET depend upon the voltage, V_G , applied to the gate terminal. If an MOS transistor is considered to be “ideal”, it is in thermal equilibrium with a constant Fermi level in the gate metal, oxide, and substrate if no voltage is applied. This is

called the flatband condition.

In the case of a p-type substrate (as would be found in an n-channel MOSFET), the application of a negative V_G attracts holes to the oxide-substrate interface, thus causing the accumulation condition. A small positive V_G results in the depletion condition, where the holes are depleted from a region in the oxide-substrate interface. As V_G increases, the depth of the depletion region also increases.

When the transistor is in depletion, electrons (the minority carriers) are also attracted to the interface. As the voltage increases, the concentration of electrons at the interface increases. Once V_G is high enough that the electron concentration at the interface is equal to or greater than the hole concentration in the bulk of the substrate, inversion occurs. The gate voltage where this begins is called V_i , the inversion voltage, or V_T , the threshold voltage.

In the case of an MOSFET with an n-type substrate, flatband still occurs with zero gate voltage, accumulation for positive voltages, depletion for small negative voltages, and inversion when V_G is equal to some negative value of V_i .

Once inversion occurs, the source-drain current I_D is controlled by the voltage applied at the drain, V_D . For small V_D , the channel behaves like a resistor, and I_D is proportional to V_D . As V_D increases, the channel becomes narrower in the area close to the drain. This decreases the conductance (dI_D/dV_D) of the channel. For a large enough V_D , the channel dwindles to nothing near the drain. This is called “pinch-off”, and the drain voltage where this occurs is sometimes called the “pinch-off voltage”, $V_{D_{sat}}$ or V_P . Once pinch-off is reached, (dI_D/dV_D) decreases to zero.

Complementary MOS (CMOS) structures combine a p- and n-channel enhancement mode transistor pair on the same substrate, and are often used in high-speed designs. The FPGAs tested in these experiments were CMOS devices. CMOS

devices can be operated with a single power supply, and have low standby power dissipation, high-speed operation, and high noise immunity. As well, CMOS Large-Scale Integrated Circuits (LSIs) have a very small die area per unit cell, very low power consumption, and a low density of defects during manufacture [19].

The simplest CMOS structure is the CMOS inverter, shown in figure 3.2. This particular inverter is built on a substrate of p-type material, with a n-type well acting as a substrate for the p-channel transistor. The inverter could also be constructed with a p-type well. Just as with stand-alone MOS devices, the p-channel transistor has a negative V_T , while the n-channel transistor has a positive V_T . In the CMOS inverter, the voltage V_I applied across the gates of both transistors is the same. Thus, a high V_I turns the n-channel device's channel on, and a low V_I turns the p-channel on.

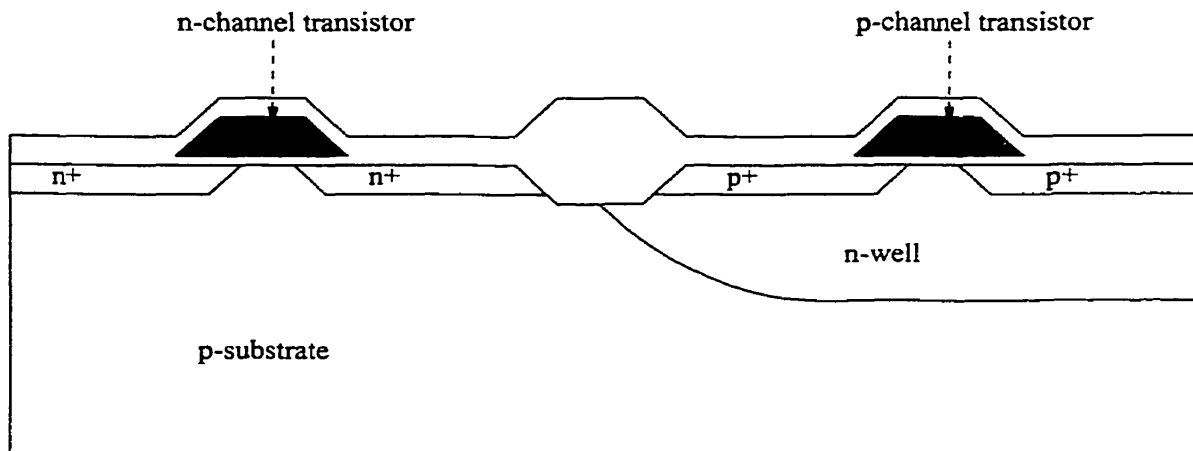


Figure 3.2: Cross-sectional schematic of an n-well CMOS inverter, modeled after reference [20]

A V_{DD} is also applied to the drain terminal of the p-channel transistor, and its source is connected to the drain terminal of the n-channel transistor. The n-channel's source is then connected to ground. When the input voltage is high, turning the n-channel on, V_{DD} drops mostly across the p-channel, and the output

voltage V_O is low. Similarly, when V_I is low (turning the n-channel off but the p-channel on), V_{DD} drops mostly across the n-channel, and V_O is high. This is why CMOS circuits have low power dissipation – at least one of the transistors is turned off, so there is no path which will carry significant current across the channels of the transistors.

3.1.3 Effects of Radiation on MOS and CMOS Structures

Ionizing radiation damages MOS devices primarily through building up positive charge (holes) in the oxide layers of the transistors, and trapping negative charges (electrons) at the interface. Although some of these pairs will recombine, the applied gate voltage sweeps the mobile electrons out of the gate oxide. The less mobile holes become trapped in the SiO_2 (for positive gate voltages) where they contribute to a trapped positive oxide charge. They may also be trapped at the silicon-oxide interface (for negative gate voltages) where they act to trap electrons. As the dose absorbed by the device increases, more hole-electron pairs are produced to become trapped oxide charge or interface traps. Since the number of hole-electron pairs produced is proportional to the amount of energy deposited in the device by the radiation, the total damage is roughly proportional to the dose absorbed by the device (since dose absorbed in a material is energy deposited per unit mass of the material). MOS devices have a wide range of radiation tolerance, ranging from 1 krad(Si) up to 10^7 krad(Si) before the first sign of damage [19].

Figure 3.3 shows the changes in the I_D vs. V_G curves of two example MOSFETs due to ionizing radiation. The primary effect of irradiating a MOSFET is the change in the V_T of the transistor. Since the current I_D in an n-channel enhancement mode device changes with the threshold voltage according to the equations

$$I_D = \frac{W}{L} \bar{\mu}_n C_{ox} \left[(V_G - V_T) V_D - \frac{V_D^2}{2} \right] \quad (3.1)$$

(for $0 \leq V_D \leq V_{D_{sat}}$ and $V_G \geq V_T$) and

$$I_D = \frac{W}{L} \bar{\mu}_n C_{ox} (V_G - V_T)^2 \quad (3.2)$$

(for $V_D \geq V_{D_{sat}}$ and $V_G \geq V_T$) the drain current also deviates from the ideal [20]. In the above equations, W and L are the width and length of the channel, $\bar{\mu}_n$ is the effective mobility of the carriers in the channel, and C_{ox} is the capacitance of the capacitor formed by the gate, substrate, and oxide layer.

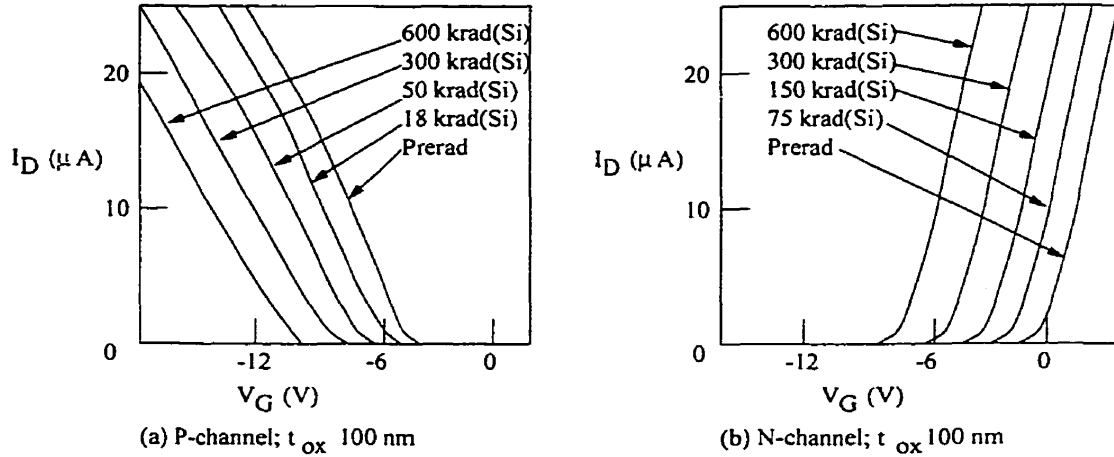


Figure 3.3: Radiation-induced shifts in enhancement MOSFET I_D - V_G curves, modeled after reference [19]

Radiation-induced shifts in V_T vary roughly with the cube of the oxide thickness [19]. Thus, the thinner the gate oxide in the device is, the more resistant it is to radiation. As electrons tunnel into the gate oxide from the contiguous structures, they recombine with the holes. If the oxide is thin, this recombination is more complete, because more electrons tunnel in. Other factors which affect the response of

a particular device include the material of the gate insulator, the processing and doping methods used to secure the gate insulator to the silicon, and the geometry of the device. The response of a device may also change with changes in the gate bias during irradiation (which affects both the location of trapped oxide charge and recombination at interface traps), temperature during irradiation, and dose rate.

Ionizing radiation affects the current-voltage characteristic curves of both the p- and n-channel parts of a CMOS structure. As the device is irradiated, the V_T for the n-channel transistor drops to negative values, as shown in figure 3.3. Meanwhile, the negative V_T for the p-channel device is also dropping. If a CMOS inverter were produced by linking the two example transistors described in figure 3.3, a V_I of -6 V would turn the n-channel transistor off, and the p-channel transistor on before irradiation. However, after about 50 krad(Si), the same input voltage would turn both devices off. After approximately 600 krad(Si), the n-channel would be on, but the p-channel would be off.

One other major problem with CMOS circuits is latchup, where a low resistance path between the power supply and ground is formed. These paths can be formed by the parasitic bipolar transistors which are built into the CMOS structure, one p-n-p and one n-p-n, if the gains of these transistors are large enough that they are driven into saturation. Under normal operation, this should not occur. However, ionizing radiation can induce latchup in a CMOS circuit by increasing the concentration of charge carriers, and thus the conductivity, of the components of the transistors.

In integrated circuits using MOS or CMOS technology, radiation damage can result in the device functioning improperly. One of the most significant effects of radiation damage in MOS structures is an increase in leakage current. Leakage

current is current flowing through a transistor which should be biased off, or current flowing between adjacent transistors. Low-resistance paths which allow leakage currents can be formed by the increase in density of interface traps, or by shifts in a transistor's V_T caused by trapped oxide charges.

In linear CMOS devices, leakage currents impair the high-input impedance which MOSFETs usually have. In an MOS transistor which is normally biased off at $V_G = 0$, drain to source leakage currents are less than 1 pA before irradiation, but increase to about 1 nA at 100 krad(Si), and hundreds of nanoamperes after 300 krad(Si), even though V_T in this example is still positive at 300 krad(Si) [20]. For complex integrated circuits, this can lead to significant increases in the power supply current. In the studies of total dose effects on the Xilinx FPGAs, the first sign of damage noted was an increase in power supply current due to the onset of leakage currents.

As the individual transistors making up a complicated CMOS integrated circuit such as a microprocessor or FPGA are damaged by ionizing radiation, the characteristics of the overall circuit will change. The damage to individual transistors and CMOS inverters can result in such effects as increased power supply current (due to leakage currents or transistors which should be off turning on), logic failures, latchup effects, or changes in circuit timing. The response to radiation of an integrated circuit made up of thousands of logic gates is, however, difficult to predict without extensive simulations.

3.2 Annealing Effects

Once the irradiation of an electronic device ends, its characteristics may still change substantially due to post-irradiation effects. The threshold voltages of n-channel or p-channel MOS transistors, which are shifted in the negative direction under irradiation, will start to shift in the positive direction, in some cases increasing their V_T above their original value [20]. The increase of V_T above the pre-irradiation value is referred to as “hyper-recovery”.

These effects are seen when transistors are left to anneal at room temperatures. Changes in threshold voltages with annealing time increase significantly at higher temperatures [20]. Just as the negative shift in V_T is due to trapped holes in the oxide or at the interface traps, the annealing effect is due to electrons tunneling from the silicon to the oxide and canceling out the charge of the trapped holes. The rate of this process increases at high temperatures.

Since MOS or CMOS devices can anneal radiation damage at room temperature, they might be able to anneal some of the damage due to absorbed dose while they were still under irradiation. This means that a device irradiated at a lower dose rate could show less damage than an identical device which had absorbed the same total dose at a higher dose rate. On the other hand, low dose rate may allow some devices to hyper-recover, thus becoming even more damaged than they would have been at higher dose rates. Hence, ionizing radiation testing of electronics often includes a period of annealing at high temperatures in order to simulate the effects of a lower dose rate.

The standards in use by the European Space Agency [21] and the US military [22] for total ionizing dose tests of electronics call for an accelerated annealing

test of $(100 \pm 5)^\circ\text{C}$ for (168 ± 12) hours, with the device under bias. However, in our tests of FPGAs, these standards could not be followed exactly.

The junction temperature, T_j , for the FPGAs tested is given by

$$T_j = T_A + (15^\circ\text{C}/\text{W})VI, \quad (3.3)$$

where V is the power supply voltage to the FPGA (3.3 V in our case), T_A the ambient temperature, and I the power supply current [4]. The high-quality parts used by space and military agencies can withstand higher junction temperatures than the less expensive commercial parts we used. The junction temperature had to be kept below 125°C to avoid damage to the FPGA. Thus, annealing the FPGA at 100°C would require that the current be kept below 0.50 A. When the test procedure was designed, the risk that the peak current during annealing would be higher required a lower annealing temperature. In addition, the FPGA had to be placed in the oven along with the entire circuit board with several passive components. Heating the circuit board to 100°C could have resulted in damage to these passive components or to the solder joints. In order to avoid further damaging the FPGAs during annealing, the temperature used for annealing was lowered to 50°C . This lower temperature resulted in slower annealing, so the FPGA was kept in the oven twice as long as the standard (two weeks, or about 336 hours) to compensate.

3.3 Recent Radiation Tests of FPGAs

3.3.1 Total Ionizing Dose Tests

Most FPGA tests to date have been performed with a view towards their use in space environments. Most of these tests have been concerned with single event upsets (SEU) and single event latchups (SEL) caused by heavy ions. This is because the effects of heavy ions from cosmic rays or solar flares are the primary concern when determining the effects of radiation on electronics in Earth orbit.

Most of the FPGAs which have been tested are antifuse-based, and thus non-reprogrammable, FPGAs. Since antifuse based FPGAs are programmed via permanent interconnections, a logic upset due to total ionizing dose effects or single event effects will not cause the program to be lost. Although results of radiation tests of antifuse-based FPGAs can be compared to results from SRAM-based FPGAs, the two technologies are quite different. Thus, it is difficult to make assumptions about the radiation tolerance of SRAM-based FPGAs based on test results of antifuse-based devices.

The total ionizing dose resistance of Actel antifuse-based FPGAs varies from less than 3 krad(Si) (for the A1280XL and A32140DX devices [23]) to 300 krad(Si) or more (for the RH1020 [24] and the RH1280 [23], which are specifically designed to be radiation hard). A more complete listing of total dose tests on Actel FPGAs can be found in reference [25]. QuickLogic's QL3025, an antifuse-based FPGA in the high-speed pASIC 3 family, withstood about 35 krad(Si) [26] before failure. From the results of various total ionizing dose tests of antifuse FPGAs, it can be seen that the radiation tolerance varies greatly between different production lots of the same device. Newer devices also tend to have lower radiation resistance [25].

In an SRAM-based FPGA, a disruption in the memory store of the FPGA can cause the circuit configuration to be lost, requiring the circuit to be downloaded again. This is a significant problem for applications which require that the circuit to configure an SRAM-based FPGA be stored in a memory device which is also subject to upset in a radiation environment. However, the circuit for the SCA controller in a hypothetical FPGA implementation would have been downloaded from an external serial port [8]. Thus, the original configuration could be reloaded from a source not subject to radiation damage.

While Actel's RH1280 and RH1020 are radiation-tolerant, they are not as versatile as a radiation-hardened reprogrammable FPGA, since they can only be programmed once. Thus, in addition to their work on radiation-hardened antifuse-based FPGAs, the Actel corporation has tested a prototype of an SRAM-based FPGA for space applications. This FPGA, the RS series, was fabricated using a 0.25 μm process (compared to the 0.35 μm process used for the Xilinx XC4036XL and XC4036XLA FPGAs.) The prototype has shown radiation hardness to 50 krad(Si) [27].

Xilinx has also designed a series of FPGAs specifically for radiation environments. The Xilinx XQR4036XL, a 0.35 μm device, has absorbed a total dose of 60 krad(Si) [28]. Most of the testing of this technology, however, has dealt with single event effects, as the vulnerability of SRAM-based FPGAs to single event effects has been the main reason SRAM-based FPGAs have not often been used in radiation environments. It must be noted, however, that the radiation-hardened XQR4000 series FPGAs are not as fast as the XC4000XL or XC400XLA series.

The newer Virtex family of Xilinx FPGAs is faster and has a greater gate capacity than the XC4000XL or XQR4000XL series. A radiation-hardened version of this series, the XQVR300 FPGA, has also been produced, but is not yet generally

available. This device is fabricated with a 0.22 μm process. Reference [29] says that Xilinx test data indicated this FPGA will resist over 50 krad(Si), but the full results of these tests have not been published.

Other technologies are being considered for the production of radiation hardened FPGAs. FPGA Technologies is designing an EEPROM-based FPGA for space applications. It is expected to withstand a total ionizing dose above 200 krad(Si) [5]. A similar SRAM-based device is also being designed, which is expected to withstand 100 krad(Si) [5]. Actel and Gatefield are also co-producing a FLASH-memory based FPGA, the ProASIC 500K family. Tests have shown this device to withstand total ionizing dose above 50 krad(Si) [6].

3.3.2 Single Event Tests of SRAM-based Field Programmable Gate Arrays

In single event testing of electronics, the devices under test are subjected to a beam of protons, neutrons, or heavy ions. Heavy ion beams are characterized by their linear energy transfer (LET), or the energy locally deposited by the particle per unit path length [12]. LET is usually measured in MeVcm^2/mg , and needs to be multiplied by the density of the material being irradiated to determine the energy deposited. This ensures that a given beam of particles can be characterized independent of what it irradiates.

The single-event effects tolerance of electronic devices is characterized by finding the cross-sections of SEU for a range of LET, and by finding the LET_{th} where the device begins SEU or SEL. Proton and neutron tests, however, are reported by expressing the total cross-sections of SEU as a function of particle energy. The cross-sections of SEU are expressed in terms of logic upsets times area of die per bit

or per device.

The earliest tests of SRAM-based FPGAs for single event effects were not promising. Crosspoint CP20420 FPGAs undergoing heavy ion tests showed SEU at an LET of 11.3 MeVcm²/mg, and SEL between 15 and 26.6 MeVcm²/mg [30]. Testing of a Xilinx 3090A FPGA showed that it was subject to SEL at 7.9 MeVcm²/mg [31]. Reconfiguration errors began to occur between 4.1 and 7.9 MeVcm²/mg, and data errors began to occur between 9.6 and 11.4 MeVcm²/mg. Both devices were produced with 0.8 μ m CMOS processes.

By comparison, the antifuse-based FPGAs available at the time, such as the A1020 and A1280 series, did not show SEL effects even at fairly high LETs. The only cases of SEL reported in Actel antifuse based FPGAs occurred in tests of the A1020B (which latched up at LET_{th}s of 22 to 37 MeVcm²/mg [23]) and the A32200DX which showed an LET_{th} for latchup of 11 to 16 MeVcm²/mg [23]. (The A32200DX is a device from the same family as the A32140DX, which did not latch up [23].)

Despite this, SRAM-based FPGAs still offered higher gate capacity and speed than antifuse based FPGAs. Hence, there was still some interest in testing SRAM-based FPGAs in a radiation environment. In reference [32], Xilinx XC4010E and FPGAs were irradiated with 0-11, 14, and 100 MeV neutrons. XC4010XL FPGAs were also irradiated with 100 MeV neutrons. The XC4010E was produced using a 0.60 μ m process, while the XC4010XL was produced using the same 0.35 μ m process as the XC4036XL. Neutron irradiation produced little or no SEUs in the XC4010E devices at the lower energies. At 100 MeV, the SEU cross sections were 1.3×10^{-15} cm²/bit for the XC4010E, and 4.4×10^{-15} cm²/bit for the XC4010XL. No latchup was reported, and reconfiguration of the devices after SEU allowed the

devices to continue working properly without signs of permanent damage.

In addition to the total ionizing dose tests discussed in this work, proton-induced single event upset tests on Xilinx XC4036XLA FPGAs were performed by our group [33]. Protons with energies varying from 23 to 94 MeV incident on the FPGA die were used. Upsets were observed at all proton energies, with the saturation cross-section at high energies determined to be $(3 \pm 1) \times 10^{-9}$ cm²/device. Proton testing of these FPGAs will continue.

The XQR4036XL devices referenced in the previous subsection are similar to the XC4000XL series, but are specifically modified to tolerate radiation. In addition to the total ionizing dose tests, SEE tests have been performed. Heavy ion tests with LETs up to 110 MeVcm²/mg resulted in no latchup [34]. SEU did occur, however, with cross-sections ranging from $\sim 1 \times 10^{-11}$ cm²/bit at 5 MeVcm²/mg to $\sim 1 \times 10^{-7}$ cm²/bit at 100 MeVcm²/mg [34].

The Virtex XQVR300 FPGA from Xilinx underwent heavy-ion testing, and was found to be immune to SEL up to an LET of 125 MeVcm²/mg [29]. This is the highest LET usually used in heavy ion testing to characterize a device's suitability for the space radiation environment. Thus, the XQR4036XL and XQVR300 FPGAs can be considered as immune to single-event latchup as antifuse based devices. The SEU cross-sections were comparable to those of the XQR4036XL.

CHAPTER 4

Radiation Testing

This chapter discusses the preparation for the radiation tests of the FPGAs. We begin by discussing tests which investigated the use of Fricke dosimetry to determine the dose rate from the cobalt-60 source. The setup and procedure of the radiation tests, the procedure used to determine the dose rate absorbed by the FPGA die, and the code used by the computer monitoring the FPGA during irradiation are also discussed.

4.1 Initial Tests of Dosimetry, Shielding, and Geometry

Before the radiation tests of the FPGAs, several tests were carried out to estimate the dose rate which the FPGAs would be exposed to and to test the use of Fricke dosimetry.

4.1.1 Testing of Fricke Dosimetry

The first test (previously described in reference [35]) was done to check the suitability of Fricke dosimetry for use with the cobalt-60 source. Figure 4.1 shows the setup of the first test. In the first test, three Fricke dosimeters were positioned on a circular arc, centered on the source. Each of the dosimeters was placed (42.4 ± 0.2) cm from the source, with a separation of about 30 cm from one another. Another dosimeter was positioned outside the radiation area, in order to provide a background measurement. The optical density of the background dosimeters was subtracted from the optical density of the irradiated dosimeters in order to find the dose absorbed, as in equation 2.8.

The dosimeters under irradiation were positioned at the height of the source with wooden stands. Over a 143 hour period, the optical density of the dosimeters was measured 12 times. The results are shown in figures 4.2, 4.3, and 4.4. Figure 4.2 shows the dosimeter on the left side of the source. Due to irregularities in the stands, the dosimeter placed to the left of the source was actually 0.8 cm closer to the source than the others. Accordingly, a 4% reduction to the dose, due to the inverse square law, was applied before plotting the data from the left dosimeter and comparing its results to the other dosimeters. The central dosimeter's results are

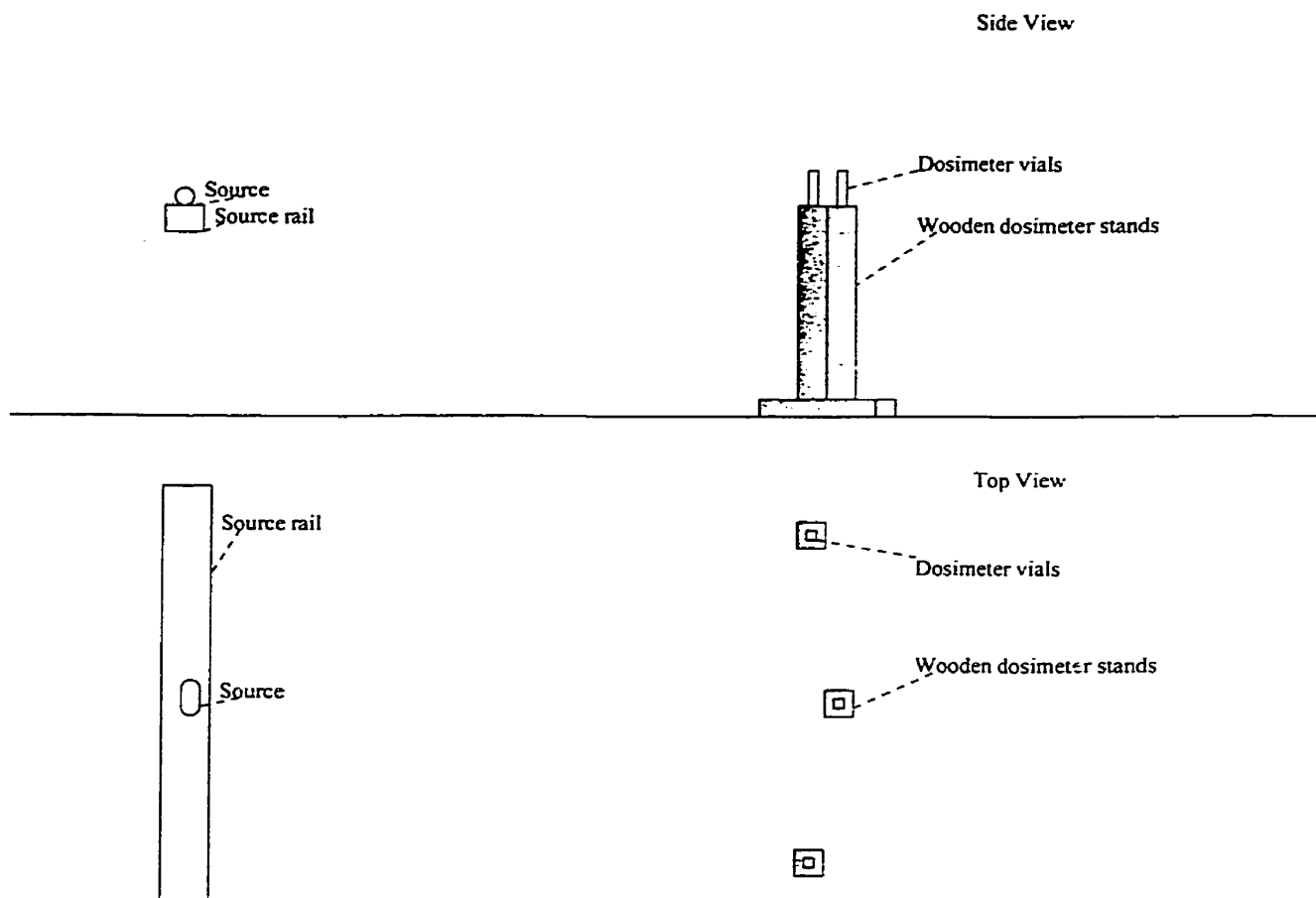


Figure 4.1: Setup of the first Fricke dosimetry test, not to scale.

plotted in figure 4.3, and the right dosimeter's results are plotted in figure 4.4.

For all three dosimeters exposed to the radiation, the dose rate was high enough that over the course of the experiment, the response of the dosimeters to absorbed dose was no longer linear. Thus, not all of the points on the plots were part of the linear fit – after absorbing more than 50 to 60 krad, we believe that the radiation had depleted the oxygen in the Fricke solution. In all subsequent dosimetry measurements, all points recorded after the saturation of the dosimeter were not included in the fits.

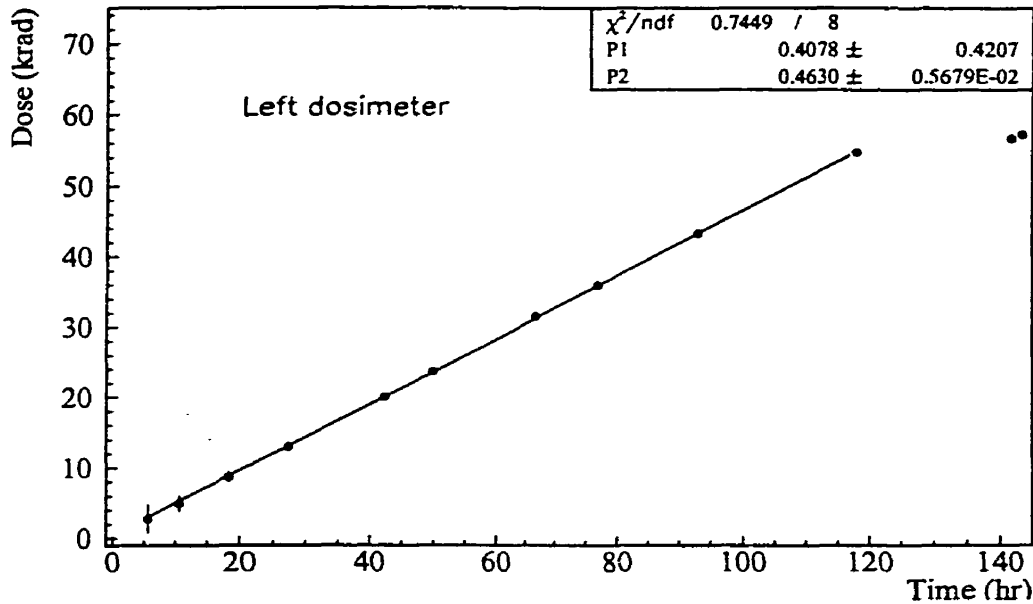


Figure 4.2: First Fricke dosimetry test: Reduced dose versus time measured in the left dosimeter.

The weighted average of the dose rates was calculated, assuming that the three absorbed dose rates were independent, and the standard deviation was used as an estimate of the statistical error. A systematic error was also estimated from the errors in the fit of the dosimetry plots. This resulted in a average dose rate of $(486 \pm 6 \pm 20)$ rad/hr at 42.4 cm from the source.

Once the dose rate is determined, the activity of the source can be estimated. First, we convert dose rate in rad/hr to exposure rate in roentgens (R) per hour. (1 R is defined as the production of 2.58×10^{-4} coulombs of ionization in a kilogram of material due to X-rays or gamma rays.) In reference [12], we find that 1 R of gamma radiation is equivalent to 0.867 rad in air, assuming an average energy to create an ion-electron pair of 33.7 eV. As the absorbed dose for different materials is different, the energy absorption coefficients in air and in Fricke solution (in reference [16]) for 1.25 MeV gamma rays must also be compared:

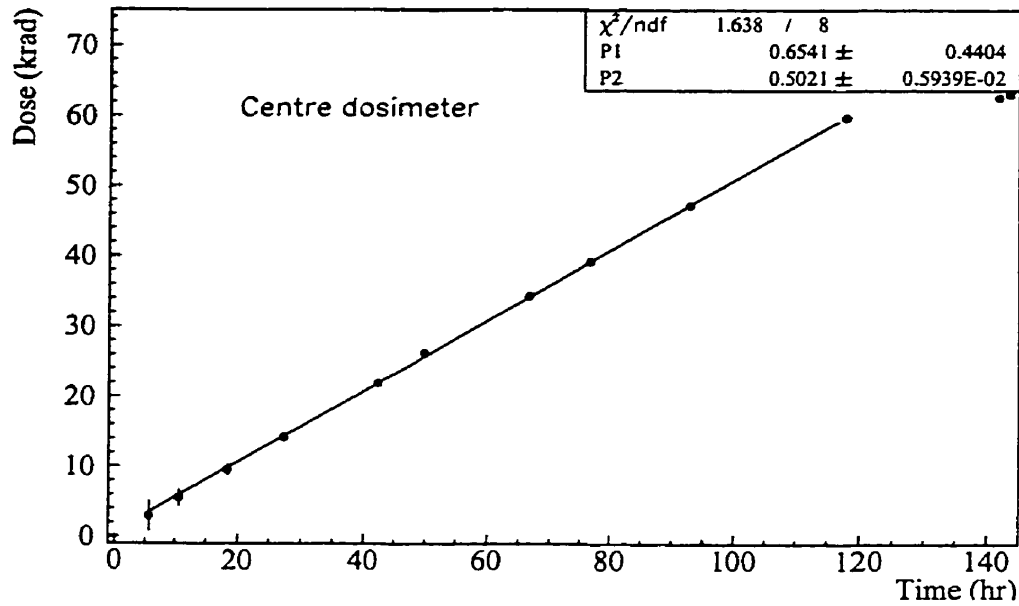


Figure 4.3: First Fricke dosimetry test: Dose versus time measured in the centre dosimeter.

$$\frac{(\mu_{en}/\rho)_{air}}{(\mu_{en}/\rho)_{Fricke}} = \frac{2.666 \times 10^{-2}}{2.955 \times 10^{-2}} = 0.902. \quad (4.1)$$

Thus, 1 R is equivalent to 0.961 rad in Fricke solution. Then, the equation from reference [18] can be used,

$$\dot{X} = \frac{\Gamma \alpha}{d^2} \quad (4.2)$$

where \dot{X} is exposure rate in R/hr, Γ is $13.2 \text{ R}\cdot\text{cm}^2/\text{hr}\cdot\text{mCi}$, d is the distance from the source, and α is the activity of the source. This results in an activity of 68.9 Ci.

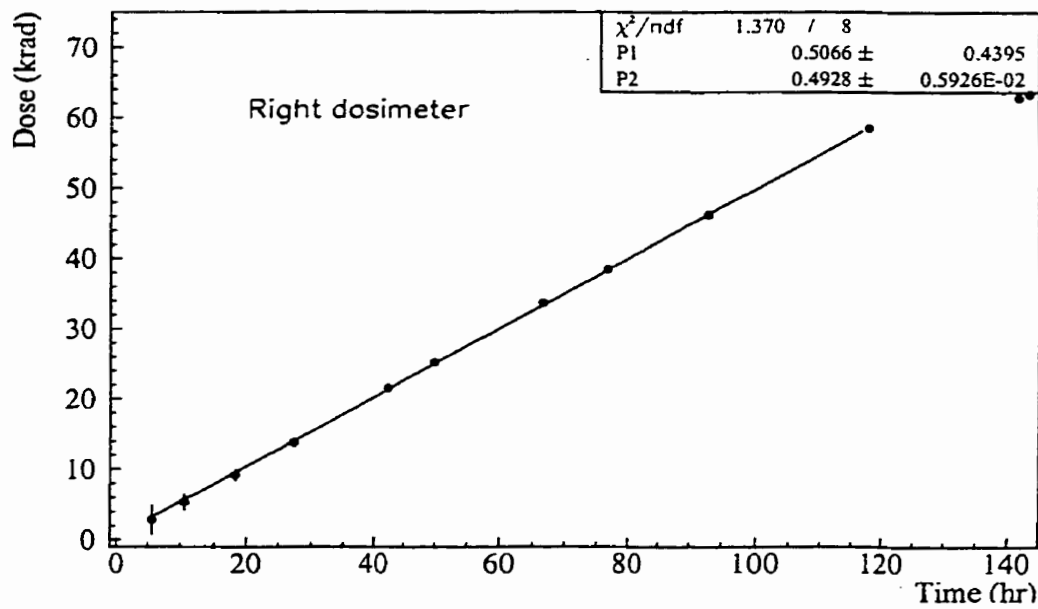


Figure 4.4: First Fricke dosimetry test: Dose versus time measured in the right dosimeter.

4.1.2 Dosimetry Test With Lead Wall

The next test (previously described in reference [36]) was primarily designed to measure the dose from a collimated source. In addition, it was designed to measure the backscattered radiation from a lead wall. The setup for this test is shown in figure 4.5. For this purpose, a lead wall 15 cm thick and 56 cm across was built, with a 3.6 x 2.0 cm aperture 24.3 cm from the source. This aperture was aligned with the source. The purpose of the lead wall was to provide a collimated beam of gamma rays from the source.

As in the previous test, a wooden stand was built to bring dosimeters up to the level of the source. Three dosimeters – at 24.9 cm, 29.3 cm, and 34.8 cm from the source, in line with the aperture – were used to measure the dose rate in front of the FPGA, at the FPGA's planned position, and behind the FPGA. Two additional dosimeters were not in line with the aperture, and were located 3.5 cm from the lead wall. These dosimeters, 20.7 cm to the left and 20.7 cm to the right of the source, were used to measure the backscattered radiation from the lead wall as well as the radiation remaining after attenuation by the lead. Two more dosimeters were used for background measurements inside the cave. One was placed out of the line of radiation, while another was placed far from the source and shielded by the lead wall.

It must also be noted that only the bottom 2.8 cm of the centre vials were irradiated by the source – partly because of imperfect alignment of the bottom of the vials with the bottom of the aperture, and partly because the vials themselves were filled to a higher level than necessary (3.9 cm for the closest dosimeter, and 3.7 cm for the other two.) The radiation dose rates were thus corrected based on the ratio of this height to the height of fluid in the dosimeter:

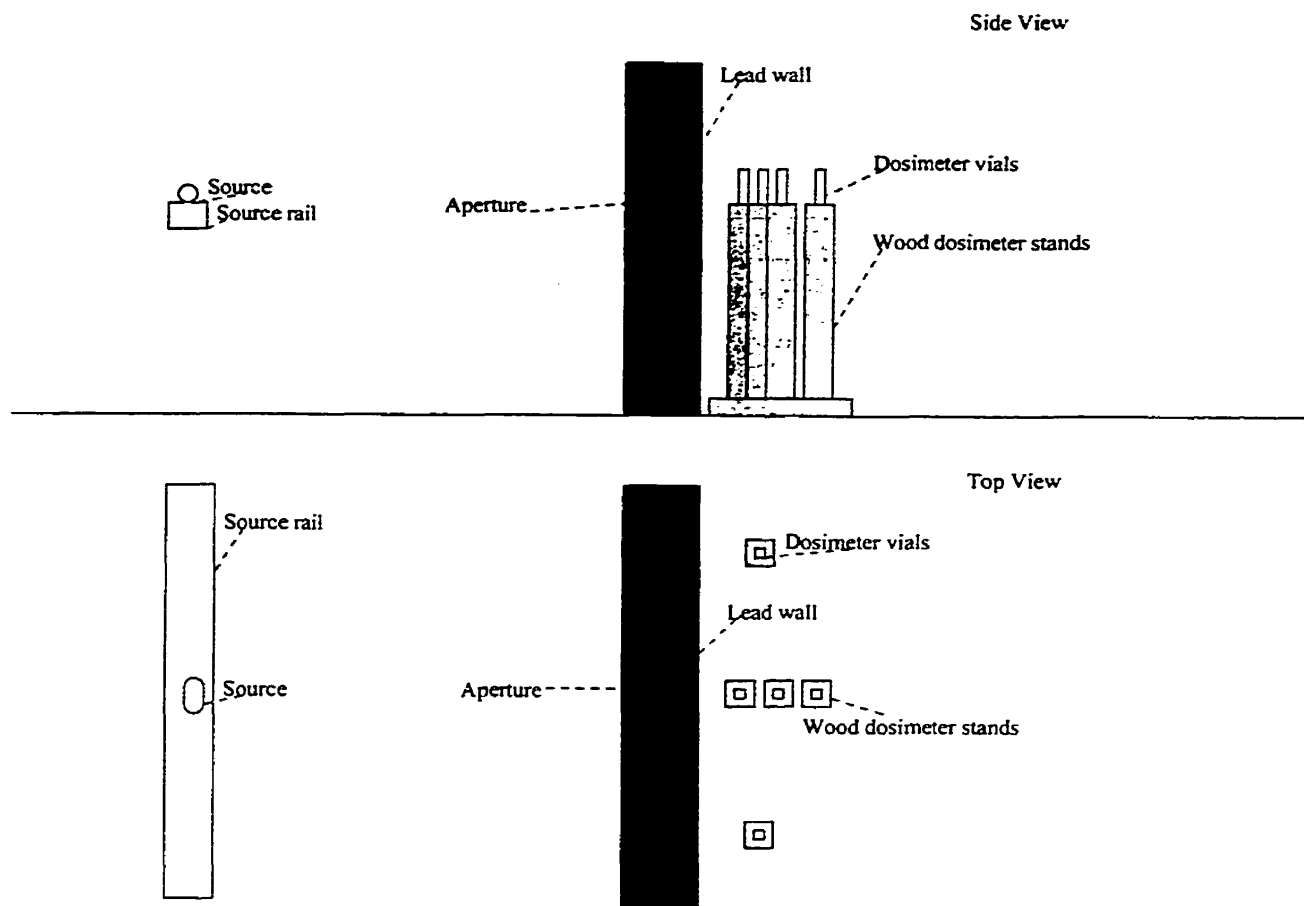


Figure 4.5: Setup of lead wall test, not to scale.

$$\frac{dD(\text{actual})}{dt} = \frac{\text{Height of fluid}}{2.8 \text{ cm}} \frac{dD(\text{apparent})}{dt} \quad (4.3)$$

The calculated dose for each of the three central dosimeters has already been corrected on figures 4.6 (for the far central dosimeter), 4.7 (for the mid-central dosimeter), and 4.8 (for the near central dosimeter.) Figures 4.9 and 4.10 show the dose versus time for the backscatter dosimeters. The dose versus time for the two background dosimeters in the cave are shown in figure 4.11 (for the dosimeter in line of radiation) and figure 4.12 (for the dosimeter further back in the cave). Finally, figure 4.13 shows the dose versus time for the background dosimeter.

Over a 281 hour period, 16 measurements of the optical densities of all eight dosimeters were made. For the two dosimeters measuring background in the cave, the total dose was less than the approximately 4 krad needed for accurate reading of the change in optical density, and the dose rate thus could not be accurately measured. Similar problems were found with the two dosimeters measuring the backscattered radiation. Thus, the dose rate from background and backscattered radiation is negligible.

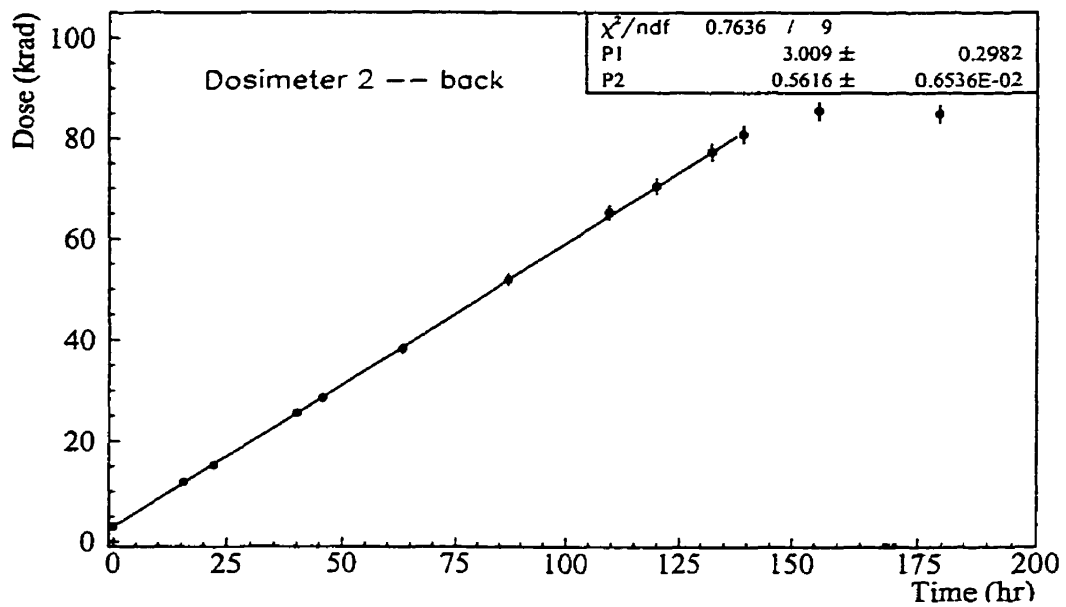


Figure 4.6: Lead wall test: Dose versus time measured in the far central dosimeter.

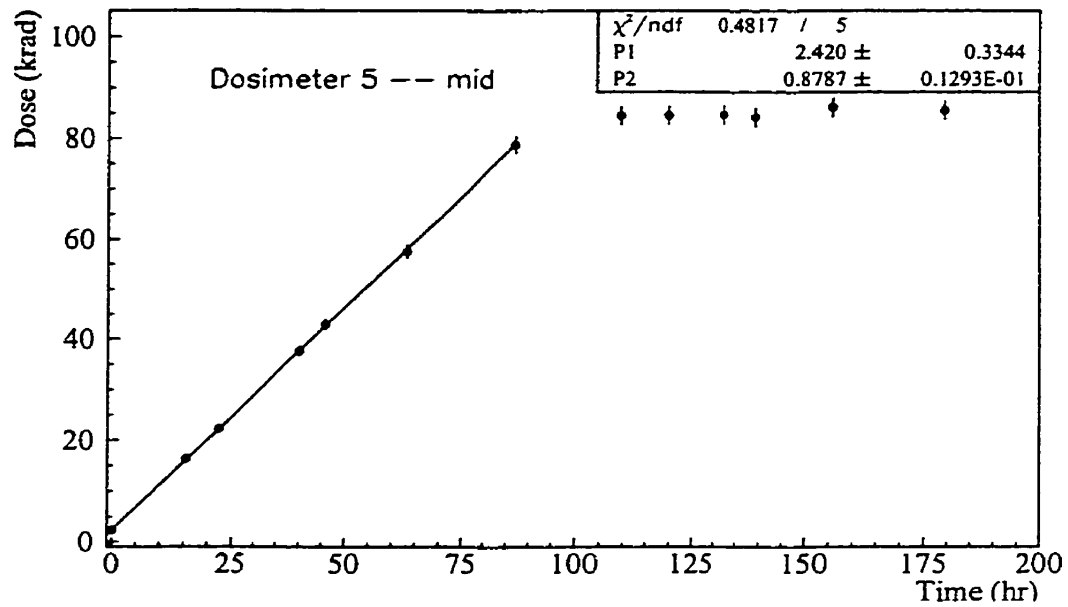


Figure 4.7: Lead wall test: Dose versus time measured in the mid-central dosimeter.

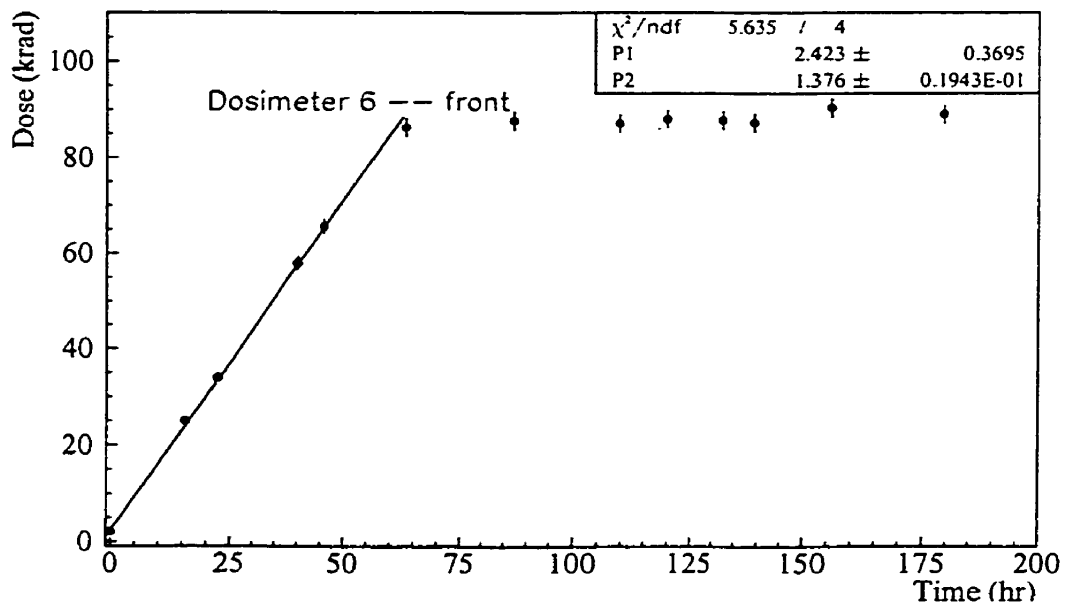


Figure 4.8: Lead wall test: Dose versus time measured in the near central dosimeter.

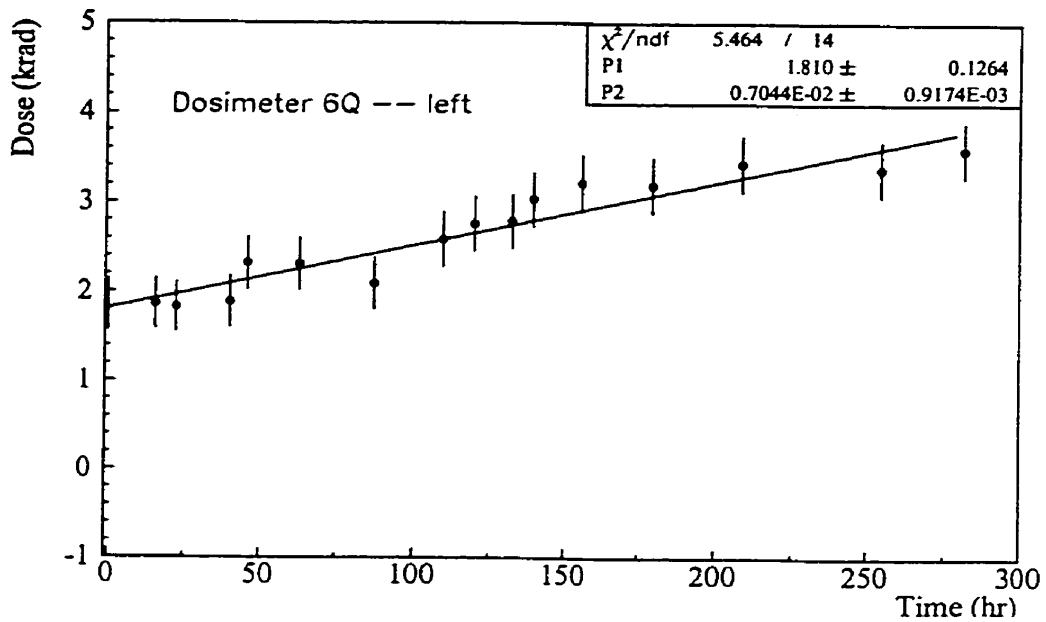


Figure 4.9: Lead wall test: Dose versus time measured in the left backscatter dosimeter.

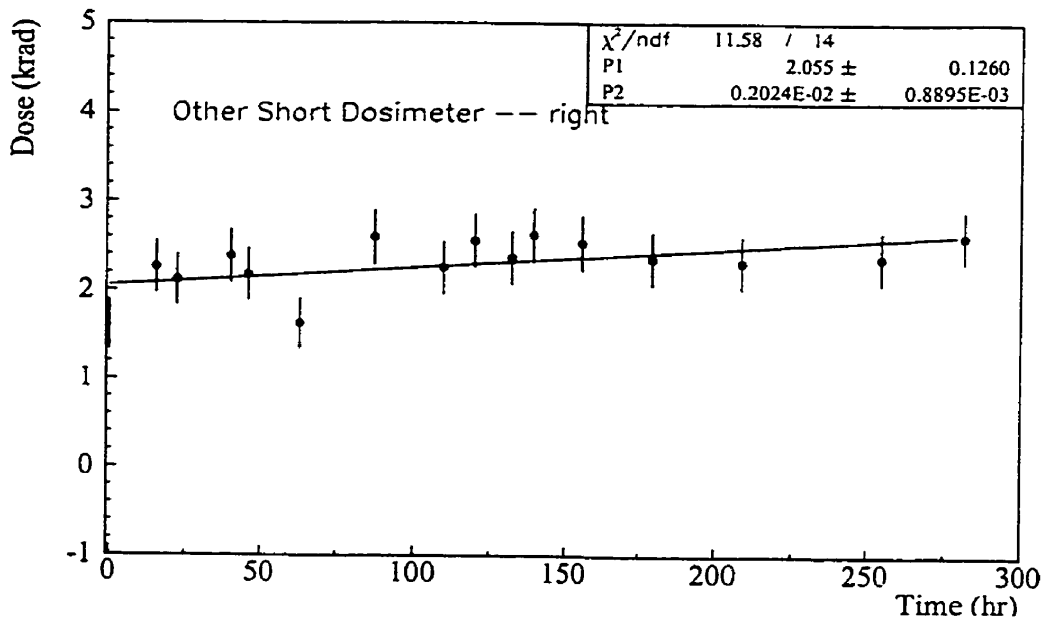


Figure 4.10: Lead wall test: Dose versus time measured in the right backscatter dosimeter.

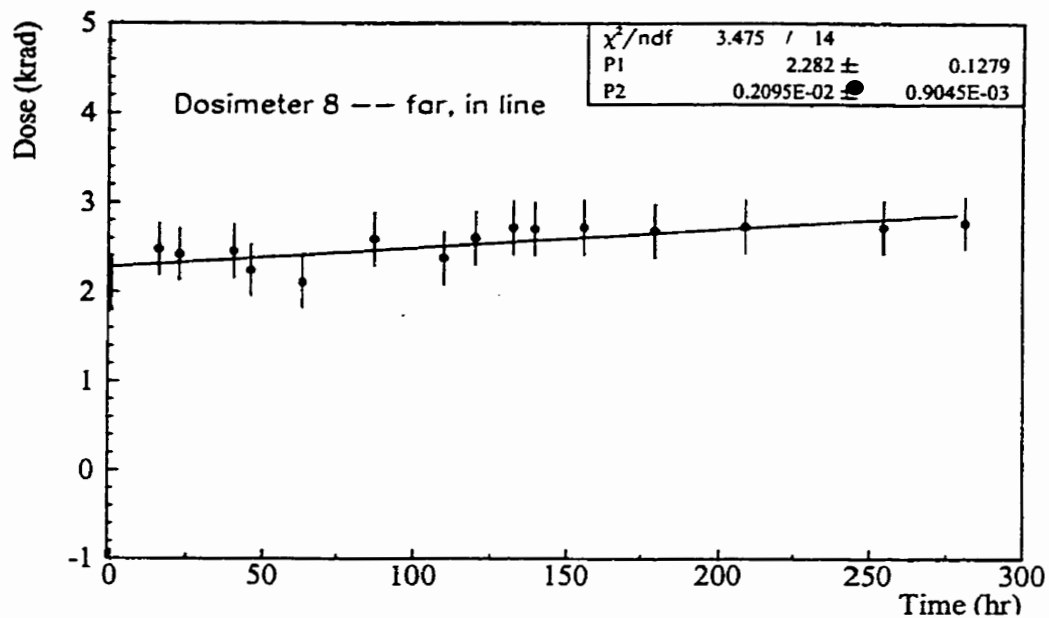


Figure 4.11: Lead wall test: Dose versus time measured in the background dosimeter in the line of radiation.

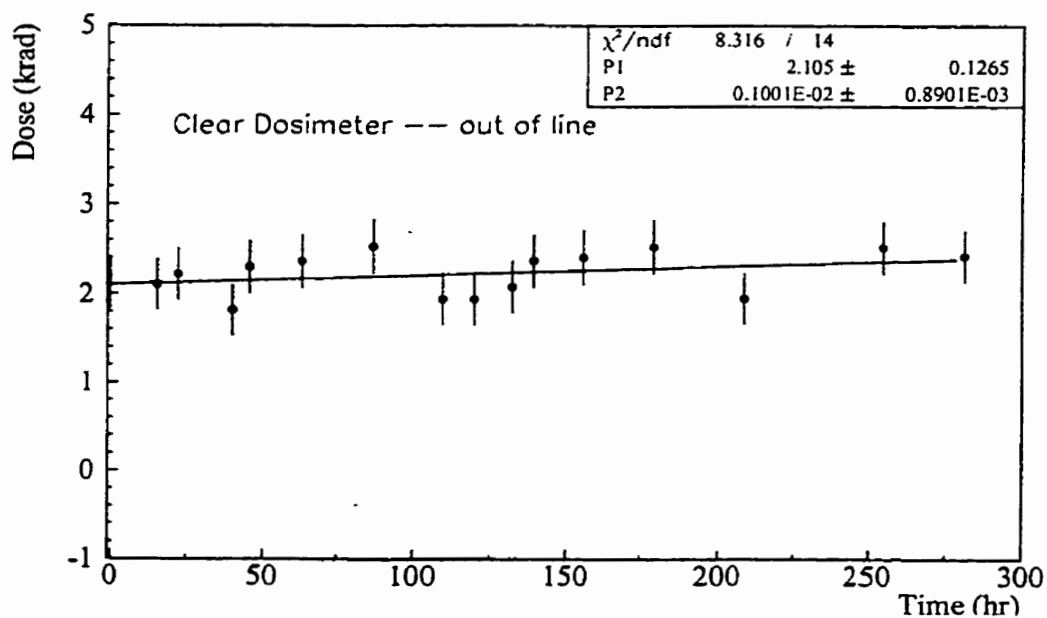


Figure 4.12: Lead wall test: Dose versus time measured in the background dosimeter out of the line of radiation.

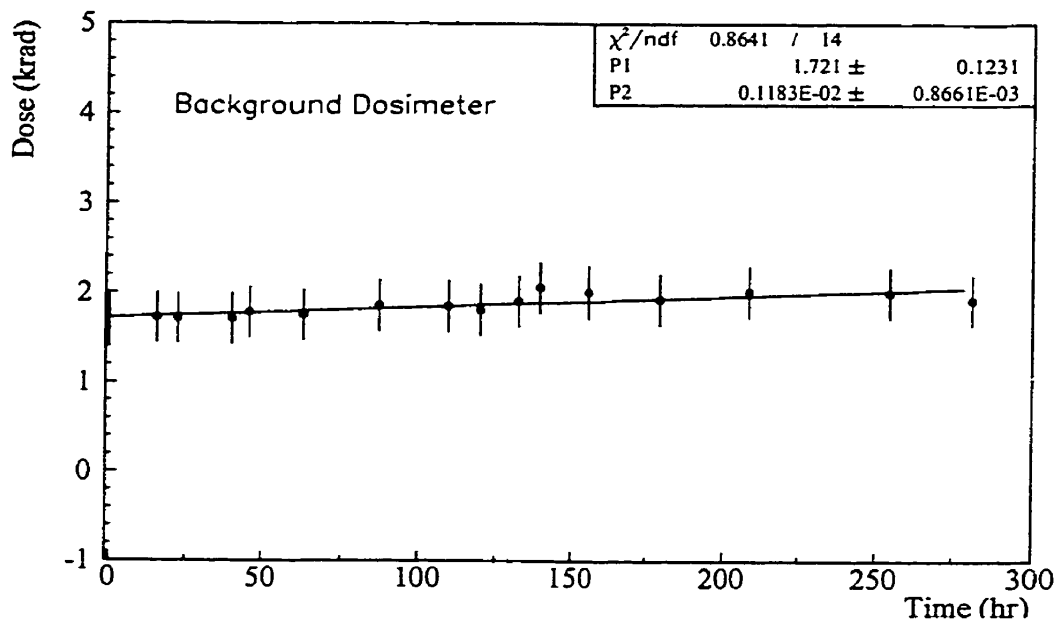


Figure 4.13: Lead wall test: Dose versus time measured in the background dosimeter outside the cave.

The dose rates measured for the dosimeters used in this test are given in Table 4.1. Note that the dose rates for all vials except for the background vial are the dose rates above background. The rates for the two background dosimeters in the cave were quite low, comparable to the background levels. The dosimeter measuring backscattered radiation on the right also measured a low rate, although the dosimeter measuring backscattered radiation on the left did show a significant dose rate. The average dose rate at dosimeter 5 is a weighted average of the dose rate at the mid-central dosimeter and the dose rates found by applying the expected attenuation to the dose rates in the front central and rear central dosimeters.

| Location | Number | Dose rate (rad/hr) |
|---------------------|------------|------------------------|
| Far, central | 2 | 559.3 ± 3.8 |
| Middle, central | 5 | 877.0 ± 7.3 |
| Near, central | 6 | 1316 ± 19 |
| Avg. dose rate at 5 | | $835 \pm 5_{-6}^{+73}$ |
| Left backscatter | 6Q | 4.00 ± 0.23 |
| Rt. backscatter | short | 0.27 ± 0.24 |
| Far, in line | 8 | 0.83 ± 0.23 |
| Far, out of line | 4-clear | -0.43 ± 0.25 |
| Background | unnumbered | 0.84 ± 0.19 |

Table 4.1: Dose rates measured for each dosimeter in lead wall test.

The dose rate in the central dosimeters will be decreased both by attenuation of the gammas while passing through the air, glass, and dosimeter solution, and reduction in intensity of the beam over distance (from the inverse square law.)

The attenuation formula used for the gammas traveling through a thickness of material was:

$$\frac{(dD/dt)_{final}}{(dD/dt)_{initial}} = e^{-\mu_{en}x}, \quad (4.4)$$

where x is the thickness of material, and μ_{en} is the energy absorption coefficient for the material.

The usual inverse square law was used to determine the reduction in dose rate with distance:

$$\frac{(dD/dt)_2}{(dD/dt)_1} = \left(\frac{d_1}{d_2}\right)^2, \quad (4.5)$$

where d_x is the distance from the source to dosimeter x , and dosimeter 2 is farther from the source than dosimeter 1.

Using the material densities and attenuation coefficients for 1.25 MeV gammas provided in reference [16], the expected attenuation was calculated and put into table 4.2. In table 4.2, (5-2) in the dosimeters column refers to the attenuation between the middle and far dosimeters, while (6-5) refers to the attenuation between the near and middle dosimeters. Error estimates were performed assuming 0.1 cm error in dosimeter distances, 0.05 cm error in the thicknesses of the dosimeter walls and solutions, and an error in reference [16]'s μ_{en}/ρ values of $1 \times 10^{-3} \text{cm}^2/\text{g}$. As the attenuation in air is so small, the attenuation in air will be neglected in the analysis of later tests.

The measured attenuation was, on average, 8.7% lower than the corresponding expected attenuation. Thus, the average dose rate is reported with a 8.7% asymmetric systematic error added in quadrature with the systematic error from uncertainty in the expected attenuation. The stat in addition to the statistical errors from statistical errors in the dose rates.

| Attenuation Source | Dosimeters | Factor | Uncertainty |
|-------------------------------------|------------|----------|--------------------|
| From Inverse Square Law | (5-2) | 0.709 | 0.006 |
| | (6-5) | 0.722 | 0.008 |
| Attenuation in air | (5-2) | 0.999894 | 5×10^{-6} |
| | (6-5) | 0.999857 | 6×10^{-6} |
| Attenuation in 2 mm glass (walls) | | 0.988 | 0.003 |
| Attenuation in 1 cm Fricke solution | | 0.970 | 0.002 |
| Total Expected Attenuation | (5-2) | 0.749 | 0.007 |
| | (6-5) | 0.693 | 0.008 |
| Total Measured Attenuation | (5-2) | 0.635 | 0.007 |
| | (6-5) | 0.634 | 0.011 |

Table 4.2: Attenuation factors for central dosimeters in lead wall test.

In summary, the collimated source provided a weighted average dose rate of $(835 \pm 5_{-6}^{+73})$ rad/hr at a distance of 29.3 cm. No significant backscatter was measured, although there appears to be a non-negligible dose rate in 6Q (the left dosimeter measuring backscattered radiation.)

4.1.3 Dosimetry Test With Full Enclosure

Another test (previously described in reference [37]) was done to check the absorbed dose rate in an aluminum box placed inside a full lead enclosure. A simplified diagram of the setup for the full enclosure test is shown in figure 4.14. The apparatus was set up just as in the subsequent FPGA tests, but without the FPGA, PC board, computer, or other electronics. The lead wall was expanded into an enclosure or “keep” constructed from lead bricks. As before, the lead enclosure served to produce a collimated beam. As well, since it was a full enclosure, it blocked background radiation. The walls of the keep were about 5 cm thick on the bottom of the enclosure, 10 cm thick on the right and left sides, and 15 cm thick in the front and

back sides. The entire enclosure measured 56 cm from left to right, 46 cm from front to back, and 55 cm from top to bottom. On top of the enclosure, an 8 mm thick slab of plexiglass was placed. This was used to support a layer of lead bricks 5 cm thick. The top bricks, as well as the plexiglass, were removed when dosimeters inside the keep had to be accessed.

A rectangular aluminum box was placed inside the enclosure, measuring 27.4 cm from left to right, 15.4 cm from front to back, and 20.8 cm in height, with a rectangular aperture 3.6 cm high by 2.0 cm wide. The box was placed on wooden blocks so its aperture and that of the enclosure were aligned. This aluminum box was used to block backscattered radiation (as discussed in section 2.2). It also had stands for two dosimeters which kept them in line with the aperture, and a rack which held a PC board in later tests of the FPGAs.

Seven dosimeters were used in this test. The first dosimeter was placed outside the cave, and was used for background measurements. As in the second test, two dosimeters were used to measure the background inside the cave. One was located in line of radiation but shielded by the lead enclosure and far from the source, and another was out of the line of radiation.

The four remaining dosimeters were used to measure the dose rate from the collimated source, the radiation attenuated by the shielding, and backscattered radiation within the enclosure. Two of them, one to the left and another to the right of the source, were placed on top of the aluminum box. These dosimeters were 7.1 cm back from the lead wall and 14.3 cm to the left or right of the centre of the aperture. Two dosimeters were placed inside the box — at 30.5 cm and 34.1 cm from the source, located in line with the aperture. These were intended to measure the dose in front of and behind the board's position in a test of the FPGA.

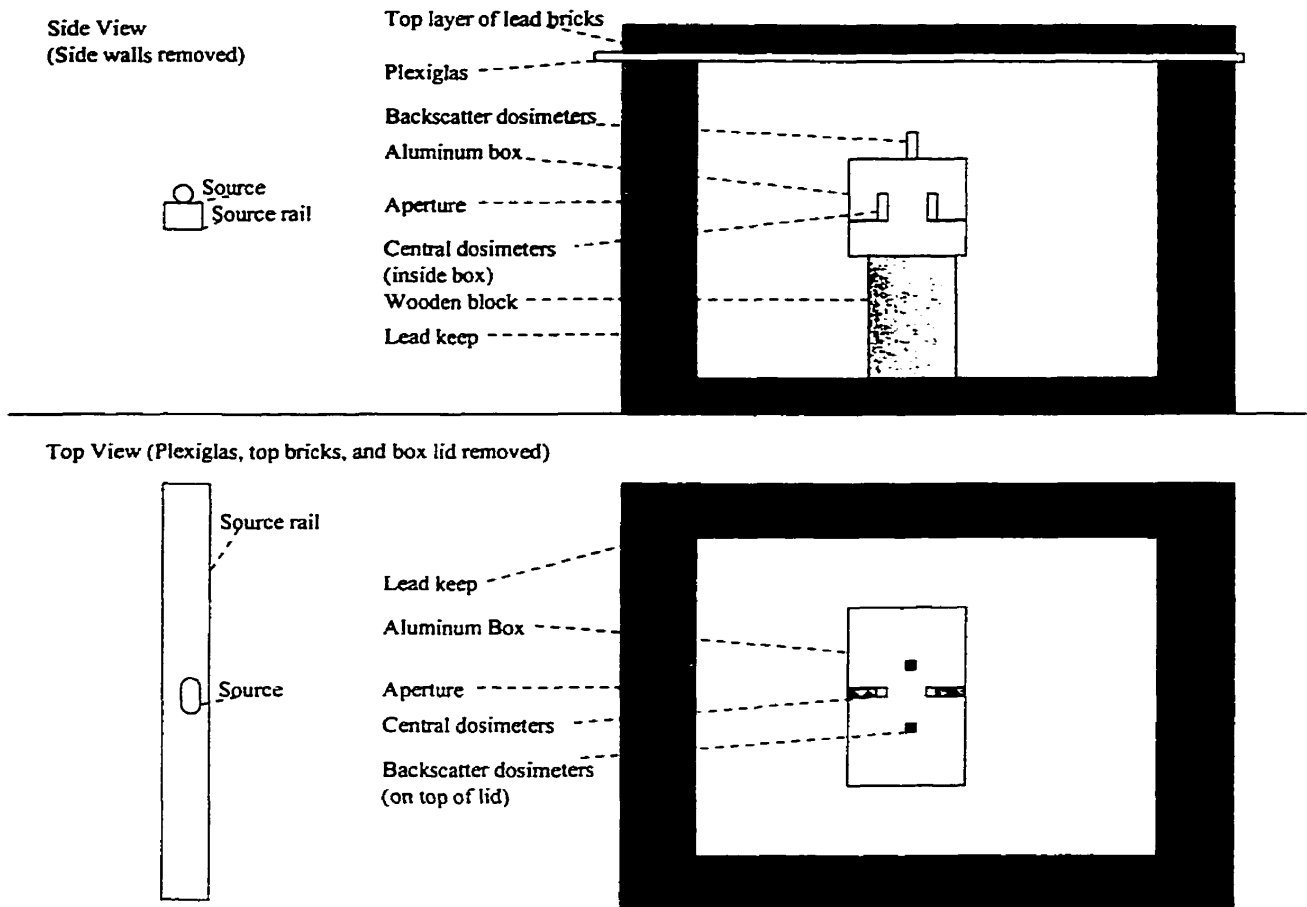


Figure 4.14: Setup of full enclosure test, not to scale.

Over a 423 hour period, measurements of the optical densities of the dosimeters were made. The two dosimeters inside the box were not measured after 162 hours, as they had reached saturation. Due to accidents occurring during the experiment, only 210 hours of irradiation were recorded for the dosimeter located at the near position outside the enclosure, and only 233 hours were recorded for the dosimeter located on top of the box on the left.

The results for the central dosimeters located in the box are shown in figures 4.15 (for the front dosimeter) and 4.16 (for the rear dosimeter). The results for the backscatter dosimeters placed on top of the aluminum box are shown in figures 4.17

and 4.18. Figure 4.19 shows the results for the dosimeter located in the cave and near the source, and figure 4.20 shows the results from the dosimeter located in the cave but far from the source. Again, for the two dosimeters measuring background in the cave, and for the two dosimeters measuring the backscattered radiation, the total dose was less than the approximately 4 krad needed for accurate readings. Finally, figure 4.21 shows the results from the background dosimeter outside the cave.

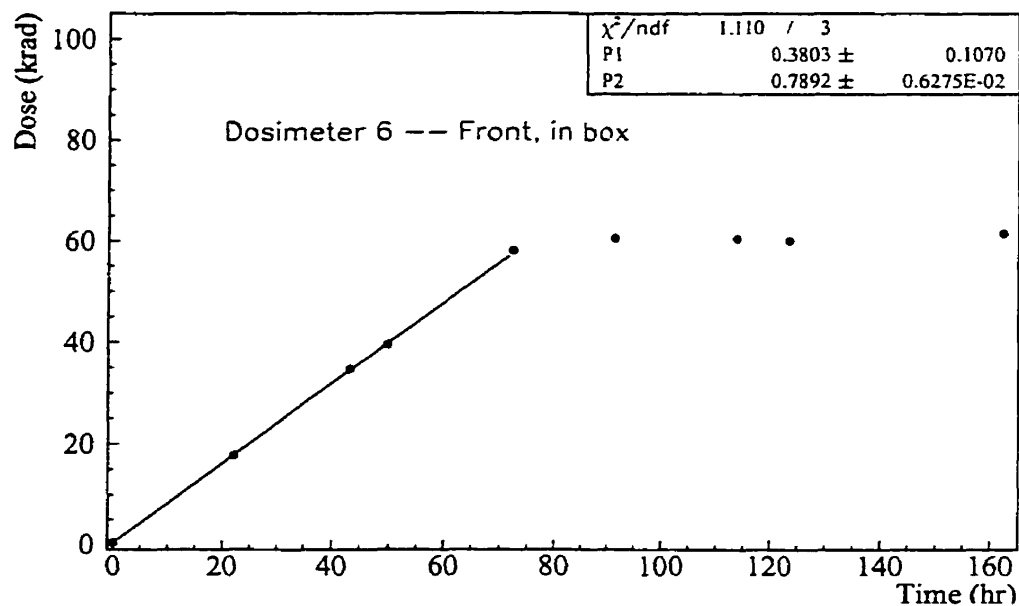


Figure 4.15: Full enclosure test: Dose versus time measured in the front central dosimeter.

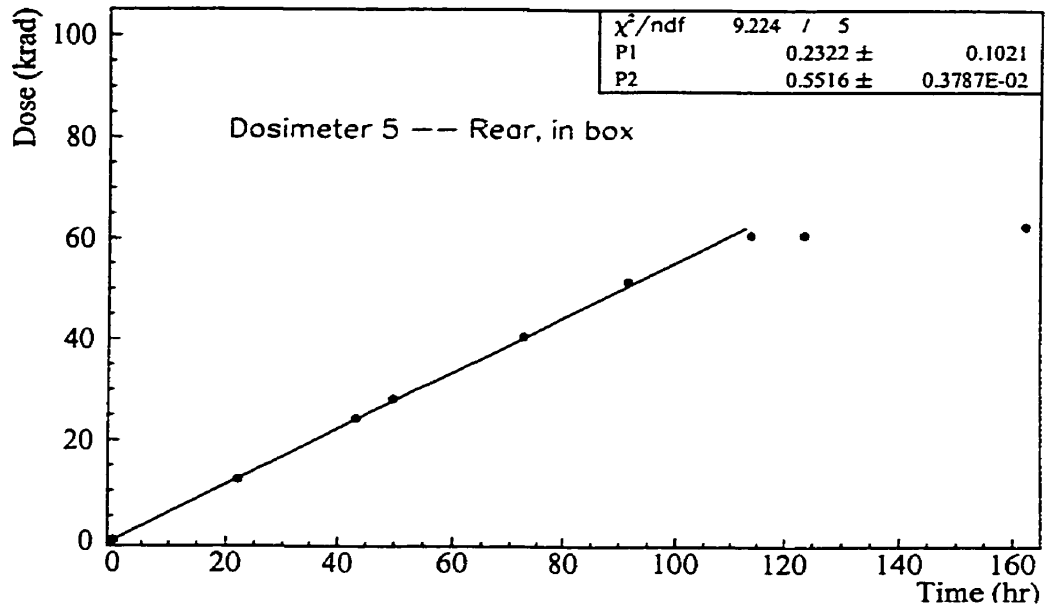


Figure 4.16: Full enclosure test: Dose versus time measured in the rear central dosimeter.

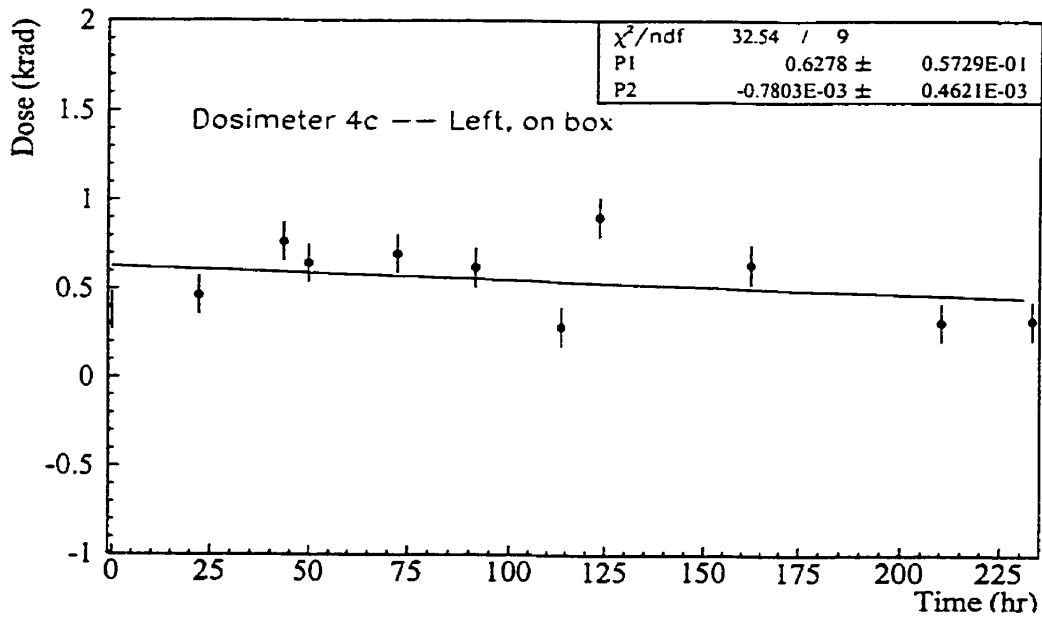


Figure 4.17: Full enclosure test: Dose versus time measured in the left backscatter dosimeter.

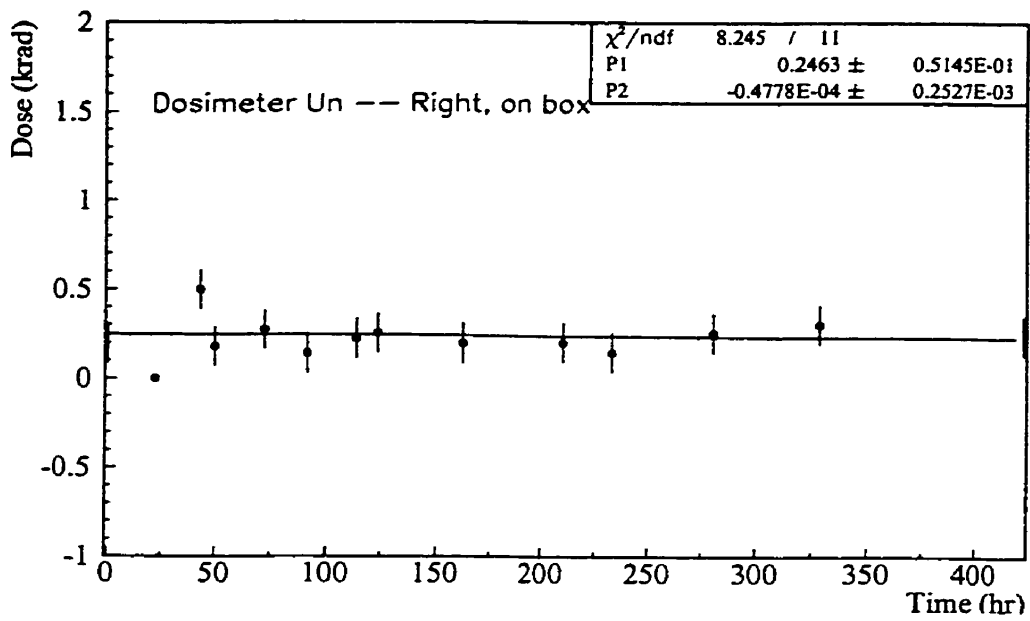


Figure 4.18: Full enclosure test: Dose versus time measured in the right backscatter dosimeter.

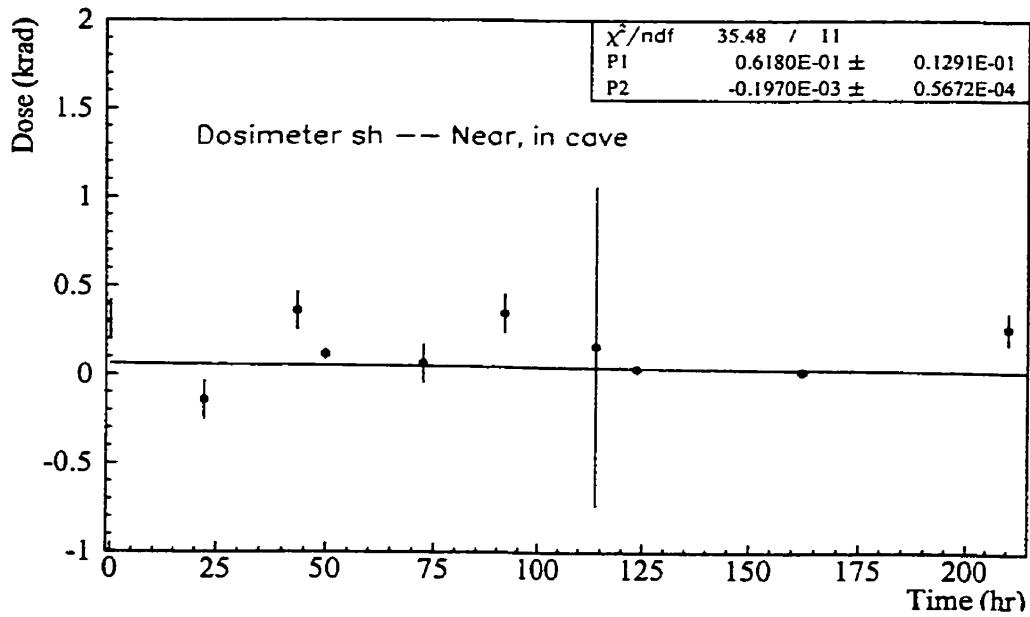


Figure 4.19: Full enclosure test: Dose versus time measured in the background dosimeter in line of radiation.

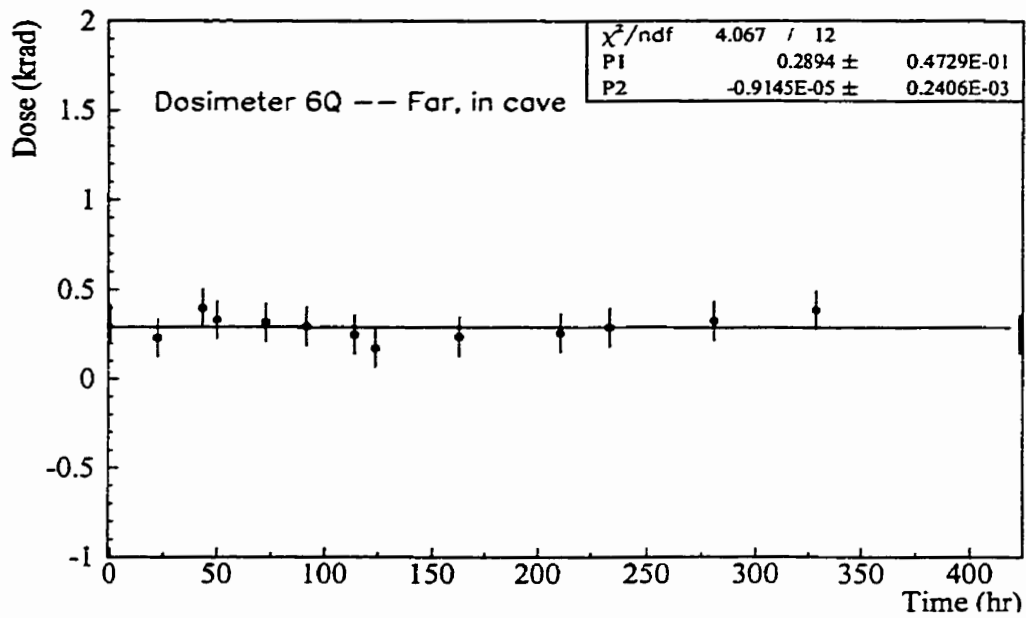


Figure 4.20: Full enclosure test: Dose versus time measured in the background dosimeter out of line of radiation.

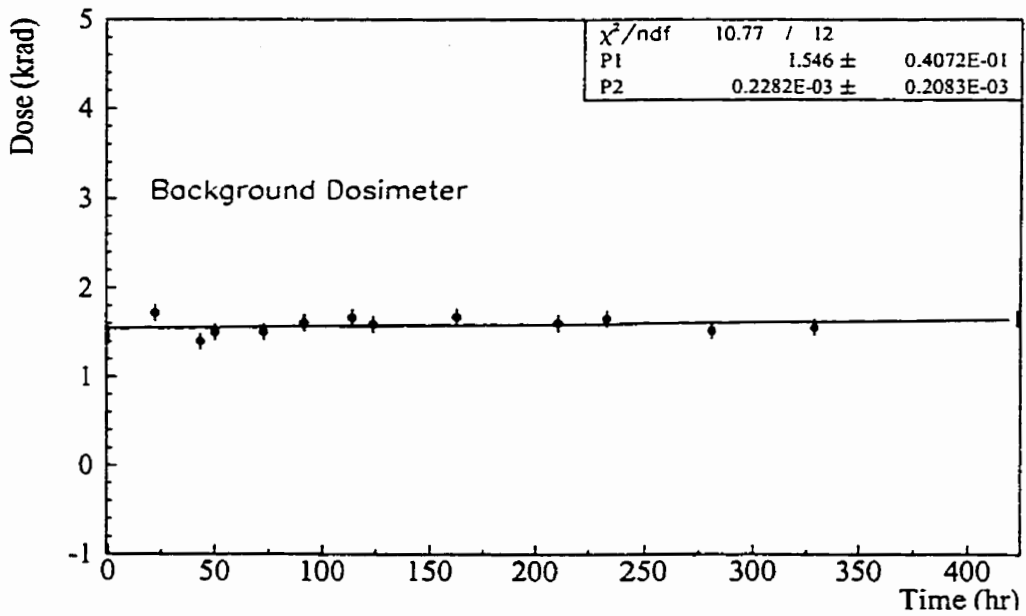


Figure 4.21: Full enclosure test: Dose versus time measured in the background dosimeter outside the cave.

The dose rates measured for the various dosimeters are given in Table 4.3. The dose rates for all vials except for the background vial are the dose rates above background.

As in previous tests, the dosimeters directly exposed to the radiation collimated by the apertures in the lead enclosure and the aluminum box received a high enough dose that their response was no longer linear. Thus, not all of the points on the plots were included in the linear fit.

| Location | Number | Dose rate (<i>rad/hr</i>) |
|------------------|------------|-----------------------------|
| Far, in box | 5 | 551.6 ± 3.8 |
| Near, in box | 6 | 789.2 ± 6.3 |
| At midpoint | | $656 \pm 4_{-6}^{+45}$ |
| Left, on box | 4c | -0.78 ± 0.46 |
| Right, on box | unnumbered | -0.05 ± 0.25 |
| Far, out of line | 6Q | -0.009 ± 0.241 |
| Far, in line | short | -0.197 ± 0.057 |
| Background | 2 | 0.23 ± 0.21 |

Table 4.3: Dose rates measured for each dosimeter in full enclosure test.

Using the material densities and attenuation coefficients for 1.25 MeV gammas provided in [16], the expected attenuations are shown in Table 4.4. Error calculations were performed assuming the same errors in distances, thicknesses, and μ_{en}/ρ values as in the previous test.

The measured total attenuation is 6.8% lower than expected. Thus, the average dose rate is reported with a 6.8% asymmetric systematic error added quadratically with the systematic error from uncertainty in expected attenuation. The statistical error from the statistical error in the dosimetry plots is also included. The expected attenuation to a point midway between the two central dosimeters

| Attenuation Source | Factor | Uncertainty |
|---|--------|-------------|
| Inverse Square Law | 0.800 | 0.007 |
| Attenuation in 2 mm glass (walls) | 0.988 | 0.003 |
| Attenuation in 1 cm Fricke solution | 0.970 | 0.002 |
| Expected Attenuation (Total) | 0.767 | 0.007 |
| Inverse Square Law (from 5 to midpoint) | 0.872 | 0.008 |
| Inverse Square Law (from midpoint to 6) | 0.897 | 0.008 |
| Attenuation in 1 mm glass (walls) | 0.994 | 0.001 |
| Attenuation in 5 mm Fricke solution | 0.9851 | 0.0009 |
| Expected Attenuation from 5 to midpoint | 0.873 | 0.008 |
| Expected Attenuation from midpoint to 6 | 0.879 | 0.008 |
| Total Measured Attenuation | 0.699 | 0.007 |

Table 4.4: Attenuation factors for dosimeters inside aluminum box.

(32.3 cm from the source) was used to find an estimate of the dose rate at the midpoint.

In summary, the dose rate in the aluminum box provides an acceptable average dose rate of $(656 \pm 4_{-6}^{+45})$ rad/hr midway between the two dosimeters. Thus, in order to irradiate the FPGAs with a total ionizing dose of approximately 100 krad(Si), they would need to be exposed for about 170 hours. (Recall from the discussion of Fricke dosimetry that under the same conditions, silicon absorbs only 90% of the dose rate that Fricke dosimetry solution receives.) No noticeable backscatter was measured inside the lead enclosure by the dosimeters placed on the aluminum box.

4.1.4 Comparison of Dose Response in Fricke Dosimeters and Thermoluminescent Detectors

The purpose of this test was to check the dose response of the Fricke dosimetry against another standard method, thermoluminescent detectors (TLDs.) In this

test, lithium borate manganese crystals were used. The dose absorbed by the TLDs was measured off-site by Saskatchewan Labour. As described in section 2.3, the measurement of total absorbed dose is done by heating the irradiated crystals to 300°C, and counting the photons emitted. After counting the photons from our TLDs, Saskatchewan Labour calibrated the measurements by exposing the TLDs to their previously calibrated X-ray source and comparing the TLD response to that expected.

A stack of lead bricks 30 cm high was built up in front of the source, with a sheet of plexiglas 0.7 cm thick placed on top. In addition to providing a flat surface for the dosimeters, the plexiglas raised the dosimeters to the level of the source, and blocked the backscattered radiation from the lead bricks.

Five Fricke dosimeter vials were placed on top of the plexiglas, at a distance of (20.0 ± 0.5) cm from the centre of the source. One vial was placed on the centre line. Two were placed to the left, at angles of 50.5° and 36.4° from the centre. Two more were placed to the right, at angles of 53.4° and 37.3° from the centre. An additional Fricke dosimeter was placed outside the radiation area, for use as a background dosimeter.

Six TLDs were also placed on top of the plexiglas sheet, 20 cm from the centre of the source. Two TLDs were placed to either side of the central Fricke dosimeter vial. Two more TLDs were placed next to the two vials on the left, and the last two were placed next to the two vials on the right. In addition, two TLDs were not exposed to radiation, but were used as control dosimeters. The setup for the combined TLD and Fricke dosimetry test is shown in figure 4.22.

The optical absorption of all six Fricke dosimeter vials was measured before irradiation began, and five more times over the course of the experiment. Equation

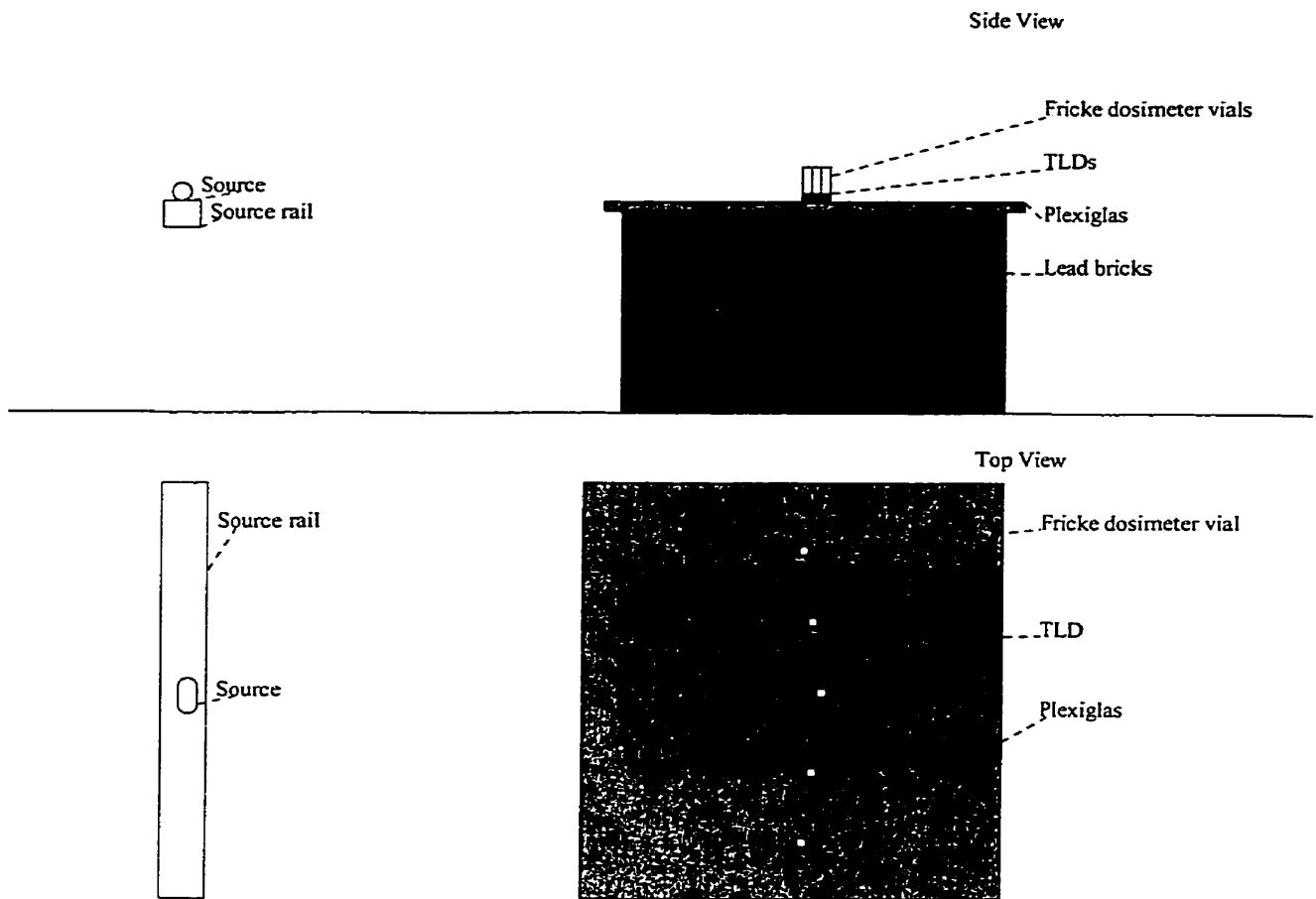


Figure 4.22: Setup for combined TLD and Fricke dosimetry test, not to scale.

2.8 was then used to determine the absorbed dose. After propagation of errors, the results were plotted in figures 4.23 (far left), 4.24 (near left), 4.25 (central), 4.26 (near right), and 4.27 (far right). Note that the background Fricke dosimeter was marked as number 1. The results from all five Fricke dosimeters are plotted together in figure 4.28. This results in a average dose rate of (1.787 ± 0.005) rad/hr.

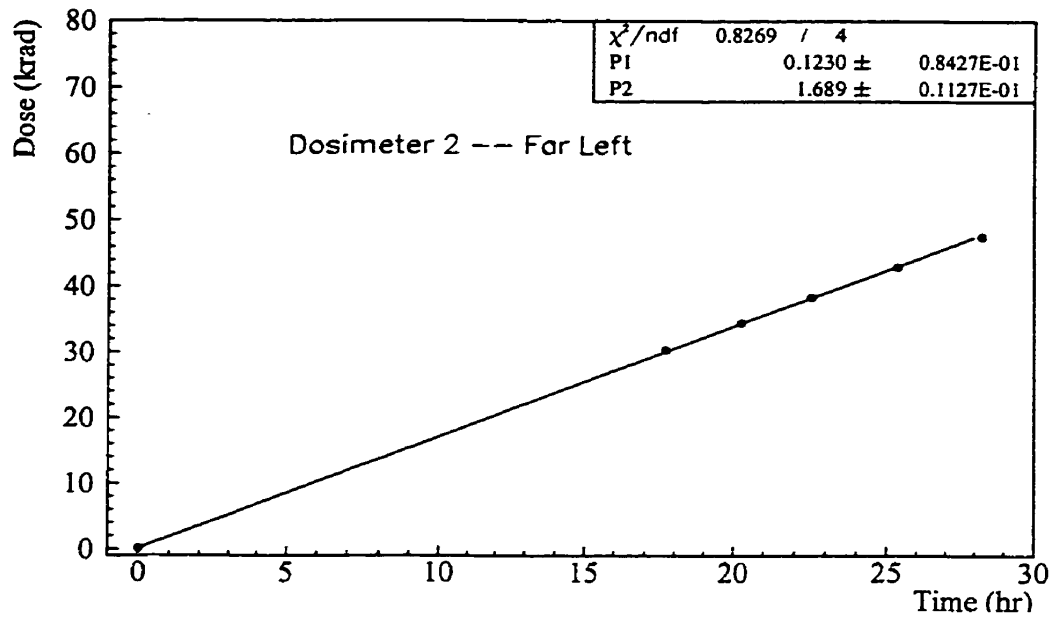


Figure 4.23: Combined TLD and Fricke test: Dose versus time measured in the far left dosimeter.

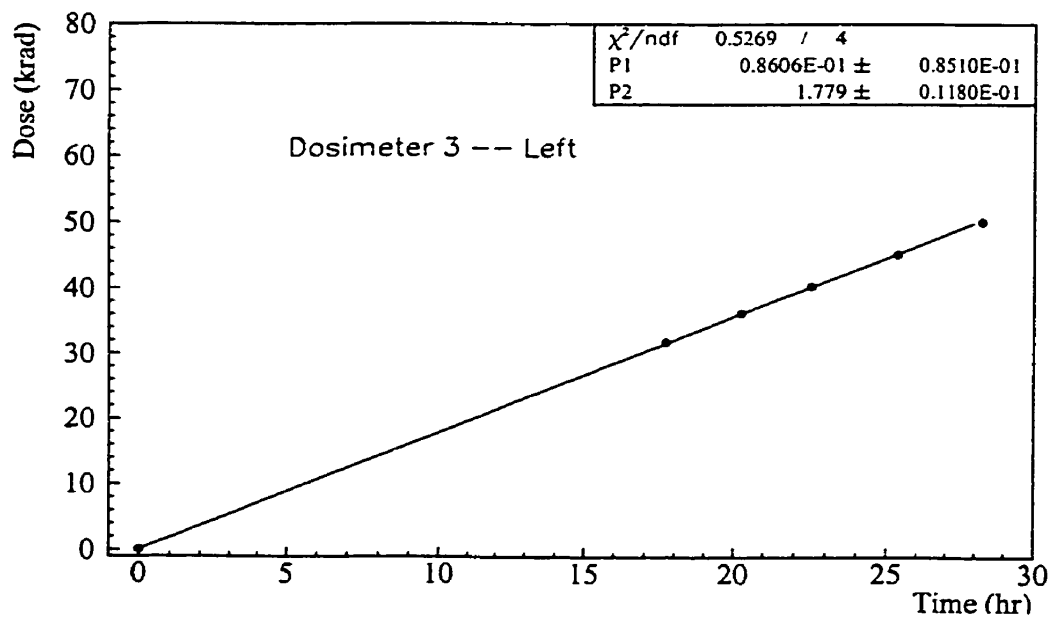


Figure 4.24: Combined TLD and Fricke test: Dose versus time measured in the near left dosimeter.

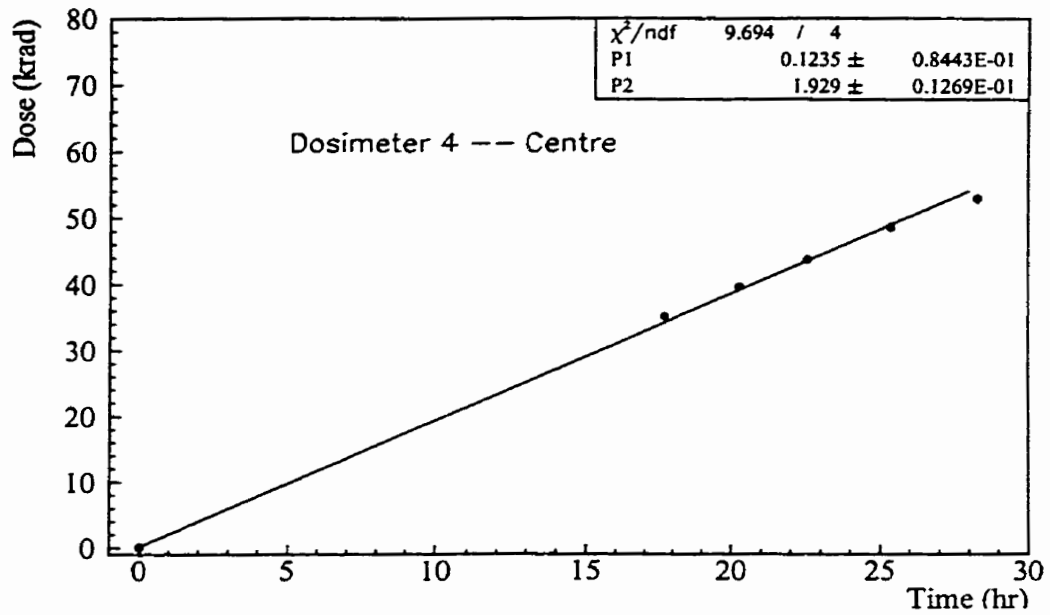


Figure 4.25: Combined TLD and Fricke test: Dose versus time measured in the central dosimeter.

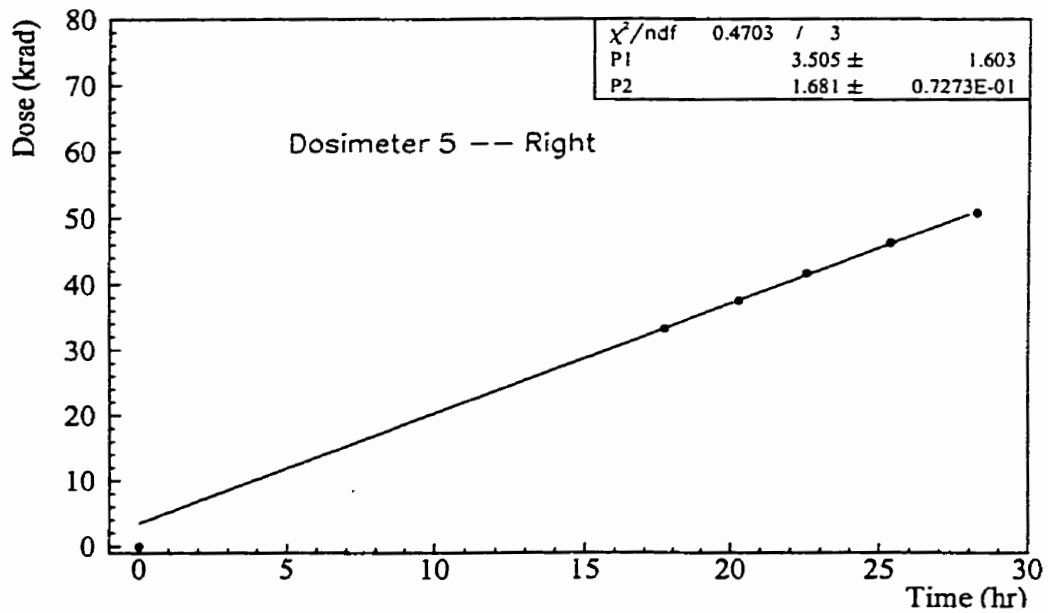


Figure 4.26: Combined TLD and Fricke test: Dose versus time measured in the near right dosimeter.

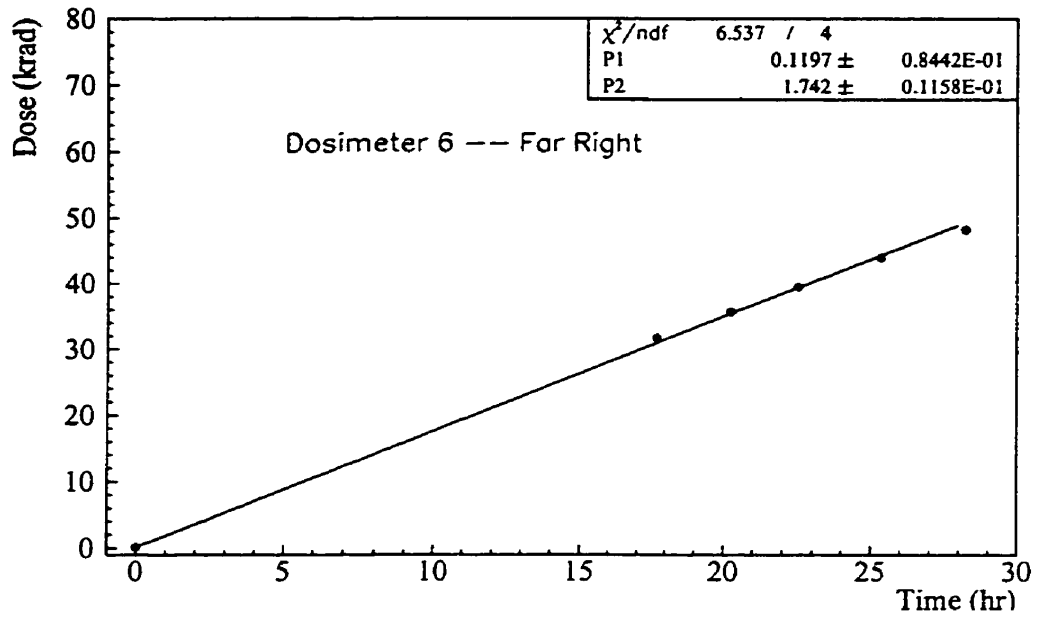


Figure 4.27: Combined TLD and Fricke test: Dose versus time measured in the far right dosimeter.

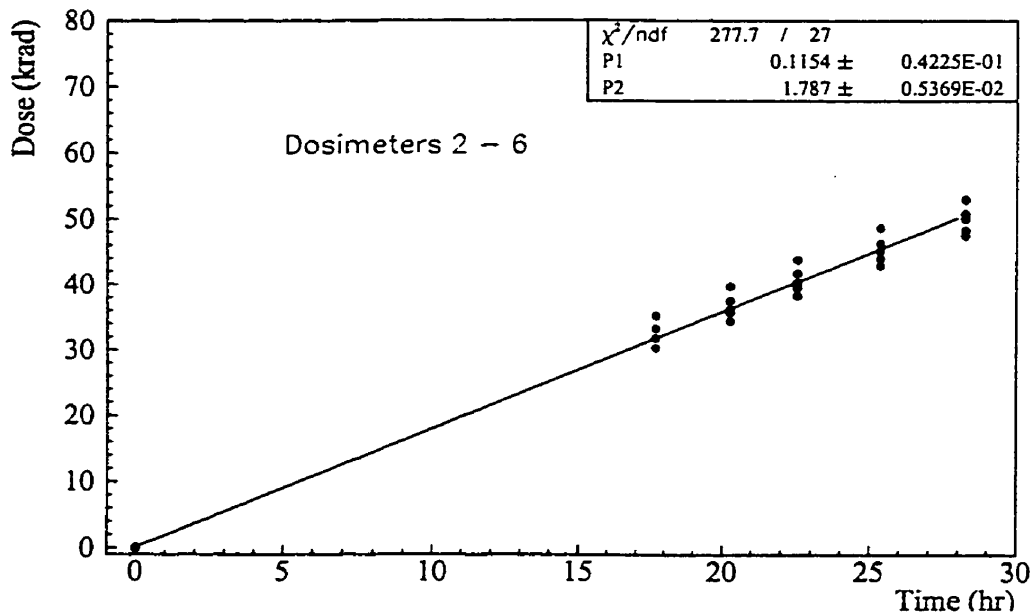


Figure 4.28: Combined TLD and Fricke test: Dose versus time measured in all irradiated Fricke dosimeters.

Fricke dosimeters 2, 3, 5, and 6 (the vials placed off the centre line) each had a single TLD placed beside them. Dosimeter 4, at the centre line, had one TLD placed at either side. In order to minimize the number of trapped electrons and holes in the TLDs, they were heated at 260 °C for 50 minutes before the test began.

During the test, the cobalt-60 source was removed and the radiation area was accessed five times. Each time, the Fricke dosimeter vials were taken away for their optical densities to be measured. At the same time, one of the TLDs would be removed and sealed in an envelope to be read at a later time. The Fricke dosimeters were then put back in their original positions, and the radiation was turned back on. The final TLD was removed at the end of the test, when all of the Fricke dosimeters were saturated.

Table 4.5 shows the dose read for each TLD, together with the dose absorbed by the nearest Fricke dosimeter at the time it was removed. The 10% error in the TLD readings is the systematic error reported by Saskatchewan Labour [38]. While TLDs 1a, 1b, 4a, 5, and 6 agree quite well with the Fricke estimates, TLDs 2, 3, and particularly 4b do not.

| TLD | Location | Time Irradiated (hr) | Dose in Fricke (<i>krad</i>) | Dose in TLD (<i>krad</i>) |
|-----|------------------|----------------------|--------------------------------|-----------------------------|
| 1a | Control(1) | 0 | 0 | 0 |
| 1b | Control(2) | 0 | 0 | 0 |
| 2 | Fricke #2 | 25.350 ± 0.017 | 42.82 ± 0.28 ± 0.03 | 62 ± 6 |
| 3 | Fricke #3 | 17.700 ± 0.008 | 31.49 ± 0.21 ± 0.01 | 54 ± 5 |
| 4a | Fricke #4(right) | 45.517 ± 0.019 | 87.80 ± 0.59 ± 0.04 | 85 ± 9 |
| 4b | Fricke #4(left) | 28.250 ± 0.019 | 54.49 ± 0.37 ± 0.04 | 163 ± 16 |
| 5 | Fricke #5 | 20.267 ± 0.012 | 34.07 ± 1.48 ± 0.02 | 34 ± 3 |
| 6 | Fricke #6 | 22.533 ± 0.014 | 39.25 ± 0.27 ± 0.02 | 41 ± 4 |

Table 4.5: Dose measured for each TLD compared to dose estimated using nearest Fricke dosimeter.

Figure 4.29 plots the dose read for each TLD against the time it was irradiated. This results in a dose rate of (1.669 ± 0.337) krad/hr. This dose rate agrees within error with all five Fricke dosimeters irradiated, and is 6.6% lower than the dose rate found by fitting all five irradiated Fricke dosimeters together.

Note that the result from TLD 4b is not included in the linear fit. As its dose is so far from what would be expected based on the other TLD results (specifically, it read a dose nearly twice as much as TLD 4a, which was irradiated for nearly twice as long), we believe the dosimeter may have been defective. Finally, the fact that the average dose rate measured from the TLD readings comes from measurements of dosimeters which were not in the same position, and thus may not have absorbed exactly the same dose rate, must be taken into consideration.

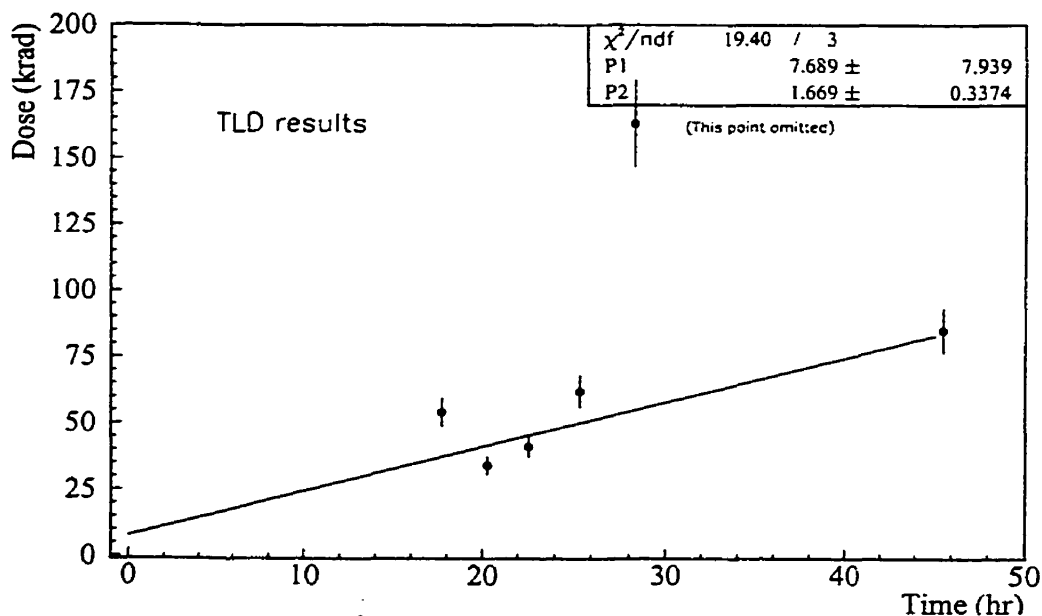


Figure 4.29: Combined TLD and Fricke test: Comparison of TLD results to time spent under irradiation.

Table 4.6 summarizes the dose rates measured for each dosimeter irradiated.

| Location | Number | Dose rate (<i>krad/hr</i>) |
|--------------------------|--------|------------------------------|
| <i>Fricke Dosimeters</i> | | |
| Far left | 2 | 1.689 ± 0.011 |
| Near left | 3 | 1.779 ± 0.012 |
| Centre | 4 | 1.929 ± 0.013 |
| Near right | 5 | 1.681 ± 0.073 |
| Far right | 6 | 1.742 ± 0.012 |
| <i>Dosimeters 2 - 6</i> | | 1.787 ± 0.005 |
| <i>TLD result</i> | | 1.669 ± 0.337 |

Table 4.6: Dose rates measured for each Fricke dosimeter irradiated for combined TLD and Fricke test.

The results from the TLDs and the Fricke dosimeters can be compared by taking the dose results expected from the best-fit line in figure 4.28, and comparing them to the dose results actually found for the TLDs. This can be used to find a chi-squared value for the TLD results, using the equation from reference [39]

$$\chi^2 = \sum \left(\frac{D_T - D_F}{\delta D_T} \right)^2, \quad (4.6)$$

where D_F is the dose result in Fricke from the best fit line in figure 4.27, D_T is the dose read from the TLDs, and the summation is over all irradiated TLDs. This results in a chi-squared value of 25. When divided by the number of degrees of freedom (5), this gives a reduced chi-squared value of 5. (There are five degrees of freedom in this case, as there are five data points and no constraints are calculated from them. The TLD data points are compared to the fit calculated independently from the Fricke data.) By the chi-squared probability table in [39], there is a probability of less than 0.05% that these results would be obtained if the TLD dose readings were expected to follow the results from the Fricke dosimeters. However, the chi-squared was dominated by TLDs 3 and 2 – TLDs 5, 6, and 4a were very

close to the fit expected from Fricke dosimetry.

Figure 4.30 plots the residuals ($D_T - D_F$) for each TLD against the time under irradiation. Figure 4.31 shows the distribution of the residual values, along with a fit to a Gaussian curve. Partly because there are so few data points, the uncertainty in the parameters of the fit is large, with a mean residual of (7 ± 18) krad, and a standard deviation of (12 ± 38) krad.

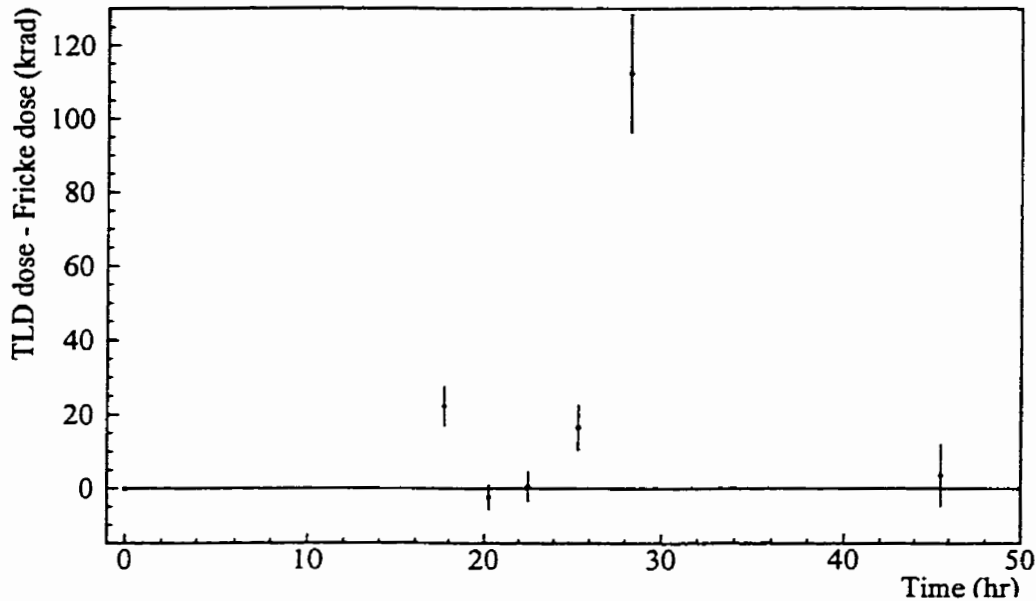


Figure 4.30: Combined TLD and Fricke test: Plot of residuals between TLD and Fricke results.

Figure 4.32 is a histogram of the distribution of the individual contributions to the chi-squared value from each irradiated TLD. It also includes a fit to a distribution of the form

$$f(\chi^2) = A(\chi^2)^B e^{-\chi^2/2}, \quad (4.7)$$

which is the expected form for a chi-squared distribution. For a distribution of five

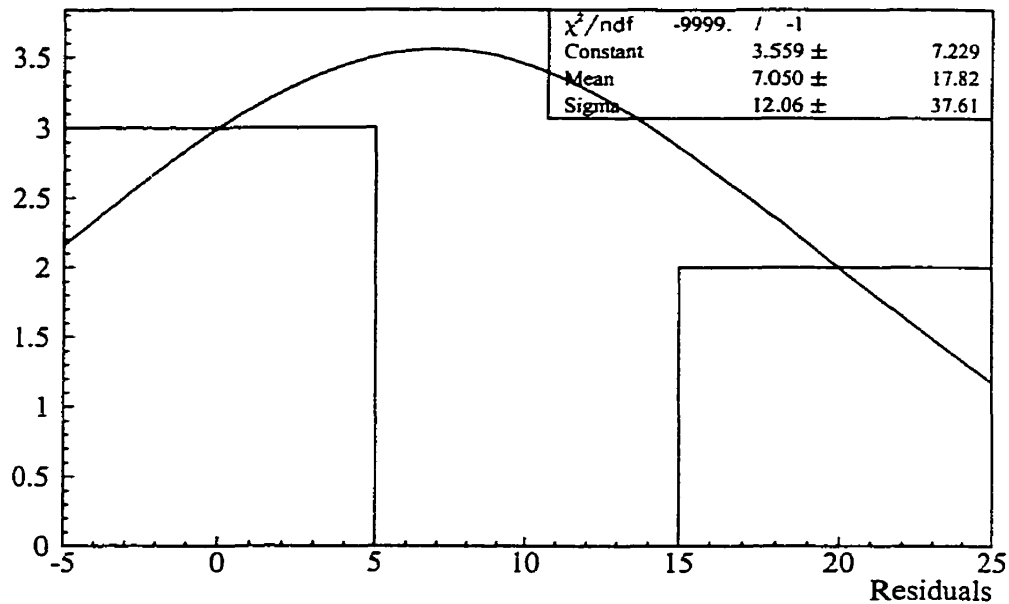


Figure 4.31: Combined TLD and Fricke test: Distribution of residuals, compared to a Gaussian fit.

data points with 5 degrees of freedom, A was expected to be 0.665, while B was expected to be 1.5. However, the fit returned values of 1.6 ± 12.7 and 1.9 ± 5.0 , respectively. As in figure 9, much of the uncertainty is due to the fact that there were only five data points.

The dose rate results from the TLDs agreed, within error, to the dose rates given by the Fricke dosimeters. However, it must be noted that one TLD measurement had to be rejected due to bad agreement with other measurements. It must also be noted that the TLD response was much less linear over time than the Fricke dosimeter response was. Finally, the results of a chi-squared test comparing the TLD readings to the results from Fricke dosimetry show significant disagreement.

As the TLDs show a less linear response, and must be sent off-site to be read, they are not preferred for our purposes. Fricke dosimetry is a better choice for

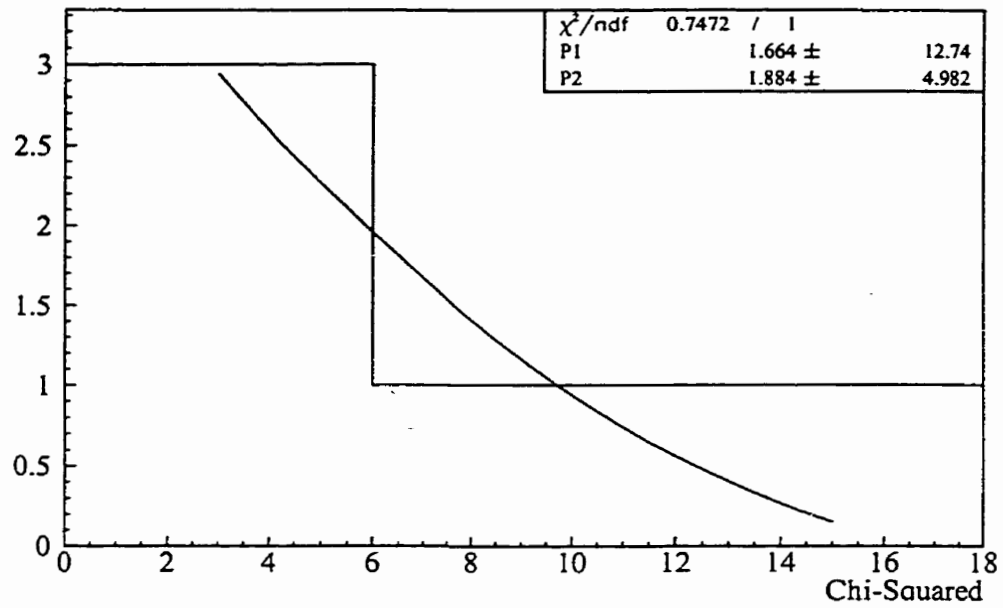


Figure 4.32: Combined TLD and Fricke test: Distribution of individual contributions to chi-squared.

total ionizing dose tests of electronics, mainly because Fricke dosimetry results are self-consistent.

4.2 Setup for Radiation Tests of FPGAs

To test the radiation tolerance of the Xilinx FPGAs, a small printed circuit test board (PCB) was built. This test board had an FPGA socket soldered to it, which allowed the FPGA on the board to be changed quickly. A 40 MHz oscillator, switches, connectors, a fuse and a small number of passive components were also present. The cobalt-60 source described earlier was used as our source of ionizing radiation.

As in the previous test described in subsection 4.1.3, an enclosure or “keep” was constructed from 5 x 10 x 15 cm lead bricks, and an aluminum box was placed inside the enclosure with its aperture, aligned with the keep’s aperture, and thus the source. This box contained a rack for the PC board which kept the PC board upright, so that the FPGA was centered on the aperture and thus in line of the radiation. The bottom of the PC board was facing the source, with the socket for the FPGA on the side facing away from the source.

Two small platforms were built into the box for the dosimeter vials – one in front of the PC board, and another behind. The lid of the box had two of the corners cut out, so that wires and cables could connect the FPGA to the test components outside the radiation area. The lid of the aluminum box was removable, so that the PC board and the dosimeters could be accessed. Figure 4.33 shows the setup used for the radiation tests of FPGAs.

During the tests, the PC board was connected to three external devices. The first was a function generator. This function generator provided triggers at a rate of 10 to 20 kHz. It was located within the radiation area, but out of the direct line of radiation and shielded from the source by the lead enclosure.

The PCB was also connected to a power supply outside the radiation area.

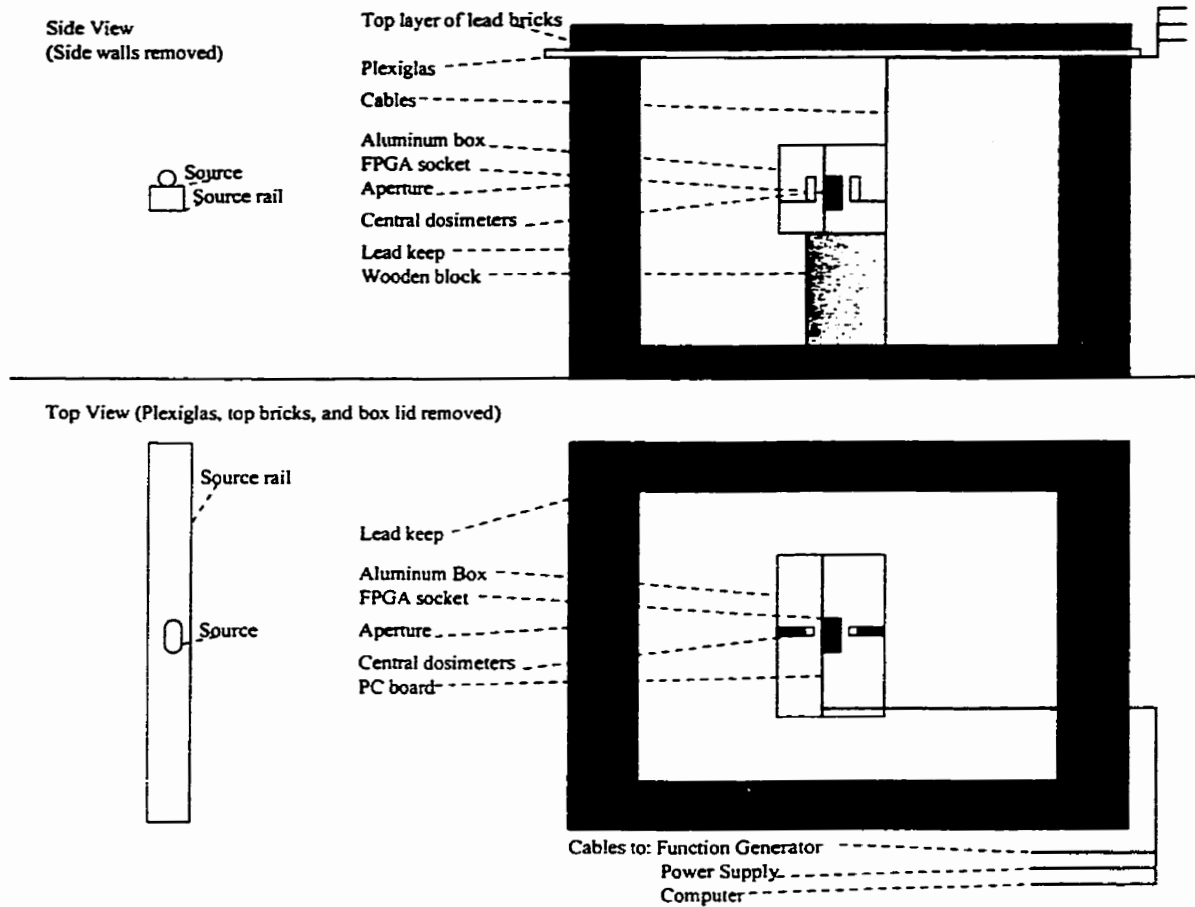


Figure 4.33: Setup for radiation tests of FPGAs, not to scale.

This power supply provided two voltage levels – an FPGA voltage of 3.3 V during operation and a voltage of 5.0 V during circuit configuration. The power supply also had a meter which was used to monitor the power supply current.

Finally, the FPGA was connected to a personal computer kept outside the radiation area. The downloading of the configuration circuit and the monitoring of the FPGA were performed by this computer. The code used to monitor the FPGA is discussed in the next section.

4.3 Monitoring Program

During tests of the FPGAs, control and monitoring of the FPGA was carried out by a computer program written in C and run by a PC using the Linux operating system. A more complete description of the program and its implementation can be found in reference [40].

This program, at the beginning of the run, would download the configuration circuit into the FPGA. The configuration was stored in a separate file. It would also download a default set of parameters to the circuit.

In addition to configuring the FPGA, the monitoring program was responsible for error monitoring. If an error occurred during the FPGA's operation, a signal was sent via a connection to the PC's parallel port. The program would record the error type and the time in both human-readable (ASCII) and machine-readable (binary) log files. The ASCII log file was also displayed on the monitor during the test.

The program would first try to clear the error condition by transmitting a reset pulse. If the error condition was cleared, and the circuit operated without error for more than some specified time interval (in these tests, one second), the program assumed that the reset pulse had cleared the problem. If the problem was not cleared, another error would be recorded, and another reset pulse would be sent. If one hundred consecutive reset pulses failed to clear the error, the program would download the circuit configuration again. This too would be recorded in the log files. If the download was not successful, the program would record that error and try to download the file again, continually recording the errors found in each successive download, until it was successful or the test was stopped.

Several different types of errors could be detected and reported by the monitoring program. Only three types were reported during the tests described in this thesis. The first, the sequence or SEQ error, was the result of the FPGA failing to properly order the capacitor addresses for the SCA. The second, the P-clock error, meant that signals from the 40 MHz oscillator mounted on the FPGA board were no longer being received by the FPGA circuit. Both of these errors were “soft” errors which could usually be cleared with a circuit reset. The third, the InitHigh error, was a “hard” error resulting from an unsuccessful download of the configuration circuit. It was flagged if an attempt to download the configuration again after one hundred soft errors resulted in the Init pin remaining high, rather than going low as would occur if the download was successful.

Finally, the program was responsible for communicating with the experimenters. When the monitoring program started up, it would write a status message in the ASCII log file, showing that one attempt was made to download the configuration circuit. It would then begin to record errors (if any) in both log files. On startup, the program would also read a command file and execute its commands. During these tests, the only commands in the file were instructions to send a status message to selected experimenters via electronic mail. This status message included the total uptime so far, the total number of errors of various types, the total number of attempts to download the configuration circuit, and the number of errors and downloads recorded since the last status message was sent. The command file also told the program how long to wait before executing the commands in the command file again. This interval was initially set to one day, but could be changed by the experimenter simply by editing the command file.

4.4 Interpolation of Dose Rates to the FPGA Die

As seen in figure 4.33, the FPGA was directly in the line of the radiation from the source, with one dosimeter in front of it and one dosimeter behind. The dose rate at the die of the FPGA was determined using the dose rates from both Fricke dosimeter vials, and correcting for the attenuation of the radiation intensity due to passage through intervening matter and the inverse square law.

Between the front dosimeter and the FPGA die, the PC board and a copper heat sink served to attenuate the radiation. Between the FPGA die and the rear dosimeter, the lid of the FPGA's package and the top of a plastic socket attenuated the radiation. In addition to the attenuation from parts on the board, the attenuation of the radiation from the centre of the Fricke dosimeters to the die had to be taken into account. Finally, the inverse square law resulted in a lowered intensity of the radiation between the dosimeters and the die. As in the full-enclosure pretest, the dosimeters were 30.5 cm and 34.1 cm from the source. The FPGA die was 32.6 cm from the source.

As in the pretests, the attenuation formulae (equations 4.4 and 4.5) were used. The material densities and attenuation co-efficients for 1.25 MeV gammas provided in reference [16] were used. Error calculations were performed assuming 0.1 cm error in the distances from the source of the dosimeters and the FPGA die, the errors in material thicknesses stated in table 4.7, and the error in reference [16]'s μ_{en}/ρ values of $1 \times 10^{-3} \text{cm}^2/\text{g}$. As the exact compositions of the plastics used were unknown, their μ_{en}/ρ values were approximated by using carbon (graphite).

Thus, the dose rate at the die estimated from the front dosimeter was

| Attenuation Source | Factor | Uncertainty |
|---|--------|-------------|
| Front dosimeter to FPGA die | | |
| Inverse square Law | 0.8773 | 0.0122 |
| Glass walls (1.000 ± 0.0025 mm) | 0.9941 | 0.0014 |
| Fricke solution (5.000 ± 0.0025 mm) | 0.9851 | 0.0008 |
| PC board (2.02 ± 0.01 mm) | 0.9909 | 0.0003 |
| Cu heatsink (1.76 ± 0.01 mm) | 0.9624 | 0.0015 |
| <i>Total</i> | 0.819 | 0.012 |
| FPGA die to rear dosimeter | | |
| Inverse Square Law | 0.9119 | 0.0124 |
| Glass Walls (1.000 ± 0.0025 mm) | 0.9941 | 0.0014 |
| Fricke Solution (5.000 ± 0.0025 mm) | 0.9851 | 0.0008 |
| Package lid and socket (6.27 ± 0.02 mm) | 0.9720 | 0.0010 |
| <i>Total</i> | 0.868 | 0.012 |

Table 4.7: Attenuation factors used to find dose rate in FPGA die.

$$D = (0.819 \pm 0.012)(D_{\text{Front dosimeter}}), \quad (4.8)$$

and the estimate from the rear dosimeter was

$$D = (D_{\text{Rear dosimeter}})/(0.868 \pm 0.012). \quad (4.9)$$

A weighted average would then give the dose rate at the die. Note that this dose rate would be the dose rate in Fricke solution, and a further material correction (equation 2.20) would need to be made to give the dose rate in Si.

4.5 Test Procedure

Before the radiation tests began, the FPGA was placed on the PC board and taken to the radiation area (the cave). Here, the power supply, function generator, and computer were connected, the monitoring program was turned on, and the FPGA received the monitoring configuration. This was done to ensure that the FPGA worked properly before irradiation. If errors were recorded, the test would have to be halted until the cause of the problem was isolated.

After twelve to twenty-four hours of error-free operation, the monitoring program was restarted. At the same time, the radiation source would be pushed out of its hutch. The power supply current would be recorded, along with the time, the voltages, and the room temperature. These checks were continued at intervals over the course of the test. The time between checks of the current varied over the course of the test, from twice a day during periods where the current was expected to remain stable, to once every half hour when continuous errors were expected to occur.

During the course of the radiation tests, three Fricke dosimeters were used to calculate the dose received by the FPGA. One dosimeter was placed in front of the FPGA, one was placed behind the FPGA, and another was placed outside the radiation area. In order to periodically check the optical absorption of the dosimeter vials, the source had to be retracted into its hutch to allow access to the cave. As well, the top layer of lead bricks, the plexiglas slab, and the top of the aluminum box had to be removed. This often resulted in temporary bad connections between the FPGA and the power supply or the function generator. As a result, a logic error would be recorded by the circuit which would be cleared by a circuit reset. These logic errors would be recorded by the monitoring program, and would also

be recorded in the experiment logbook to avoid confusing them with genuine errors caused by radiation effects.

After their optical densities had been measured, the dosimeters were returned to their positions, and the radiation was turned back on. During the 10 to 12 minutes that the radiation was turned off, the FPGA continued to run. Corrections to the total time under irradiation were thus made.

Fricke dosimetry, described in earlier sections, was used to calculate the dose received by the FPGA.

After the FPGA errored continuously, the monitoring program would be turned off and the radiation source would be retracted. The PC board would be placed in an anti-static bag, and taken along with the power supply and the function generator to the Centre for Subatomic Research. The FPGA would then be reconnected to the power supply and function generator. The PC board would be put in the oven. The oven was heated to $50 \pm 2^\circ\text{C}$. Power supply current, voltages, and the temperature of the oven were recorded.

After fourteen days in the oven, the PC board, FPGA, power supply, and function generator were taken back to the cave. Again, the monitoring program would be run to check that the FPGA was functioning properly. After twelve to twenty-four hours of error-free operation, the monitoring program would be restarted and the radiation would be turned on. The current, voltages, and temperatures would then be monitored approximately once per hour until continuous errors were recorded. Then, the radiation would be turned off, and the FPGA on the PC board would be replaced with the next FPGA to be tested.

CHAPTER 5

Results

Four XC4036XL FPGAs and three XC4036XLA FPGAs were exposed to gamma radiation from a cobalt-60 source. After showing increased power supply current and continuous logic errors, the FPGAs were removed from the radiation cave and annealed in an oven for fourteen days. At the end of the annealing period, the FPGAs were subjected to a second irradiation period.

5.1 Test Results for XC4036XL Devices

Four XC4036XL-1HQ240C FPGAs were irradiated with a cobalt-60 source, using the setup described in section 4.2 and the procedure described in section 4.5. The results of these tests have been previously presented in references [41], [42], and [43]. In this section, the four FPGAs tested will be referred to as FPGA A, FPGA B, FPGA C, and FPGA D.

The date codes for the four FPGAs are given in table 5.1. Of the four FPGAs tested, only A and B had the same date code. This may explain why C and D showed slightly different behaviour while annealing and while under irradiation. All of the FPGAs were fabricated at UMC in a $0.35 \mu\text{m}$ CMOS process [44].

The dose rate for each test was determined using Fricke dosimetry, as outlined in previous sections of this thesis. The dose rates are given in table 5.2. The dose rate in Fricke solution was determined through interpolation of the dose rates calculated from the optical absorbtion measurements of the dosimeter vials in front of and behind the FPGA. This was converted to the dose rate in silicon using equation 2.20. The dose rate is reported with a statistical error from the fitting of the absorbtion versus time plots used to find the dose rates in the dosimeter vials. Systematic error from the uncertainty in the attenuation of the dose rate between the dosimeter vials

| FPGA | Date code |
|------|-----------|
| A | 9737 |
| B | 9737 |
| C | 9725 |
| D | 9733 |

Table 5.1: Date codes for XL FPGAs.

| FPGA | Dose rate in Fricke (rad/hr) | Dose rate in Si (rad/s) |
|------|------------------------------|--------------------------------|
| A | $533 \pm 2 \pm 8$ | $0.1332 \pm 0.0006 \pm 0.0019$ |
| B | $533 \pm 4 \pm 7$ | $0.1333 \pm 0.0009 \pm 0.0017$ |
| C | $538 \pm 4 \pm 7$ | $0.1346 \pm 0.0009 \pm 0.0017$ |
| D | $487 \pm 6 \pm 6$ | $0.1218 \pm 0.0015 \pm 0.0016$ |

Table 5.2: Dose rates measured for each XL FPGA tested.

and the FPGA is also included.

Table 5.3 shows the doses absorbed by the FPGAs before failure. In the first irradiation period, two different types of failure are considered – increase in power supply current and logic errors. In the second irradiation period, only the dose absorbed up to the first logic error was recorded, as the power supply current begins to increase immediately during the second irradiation period.

The absorbed doses are reported with a statistical error coming from the statistical error in the dose rate, and a systematic error coming from the systematic errors in the dose rate and the time elapsed before failure. In the cases of current increase, the systematic error in time was taken to be one half the time elapsed between the current recording just before and just after the current increased. In the case of the first error in the first irradiation period, the error came from the uncertainty in time under irradiation due to turning the radiation off for dosimetry measurement. For the second period, no dosimetry was carried out, so a 30 second error in the time was assumed due to possible inaccuracies in reading the clock used to time the experiment. A weighted average of the absorbed doses until failure for the four FPGAs was also determined, with the standard deviation used as the error in the average dose.

| FPGA | Dose absorbed (krad(Si)) | | |
|---------|--------------------------|---------------------------|---------------------------|
| | to current increase | to first error (period 1) | to first error (period 2) |
| A | 40.1 ± 0.2 ± 3.2 | 56.2 ± 0.2 ± 0.8 | 3.45 ± 0.01 ± 0.05 |
| B | 41.0 ± 0.3 ± 2.7 | 58.6 ± 0.4 ± 0.7 | 4.50 ± 0.03 ± 0.06 |
| C | 41.0 ± 0.3 ± 1.2 | 63.7 ± 0.4 ± 0.8 | 6.63 ± 0.04 ± 0.08 |
| D | 36.5 ± 0.5 ± 0.8 | 58.2 ± 0.7 ± 0.7 | 4.59 ± 0.06 ± 0.06 |
| Average | 39 ± 2 | 59 ± 3 | 4 ± 1 |

Table 5.3: Results from irradiation of XL FPGAs.

5.1.1 First Irradiation Period

Figure 5.1 shows the power supply current versus total absorbed dose for the first irradiation period of the four XL FPGAs. The average dose absorbed by the XL chips before an increase in power supply current to 0.01 A above the value before irradiation was (39 ± 2) krad(Si). After the onset of current increase, monitoring continued until the onset of errors.

One anomaly occurred during the testing of FPGA C which is not shown in figure 5.1. Sometime between 52.183 hours and 70.333 hours, the current dropped from 0.34 A to 0.20 A. At 72.233 hours, the monitoring program and the power supply were turned off. At 72.250 hours, the power supply was turned on, and the monitoring program restarted and reloaded the circuit. The current returned to 0.34 A.

The average dose absorbed until the first error was recorded was (59 ± 3) krad(Si). Address sequence errors were the only type of error recorded in the tests of the XL FPGAs. The monitoring program would attempt to clear these errors by sending a circuit reset signal. Only after one hundred continuous errors could not be cleared by a circuit reset would the monitoring program attempt to

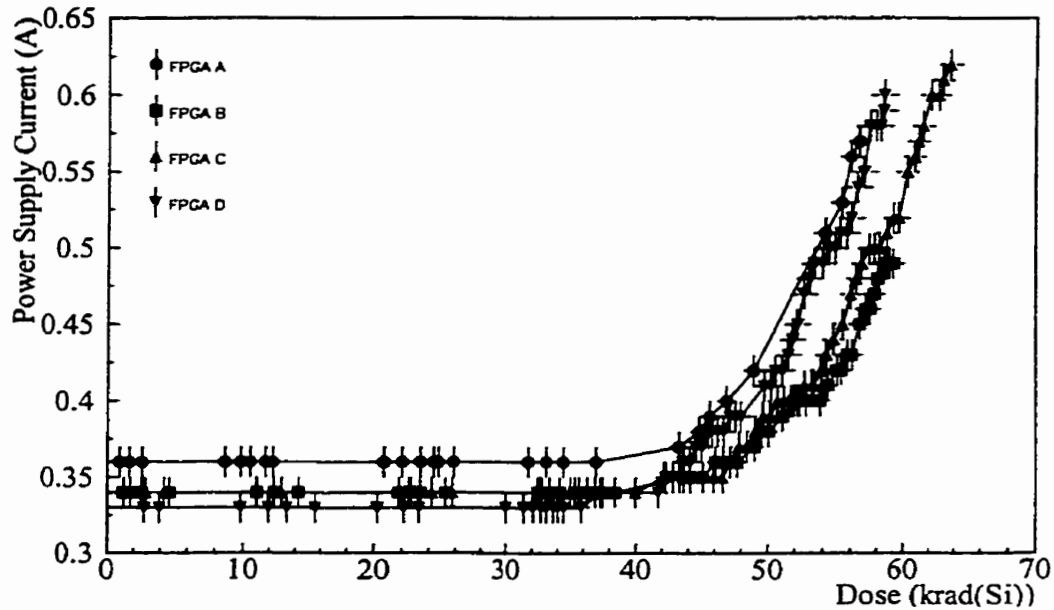


Figure 5.1: Current versus dose for XL FPGAs, first irradiation period.

reload the configuration circuit.

Figure 5.2 shows, for all four XL FPGAs, the total number of address sequence errors versus time after the first error was recorded. Although the error rate starts out slowly for most of the FPGAs, it eventually increases towards continuous errors. FPGA C, on the other hand, began to error very quickly, reaching one thousand sequence errors within the first half hour. FPGA B's errors are seen to "level off" twice. In some cases, this may be because reloading the circuit temporarily resulted in a lower error rate.

5.1.2 Annealing Period

Figure 5.3 shows the current versus time for the four XL FPGAs during their annealing period. After the chip was removed from the radiation cave and transferred

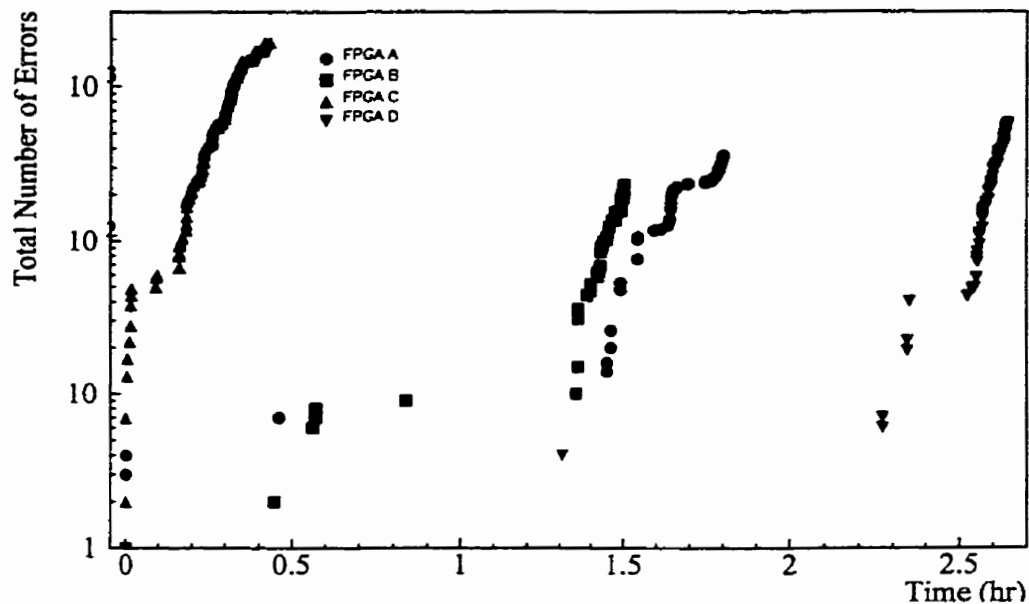


Figure 5.2: Errors versus time since first error for XL FPGAs, first irradiation period.

to the oven, the current began to rise as the oven heated up to $(50 \pm 2)^\circ\text{C}$. The first points on the graph were recorded when the FPGA's current had reached its maximum, and the oven was finished heating up.

FPGA C shows two discontinuities in its current. The first occurred after 3.5 days in the oven, when the chip was removed from the oven for about 30 minutes. This resulted in a decrease in the current – even after being returned to the oven, the current did not increase back to the level it showed before being removed. However, between 13.5 and 14 days, the current increased substantially, even though temperature and power supply voltage had remained constant.

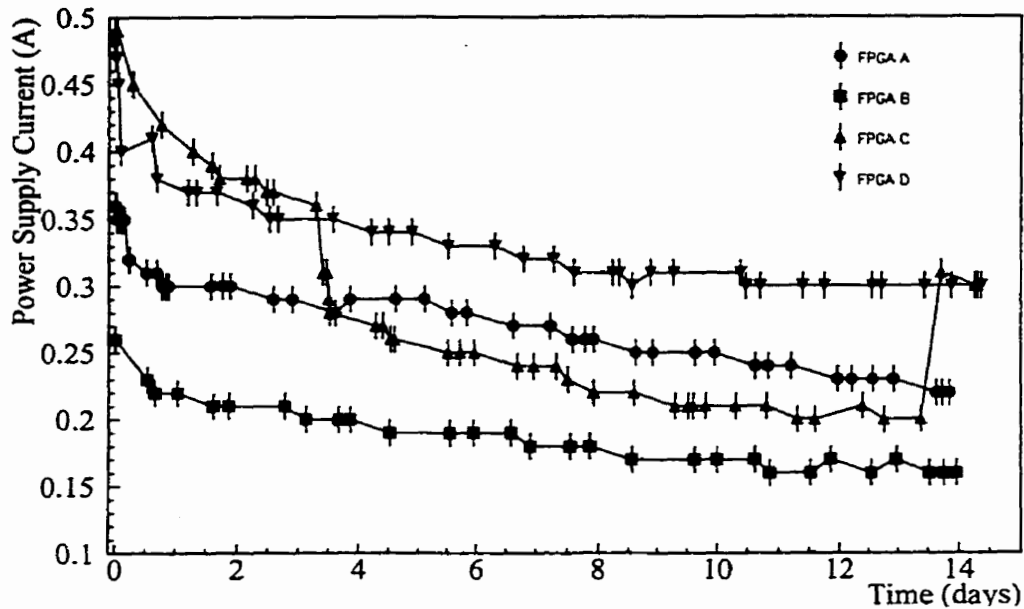


Figure 5.3: Current versus time for XL FPGAs during annealing.

5.1.3 Second Irradiation Period

Figure 5.4 shows the power supply current versus total absorbed dose for the second irradiation period. Even before irradiation began, the power supply current was higher than for a non-irradiated FPGA, showing that the damage to the device was not entirely annealed away. As well, the current began to increase almost immediately once the second period of irradiation began.

Figure 5.5 shows, for all four XL FPGAs, the total number of address sequence errors versus time after the first error recorded during the second irradiation period. The error rates for the FPGAs in the second irradiation period were very similar to those in the first irradiation period. Again, only address sequence errors were observed.

Finally, figure 5.6 shows the current versus time plot for the entire test.

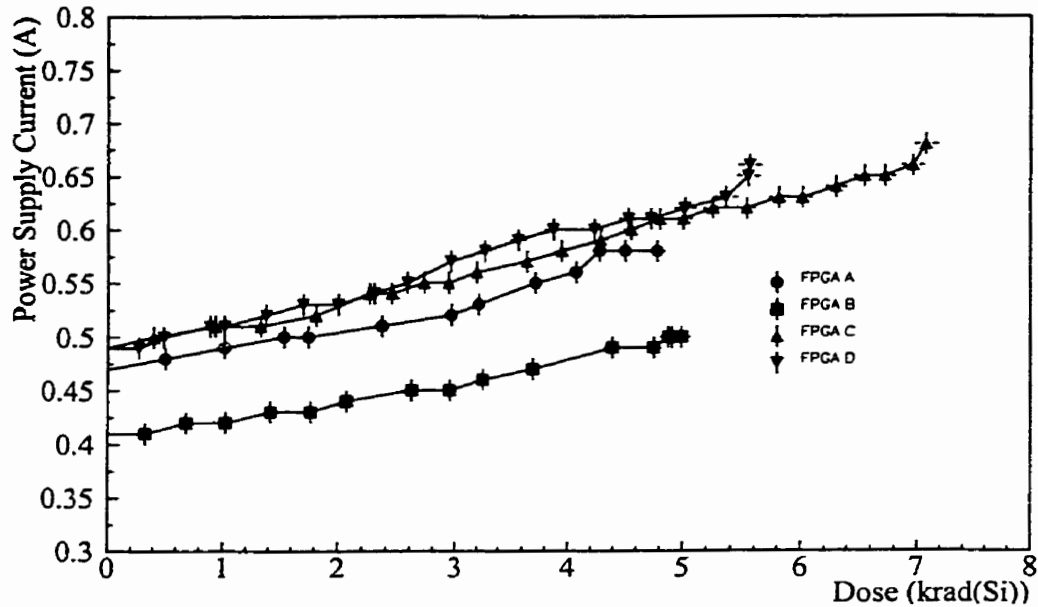


Figure 5.4: Current versus dose for XL FPGAs, second irradiation period.

The periods of increasing current are the periods of irradiation, while the period of decreasing current is the annealing period. Note that although the times in the first irradiation period where the source was removed for access to the dosimeters is eliminated from the graph, the time taken to transfer the FPGA from the cave to the oven, and the time between removing the FPGA from the oven and the beginning of the second irradiation period are not omitted.

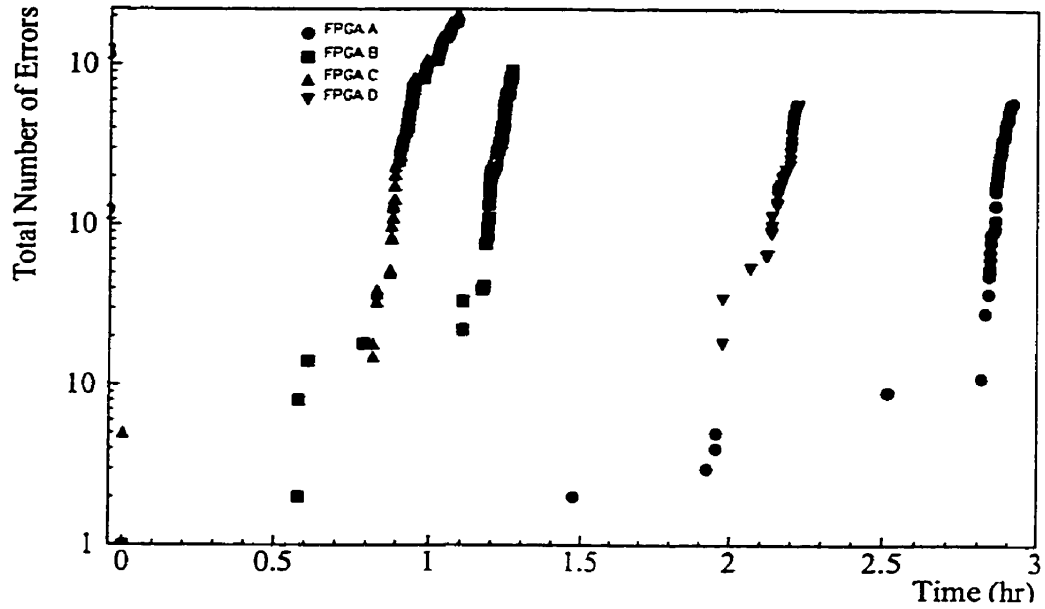


Figure 5.5: Errors versus time since first error for XL FPGAs, second irradiation period.

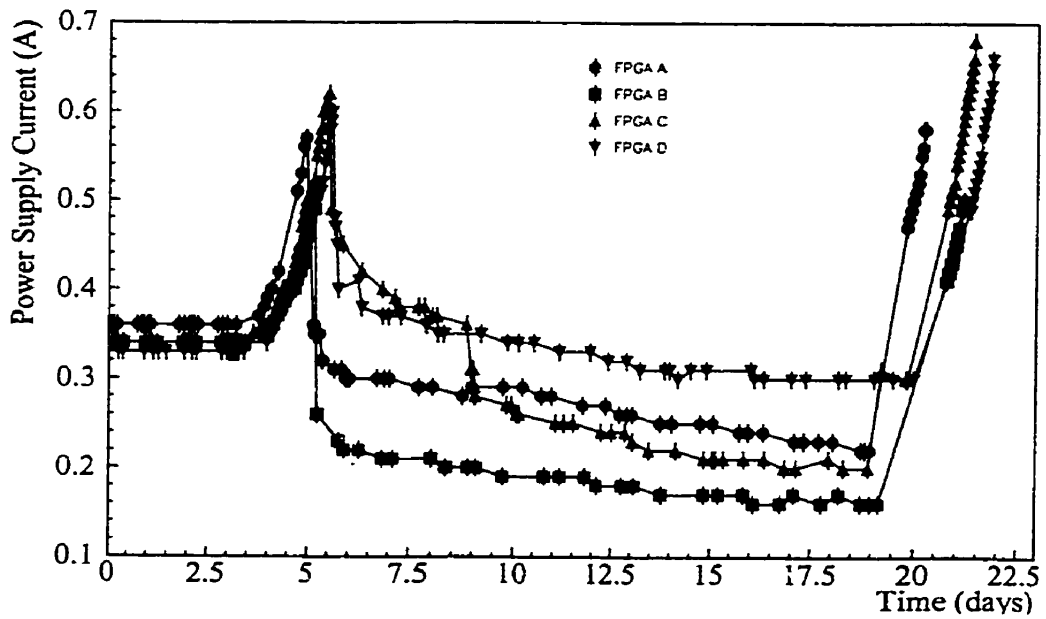


Figure 5.6: Current versus time for XL FPGAs, entire test.

5.2 Test Results for XC4036XLA Devices

Three XC4036XLA-09HQ240C FPGAs were irradiated with a cobalt-60 source, using the setup described in section 4.2 and the procedure described in section 4.5. The results of these tests have been previously presented in references [42] and [43]. In this section, the three FPGAs tested will be referred to as FPGA A, FPGA B, and FPGA C. All three XLA devices tested had a date code of 9909, and would hence be expected to behave similarly. The XLA devices were fabricated at Seiko in a $0.25\ \mu\text{m}/0.35\ \mu\text{m}$ hybrid CMOS process, where the $0.25\ \mu\text{m}$ design rules were used for the interconnects, but the transistors still had a channel length of $0.35\ \mu\text{m}$ [44].

The dose rate for each test was determined using Fricke dosimetry, just as in the XL tests. The dose rates are given in table 5.4. Again, statistical errors and systematic errors are given.

Table 5.5 shows the doses absorbed by the FPGAs before failure. As with the XL FPGAs, the increase in power supply current during the first irradiation period and the onset of logic errors during both irradiation periods are shown. Statistical and systematic errors are shown. Note that the results from FPGA C are excluded from the calculation of the average dose to first logic error during the first irradiation period, as it was substantially greater than the results from the other two devices tested.

| FPGA | Dose rate in Fricke (rad/hr) | Dose rate in Si (rad/s) |
|------|------------------------------|--------------------------------|
| A | $508 \pm 4 \pm 6$ | $0.1271 \pm 0.0011 \pm 0.0016$ |
| B | $520 \pm 3 \pm 7$ | $0.1300 \pm 0.0006 \pm 0.0016$ |
| C | $508 \pm 3 \pm 6$ | $0.1269 \pm 0.0006 \pm 0.0016$ |

Table 5.4: Dose rates measured for each XLA FPGA tested.

| FPGA | Dose absorbed (krad(Si)) | | |
|---------|---------------------------|---------------------------|---------------------------|
| | to current increase | to first error (period 1) | to first error (period 2) |
| A | $21.3 \pm 0.2 \pm 0.7$ | $38.1 \pm 0.3 \pm 0.5$ | $28.8 \pm 0.2 \pm 0.4$ |
| B | $16.48 \pm 0.08 \pm 3.34$ | $46.7 \pm 0.2 \pm 0.6$ | $51.3 \pm 0.2 \pm 0.6$ |
| C | $14.66 \pm 0.07 \pm 0.27$ | $85.2 \pm 0.4 \pm 1.1$ | $45.4 \pm 0.2 \pm 0.6$ |
| Average | 16 ± 3 | $42 \pm 4(A\&B)$ | 38 ± 10 |

Table 5.5: Results from irradiation of XLA FGAs.

5.2.1 First Irradiation Period

Figure 5.7 shows the power supply current versus total absorbed dose for the first irradiation period of the three XLA FGAs tested. The average dose absorbed by the XL chips before an increase in power supply current to 0.01 A above the value before irradiation was (16 ± 3) krad(Si). After the onset of current increase, monitoring continued until the onset of errors.

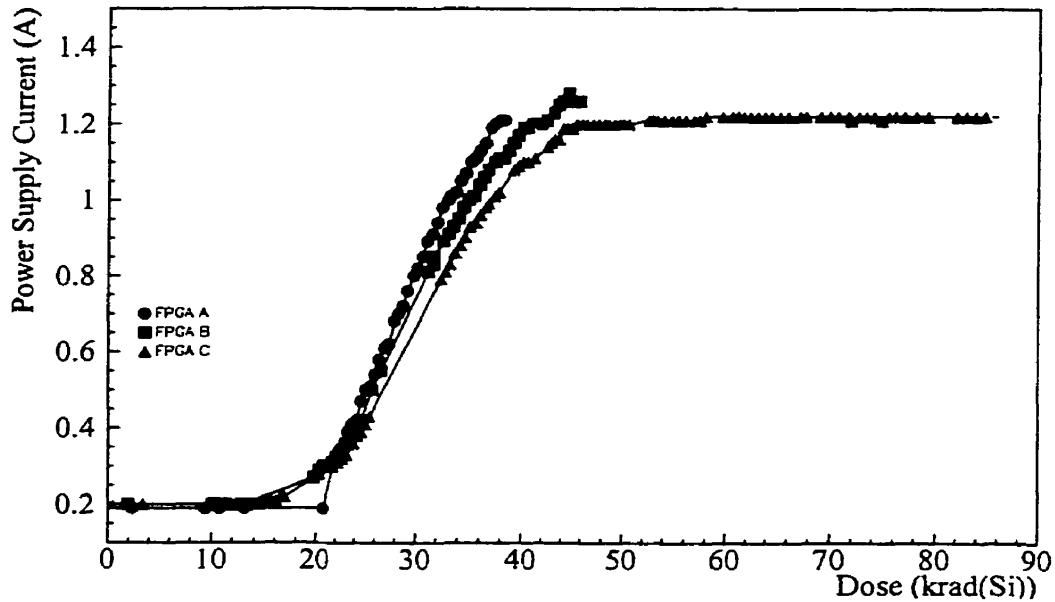


Figure 5.7: Current versus dose for XLA FGAs, first irradiation period.

One anomaly occurred during the testing of FPGA B which is not shown in figure 5.7. Sometime between 27.483 hours and 27.500 hours, the current dropped from 0.20 A to 0.11 A. Between these two current recordings, the radiation was turned off and the cave was accessed to check the Fricke dosimeter vials. It is possible that during the dosimetry check, the jostling of the wires connecting the board to the power supply caused a bad connection. At 28.067 hours, the monitoring program and the power supply were turned off. At 28.083 hours, the power supply was turned on, and the monitoring program restarted and reloaded the circuit. The current returned to 0.20 A. A similar anomaly was discovered during tests on XL FPGA C, which may also have been the result of wires being moved during a dosimetry check. However, due to the long period of time during which that FPGA may have undergone its current drop, the cause is less certain.

The average dose absorbed for the first and second XLA FPGAs until the first error was recorded was (42 ± 4) krad(Si). However, the third FPGA operated without error until $(85.2 \pm 0.4 \pm 1.1)$ krad(Si). The errors recorded for FPGA A and B during the first irradiation period were all address sequence errors, just as the case was with the XL FPGAs. However, during the first irradiation period of FPGA C, P-clock errors occurred.

As with the XL FPGAs, one hundred successive sequence or P-clock errors which are not cleared by the circuit reset resulted in an attempted reload of the circuit configuration. During the first irradiation period of FPGAs A and B, this was always successful. However, for FPGA C, after two sequence and 98 P-clock errors, 46,420 attempts to reload the configuration circuit failed. The unsuccessful downloads were flagged as InitHigh errors by the monitoring program.

Figure 5.8 shows, for all three XLA FPGAs, the total number of address

sequence errors and P-clock errors versus time after the first error recorded. Much like the XL FPGAs, FPGAs A and B show a slow error rate gradually increasing towards continuous errors, and a levelling off of the error rate after reloading of the circuit.

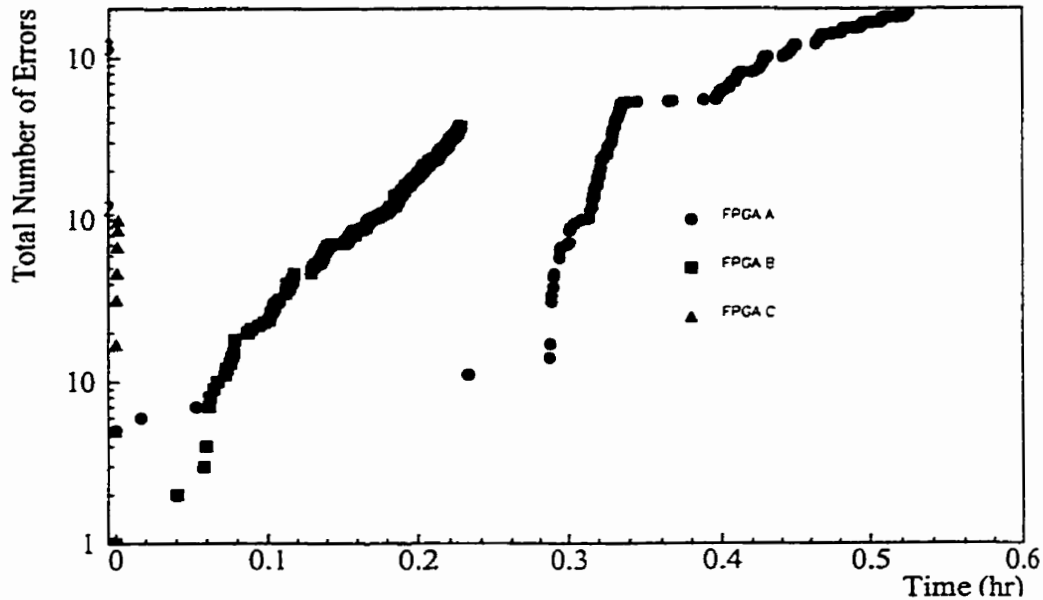


Figure 5.8: Errors versus time since first error for XLA FPGAs, first irradiation period.

5.2.2 Annealing Period

Figure 5.9 shows the current versus time for the four XL FPGAs during their annealing period. After the chip was removed from the radiation cave and transferred to the oven, the current began to rise as the oven heated up to $(50 \pm 2)^\circ\text{C}$. The first points on the graph were recorded when the FPGA's current had peaked, and the oven was finished heating up.

Although the XL chips withstood about twice the dose of the XLA chips, and

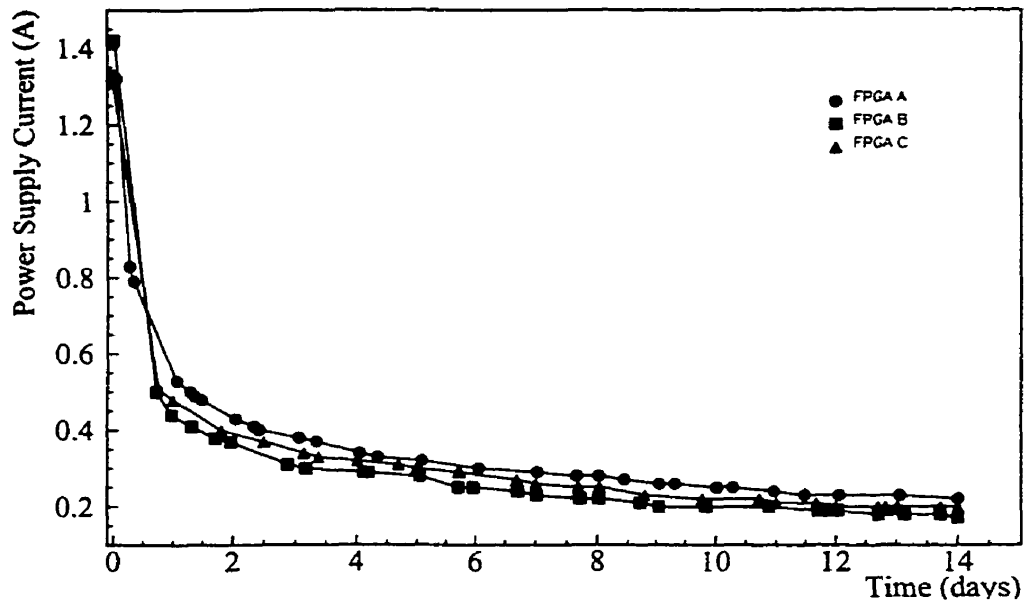


Figure 5.9: Current versus time for XLA FPGAs during annealing.

their current only increased to an average of 0.57 A under irradiation, annealing only lowered their average current from 0.40 A to 0.25 A. In the XLA FPGAs, however, average current was lowered from 1.35 A to 0.20 A over the annealing period.

5.2.3 Second Irradiation Period

Figure 5.10 shows the power supply current versus total absorbed dose for the second irradiation period. As with the XL FPGAs, the power supply current was higher than for a non-irradiated FPGA, and began to increase almost immediately once the second period of irradiation began.

Figure 5.11 shows, for the XLA FPGAs, the total number of address sequence errors and P-clock errors versus time after the first error recorded during the second irradiation period. FPGA A's errors during the second irradiation period

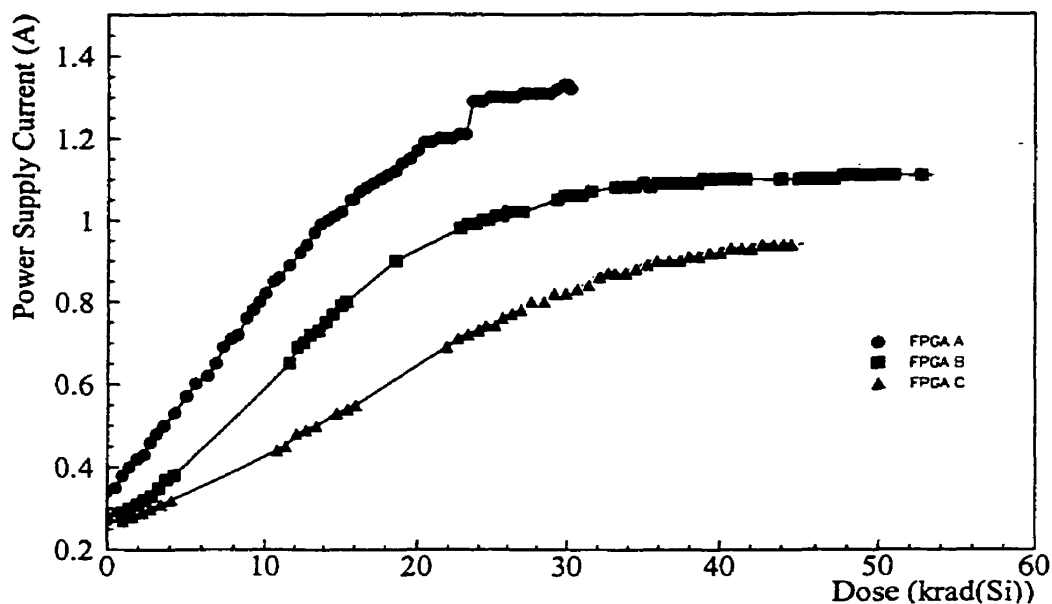


Figure 5.10: Current versus dose for XLA FPGAs, second irradiation period.

were slightly different than those recorded during the first irradiation period. After 587 sequence errors were recorded, the program attempted to download the configuration circuit again. However, even after 2924 tries, the configuration could not be downloaded. FPGA C's failure was similar to its failure during its first irradiation period, with 134 errors (which were a mixture of P-clock and sequence errors) followed by 15,568 unsuccessful attempts to download the configuration circuit (flagged by the monitoring program as InitHigh errors).

FPGA B's failure during the second irradiation period was unusual. After four P-clock errors, no further errors were recorded for more than 2.5 hours. The test was ended before the FPGA began to fail continuously.

Finally, figure 5.12 shows the current versus time plot for the entire test. As in figure 5.6, the periods of increasing current are the periods of irradiation, while the period of decreasing current is the annealing period. Note that although the

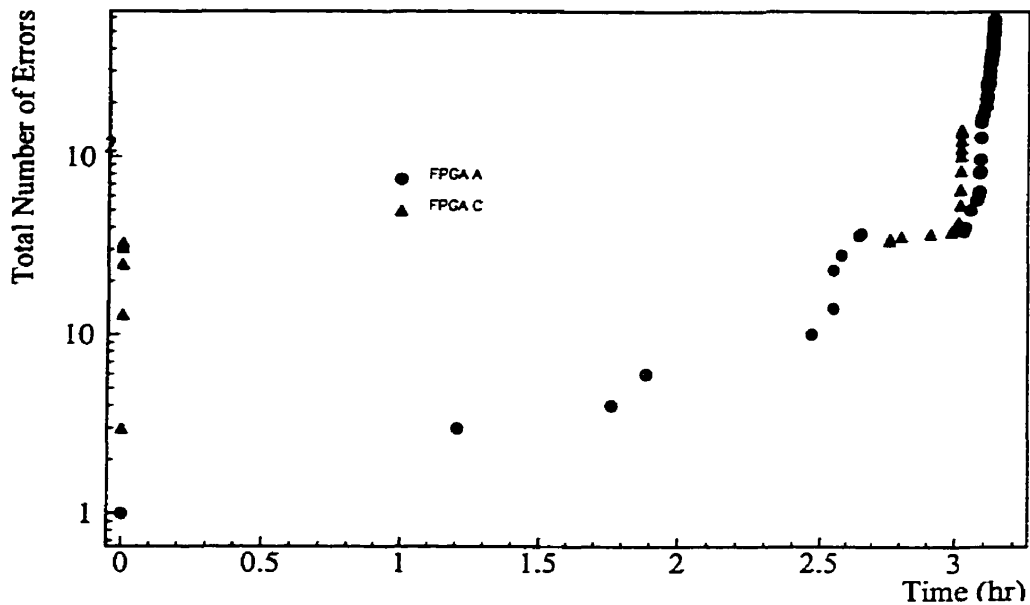


Figure 5.11: Errors versus time since first error for XLA FPGAs, second irradiation period.

times in the first irradiation period where the source was removed for access to the dosimeters is eliminated from the graph, the time taken to transfer the FPGA from the cave to the oven, and the time between removing the FPGA from the oven and the beginning of the second irradiation period are not included.

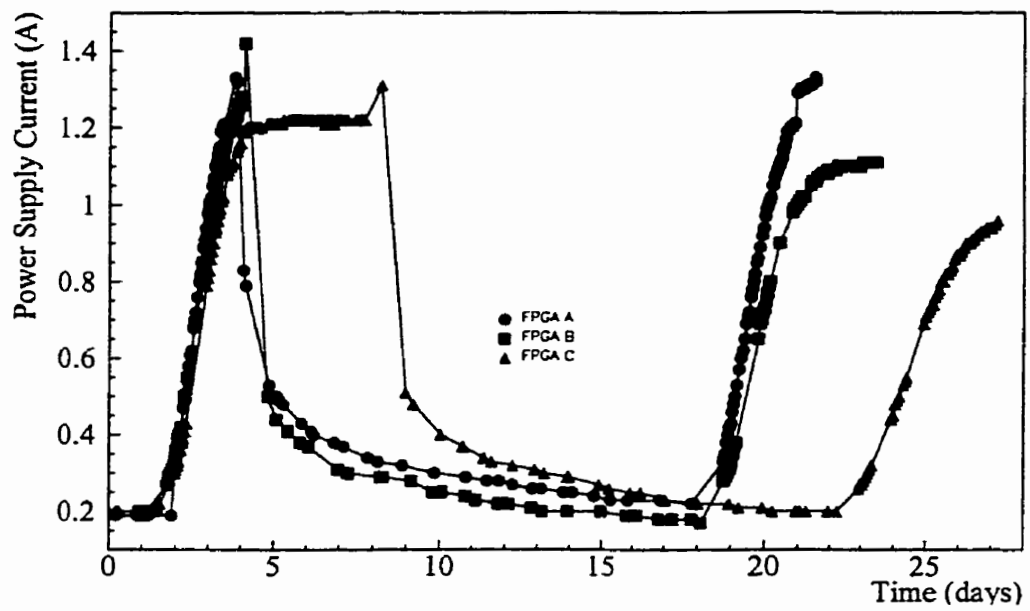


Figure 5.12: Current versus time for XLA FPGAs, entire test.

CHAPTER 6

Conclusions

Although neither the XL nor the XLA FPGAs could meet ATLAS requirements, the results of these tests can lead to interesting further study, discussed in this final chapter. General conclusions are also discussed.

6.1 Further Work

As neither the XL nor the XLA FPGAs meet ATLAS requirements, replacements must be found for use as the SCA controller chip on the front end boards. However, dose rates in some space applications are significantly lower than at ATLAS (on the order of 0.4 krad(Si)/yr [45] for low Earth orbits), which might allow the XL FPGAs, at least, to survive a space mission for several years without failure. Other applications requiring radiation resistant electronics might have less constraints on space than ATLAS, and would thus be able to better shield Xilinx FPGAs. This would increase their useful lifespan in a radiation environment.

If XC4000 series FPGAs were being considered for other applications in radiation environments, it would be instructive to test devices with different date codes (and thus from different production lots), test the FPGAs at higher and lower dose rates, and anneal at varying temperatures. This would give a more complete picture of their response to radiation.

Tests of FPGAs continue at the University of Alberta. The proton-induced SEU tests of XC4036XLA FPGAs will continue in the summer of 2000, as well as total ionizing dose tests of Altera FLEX 10K series SRAM-based FPGAs. Total ionizing dose tests might also be done on FPGAs which are specifically designed to be radiation hard. The XQR4036XL FPGAs, radiation hard devices similar to the XC4036XL FPGAs, are too slow to meet ATLAS requirements. However, it would be instructive to test Xilinx's radiation hardened FPGAs alongside XC4036XL or XC4036XLA FPGAs operating at slower speed to compare their response to radiation. The XQVR300, when it becomes available, could also be tested.

Other devices built with standard 0.35 μm or 0.35 $\mu\text{m}/0.25 \mu\text{m}$ hybrid CMOS

technologies would be expected to absorb about the same total ionizing dose as XC4036XL or XC4036XLA FPGAs before failure. Hence, other standard FPGA designs would not be suitable for use in ATLAS (though their radiation resistance may be good enough for extended use as prototype controllers at future ATLAS testbeams). Likewise, commercial processes used for ASICs would probably not produce devices which could meet ATLAS requirements for radiation tolerance, since they too are built with deep sub-micron CMOS technologies. Hence, the choices for ATLAS are radiation-hardened FPGAs or custom-designed radiation-hardened ASICs. As the radiation-hardened FPGAs available are too slow, ASICs produced in Temic Semiconductor's DMILL process [46] are the current choice for the SCA controller chips. The DMILL process is a 0.8 μm Bi-CMOS process specifically designed to resist radiation. Components built with the DMILL process can absorb ionizing doses beyond 10 Mrad [46] without failure. Prototype SCA controllers built as DMILL ASICs will also be tested by the University of Alberta.

6.2 General Conclusions

Of the two types of FPGAs irradiated with the cobalt-60 source with an average dose rate of 0.13 rad(Si)/s, the XL FPGAs were more radiation resistant, taking an average of 39 krad(Si) in the first irradiation period before increases in the power supply current were seen. The XLA FPGAs, by comparison, could only take an average dose of 16 krad(Si). These increases in power supply current were the result of the onset of leakage currents in the transistors. The XLA FPGAs also had a much larger increase in power supply current during the first irradiation period than the XL FPGAs did.

The XL FPGAs were also more resistant to logic upset than most of the XLA FPGAs. XL FPGAs could take an average of 59 krad(Si), compared to an average of 42 krad(Si) for the first two XLA FPGAs. However, a third XLA FPGA with the same date code as the others took 85 krad(Si). With the exception of XLA FPGA C's anomalous resistance to logic upset during the first irradiation period, there was not very much variation from chip to chip for either the XL or the XLA devices. However, the variation between different devices (even in FPGAs fabricated with the same date code and at the same factory, as seen with the XLA FPGAs tested) must still be considered when considering the suitability of Xilinx FPGAs for radiation applications.

Both types of FPGA responded to annealing by showing a decrease in power supply current. However, the apparent recovery was not complete, as both types of FPGA showed immediate increase in power supply current after the second irradiation period began. Although the XLA FPGAs generally showed less resistance to total dose than the XL FPGAs, they lasted longer during the second irradiation period before logic upset, taking an average of 38 krad(Si) compared to the XL

average of 4 krad(Si).

The results obtained for the dose rates received by the FPGA dies using Fricke dosimetry were quite precise, with less than 2% uncertainty. The results would show improved precision and accuracy with a better knowledge of the composition of the various plastics used in the FPGA, the socket, and the PC board. The absorbed doses taken by each FPGA until logic upset or increase in power supply current were also found precisely, with uncertainties of less than 4 krad(Si). In the case of determining the absorbed dose to increased power supply current, precision would be increased by constant automatic monitoring of the power supply current. In future radiation tests, a computer will monitor the power supply current automatically.

Since neither FPGA has been shown capable of surviving the total absorbed dose required by ATLAS, it is clear that neither the XL nor the XLA FPGAs are suited for use as the SCA controller for the front end boards.

Bibliography

- [1] ATLAS collaboration, *ATLAS Technical Proposal*, December 15, 1994.
- [2] ATLAS collaboration, *Liquid Argon Calorimeter Technical Design Report*, December 15, 1996.
- [3] J.V. Oldfield & R.C. Dorf, *Field-Programmable Gate Arrays*, John Wiley & Sons, 1995.
- [4] Xilinx Inc., *The Programmable Logic Data Book*, <http://www.xilinx.com>, 1999.
- [5] D. Mavis, B. Cox, D. Adams, & R. Greene, "A Reconfigurable, Nonvolatile, Radiation Hardened Field Programmable Gate Array (FPGA) for Space Applications", presented at the 1st annual Military and Aerospace Applications of Programmable Devices and Technologies International Conference, http://rk.gsfc.nasa.gov/richcontent/Ksymposium/Papers/B8_Mavis.pdf, 1998.
- [6] T. Speer *et al.*, "0.25 μm FLASH Memory-based FPGA for Space Applications", presented at the 2nd annual Military and Aerospace Applications of Programmable Devices and Technologies International Conference, in Proceedings CD-ROM, 1999.
- [7] W. Burris *et al.*, "The Effects of Radiation and Temperature on a Switched Capacitor Array", ATLAS Note ATL-LARG-95-016, January 23, 1995.

- [8] D.M. Gingrich, J.C. Hewlett, L. Holm, S. Mullin, B. Zhang, "SCA Controller for the Front-End Boards", version 1.2,
<ftp://jever.phys.ualberta.ca/pub/atlas/papers/UofA-ATLAS-99-1.pdf>,
August 11, 1999.
- [9] R. Bernier *et al.*, "SPAC: Serial Protocol for the ATLAS Calorimeter", ATLAS
Note ATL-LARG-98-093, March 24, 1998.
- [10] M. Shupe, "Radiation Levels in the ATLAS Detector",
<http://isnwww.in2p3.fr/atlas/andrieux/mshupe.html>, December 9, 1999.
- [11] P. Farthouat & H. Williams, "ATLAS policy on radiation hard electronics",
ATLAS Note ATL-ELEC-98-003, August 24, 1998.
- [12] W.R. Leo, *Techniques for Nuclear and Particle Physics Experiments*, Second
Revised Edition, Springer-Verlag, 1994.
- [13] R.D. Evans, *The Atomic Nucleus*, McGraw-Hill, 1955.
- [14] J.W.T. Spinks & R.J. Woods, *An Introduction to Radiation Chemistry*, John
Wiley & Sons, 1964.
- [15] S. Woolf & A.R. Frederickson, "Photon Spectra in ^{60}Co - γ Test Cells", IEEE
Transactions on Nuclear Science, Vol. NS-30, No. 6, pp. 4371-4376, December
1983.
- [16] J.H. Hubbell & S.M. Seltzer, "Tables of X-Ray Mass Attenuation Coefficients
and Mass Energy-Absorption Coefficients", NISTIR 5632, Web Version 1.02,
<http://physics.nist.gov/PhysRefData/XrayMassCoef/cover.html>, 1996.
- [17] F.S. Dainton, "Chemical Dosimetry", in *Proceedings of the International School
of Physics, "Enrico Fermi", Course XXX, Radiation Dosimetry*, pp. 167-179,

- G.W. Reed ed., Academic Press, 1964.
- [18] G.F. Knoll, *Radiation Detection and Measurement*, John Wiley & Sons, 1979.
- [19] G.C. Messenger & M.S. Ash, *The Effects of Radiation on Electronic Systems*, Van Nostrand Reinhold, 1986.
- [20] T.D. Ma & P.V. Dressendorfer, editors, *Ionizing Radiation Effects in MOS Devices and Circuits*, John Wiley & Sons, 1989.
- [21] "Total Dose Steady-State Irradiation Test Method", ESA/SCC Basic Specification No.22900, European Space Agency, April 1995.
- [22] "Ionizing Radiation (Total Dose) Test Procedure", MIL-STD-883, Method 1019.5, US Department of Defense, December 1 1997.
- [23] R. Katz *et. al.*, "Radiation Effects on Current Field Programmable Technologies", IEEE Transactions on Nuclear Science, Vol. 44, No. 6, pp. 1945-1756, December 1997.
- [24] J.J. Wang *et. al.*, "Development of Total Dose Hardened Antifuse FPGA", presented at the 1st annual Military and Aerospace Applications of Programmable Devices and Technologies International Conference, http://rk.gsfc.nasa.gov/richcontent/Ksymposium/Papers/C1_Wang.pdf, 1998.
- [25] J.J. Wang, "Radiation Performance of Actel Products", Rev6. <http://www.actel.com/products/devices/radhard/radperf.pdf>, June 6, 1999.
- [26] R. Katz, "FPGA and ASIC Main Page" <http://rk.gsfc.nasa.gov:/fpgas.htm>, 1999.

- [27] J.J. Wang *et. al.*, "SRAM-based Re-Programmable FPGA for Space Applications", IEEE Transactions on Nuclear Science, Vol. 46, No. 6, pp. 1728-1735, December 1999.
- [28] P. Alfke & R. Padovani, "Radiation Tolerance of High-Density FPGAs", presented at the 1st annual Military and Aerospace Applications of Programmable Devices and Technologies International Conference, http://rk.gsfc.nasa.gov/richcontent/Ksymposium/Papers/B6_Alfke.pdf, 1998.
- [29] E. Fuller, P. Blain, *et. al.*, "Radiation Test Results of the *Vertex* FPGA and ZBT SRAM for Space Based Reconfigurable Computing", presented at the 2nd annual Military and Aerospace Applications of Programmable Logic Devices and Technologies International Conference, <http://www.xilinx.com/appnotes/VtxTest.pdf>, 1999.
- [30] K. LaBel, A.K Moran, *et. al.*, "Single Event Effect Proton and Heavy Ion Test Results for Candidate Spacecraft Electronics", IEEE Radiation Effects Data Workshop Record, pp. 64-71, 1994.
- [31] K. LaBel, A.K Moran, *et. al.*, "Current Single Event Effect Test Results for Candidate Spacecraft Electronics", IEEE Radiation Effects Data Workshop Record, pp. 19-27, 1996.
- [32] M. Ohlsson & P. Alfke, "Neutron Single Event Upsets in SRAM-based FPGAs", IEEE Radiation Effects Data Workshop Record, pp. 177-180, 1998.
- [33] N.J. Buchanan & D.M. Gingrich, "Estimation of the Single Event Upset Cross-section for an SRAM Based FPGA", UofA-ATLAS-99-02, February 24, 2000.

- [34] G. Lum & G. Vandenboom, "Single Events Testing of Xilinx FPGAs",
http://www.xilinx.com/appnotes/Single_event/FPGAs.pdf,
- [35] D.M. Gingrich, "Measurement of the Dose Rate from the Cobalt-60 Source",
<http://www.phys.ualberta.ca/~gingrich/atlas/radiation/r2.pdf>, June
24, 1998.
- [36] D.M. MacQueen & D.M. Gingrich, "Collimation and Background Measure-
ments from the Cobalt-60 source",
<http://www.phys.ualberta.ca/~gingrich/atlas/radiation/onewall.pdf>,
August 6, 1998.
- [37] D.M. MacQueen & D.M. Gingrich, "Dose Rate Measurements in an Aluminum
Box from the Cobalt-60 source",
<http://www.phys.ualberta.ca/~gingrich/atlas/radiation/enclosed.pdf>,
July 30, 1998.
- [38] V. Bala, Saskatchewan Labour, private communication.
- [39] J.R. Taylor, *An Introduction to Error Analysis*, University Science Books, 1982.
- [40] P.W. Green, "Radiation Lab Monitoring Program",
<http://www.phys.ualberta.ca/~gingrich/atlas/radiation/monitor.html>,
October 11, 1998.
- [41] N.J. Buchanan, D.M. Gingrich, P.W. Green, & D.M. MacQueen, "Total Ioniz-
ing Dose Effects in a Xilinx FPGA", ATLAS Note ATL-LARG-99-003, 1999.
- [42] D.M. MacQueen, D.M. Gingrich, N.J. Buchanan, & P.W. Green, "Total Ioniz-
ing Dose Effects in a SRAM-based FPGA", IEEE Radiation Effects Data Work-
shop Record, pp. 24-29, 1999.

- [43] D.M. Gingrich, D.M. MacQueen, & N.J. Buchanan, "Total Ionizing Dose Effects in a SRAM-based FPGA", presented at the 2nd annual Military and Aerospace Applications of Programmable Devices and Technologies International Conference, in Proceedings CD-ROM, 1999.
- [44] J. Fabula, Xilinx Inc., private communication.
- [45] R.L. Pease, A. H. Johnston, & J.L. Azarewicz, "Radiation Testing of Semiconductor Devices for Space Electronics", Proceedings of the IEEE, Vol. 76, No. 11, pp. 1510-1526, November 1988.
- [46] Temic Semiconductors, "DMILL Technology"
<http://www.temic-semi.de:80/pdf/dmill.pdf>, June 1999.